Universitá degli Studi di Pavia

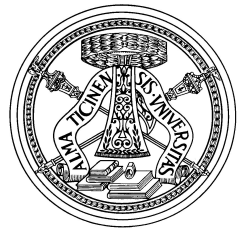

Form and structural optimization: from beam modeling to 3D printing of reinforced concrete members

by

Valentina Mercuri

A Thesis submitted in Fulfilment of the Requirements
for the Degree of Doctor in Philosophy in

Civil Engineering and Architecture
at Universitá degli Studi di Pavia

Ph.D. Program Coordinator: Prof. Ferdinando Auricchio

Supervisor:
Prof. Ferdinando Auricchio - Universitá degli Studi di Pavia

Co-supervisor:
Dr. Domenico Asprone - Universitá "Federico II" di Napoli

XXX Cycle (years 2014-2017)

To genuine people

Acknowledgments

First of all, I want to thank Prof. Ferdinando Auricchio for giving me the opportunity to start this adventurous journey. The PhD path is one of the most complex and beautiful experience you can do in your life. If I had to summarize it through keywords (like in a scientific paper, of course) I would choose: extraordinary people, knowledge, patience, life-long learning, ambition.
It is a duty for me to thank Giuseppe Balduzzi for his invaluable patience and constant encouragement in the hardest moments.
I would like to acknowledge Domenico Asprone and Costantino Menna from University "Federico II" of Naples for their constant help and availability. The same acknowledgment goes to Paola Festa and a special one to Tommaso Pastore, a great colleague and, foremost, a good friend.

One of the best part of this three-years journey was the period I spent at the Statik Chair with Prof. Bletzinger and his group. I want to thank all of them for the collaboration and the interest they have always shown towards my project. Another mandatory thank is for all the guys met at the Oskar Von Miller Forum, really brilliant minds!

Thanks to all the people of the Compmech group, from veterans to novices. All of you have been more than essential during these fantastic years. Just to mention some motivations, I could not survive without vegetables from Albe's field, laughs of Marghe, Xi's suggestions and rides in the Massimo's car.

My greatest thanks go to the TTF group: Marco, Isa, Rod, Ele, Montix and the little Diego. I will miss you as well as I will miss our incredible dinners.

I big hug goes to my sweet Melisú, my friend Borgo from Camburá and my super cool friend Ale. Near or far you have always been able to give me the help and friendship I needed.

Last but not least, the final thanks go to my genuine people. The dedication in the first page is made on purpose because this category well represent the most important people of my life: my family. You will be always my first example, the starting point and the horizon in front of me.

Thanks to my beloved Matteo, you are the best miller and the best man in the world. Thanks to you I realized who I am and what I want to be. I love you.

Abstract

Nowadays, in the fields of civil engineering and architecture there is a growing demand for designing and building complex shapes using innovative materials and technologies. To meet this demand, engineers and architects work in parallel to find the best solutions in terms of feasibility, optimization, speed of construction and costs. Regarding this point, the development of increasingly sophisticated numerical tools together with the available computational power, makes easier to study non-conventional and complex design problems. Among these, non-prismatic and curved elements should be mentioned since characterized by a non-trivial behavior, usually leading to modeling issues. Furthermore, recent technological advances, especially in Additive Manufacturing (AM), enable the realization of challenging solutions and the use of optimization methods to design components with better performances. In particular, topology optimization methods have been identified as a key technique to fully exploit the capabilities of AM.

Starting from this background, the objective of the work is to investigate both the performance of new numerical tool when used for complex design problems and a novel approach for the 3D printing of optimized structural elements. Firstly, the study of an accurate non-prismatic beam model and its comparison with building software in real cases is reported. Results comparison emphasizes the importance of using accurate modeling strategies when non-conventional elements have to be modeled. Secondly, an innovative 3D printing method to manufacture Reinforced Concrete (RC) elements is proposed together with some preliminary studies on possible compatible topology optimization methods. Conclusion and future developments on the proposed manufacturing approach are reported; current difficulties in the implementation of topology optimization tools for the 3D printing application are also discussed.

Contents

List of Tables

List of Figures

1 Introduction

Form and structure in engineering and architecture are the first important issues in the establishment of the space, in the design and construction process of a building. The strong relationship between form and structure can be understand simply recalling the base meaning of these two words. Any material form (i.e., the object represented by that form) is exposed to gravitational and other accidental actions that can load it during its life. To withstand these loads, thus to preserve shape and function in time, a structure is needed. Therefore, it is implicit that any structure must allow the internal flow of forces, and design optimal structure can not ignore the study of the force transfer in dependence of the shape. Although this intrinsic relation, often form and structure are still conceived in a separate manner: the form is designed in relation to functional and aesthetic motivations, to the need of replicate a particular element, while the structure is limited to be the organism capable of absorbing forces, with a form already outlined but without bothering or occupy too much space. This concept is well exemplified by the Eduardo Torroja quote: "the designer, in love with a solution (...), goes to the structural engineer to insert it into a structure" [Torroja and Miret, 1958]. The same thought is reflected on the historical idea for which architects and engineers are independent, which mainly underlines differences rather than advantages coming from an harmonious cooperation. Indeed, the synergy between skilled engineers and designers is necessary to shape ambitious building and to reach optimal designs. Concerning the structural optimization, it can be expressed at a global level (i.e., the performance of a building under seismic loads) or at the single structural element level (i.e., the topology optimization of a component, the ultimate strength of a pillar). Furthermore, an optimal design means also: good balance between efficiency of the structure and aesthetic benefits, cost and material savings, simplification of the construction technique.

Despite this persistent gap between these two domains, there are eminent examples from the past and not only, showing that form and structure, aesthetics and technique can work perfectly together. Among them, we can recall Eduardo Torroja, Spanish engineer notable as a pioneer in the design of concrete-shell structures. He believes there are three basic elements to keep in mind for the definition of a structural system: balance, strength and stability. He uses, in fact, the knowing of isostatic lines to ensure the correspondence of the structure to the developed stresses, without renouncing to complex aesthetic shapes.

Another significant example is given by Robert Maillart who revolutionizes the

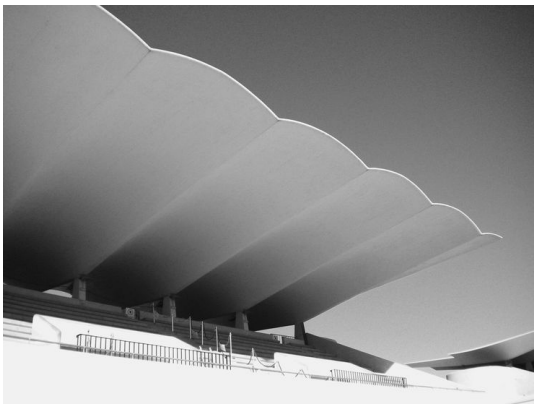

(a)

(b)

Figure 1.1. Eduardo Torroja *Roof of La Zarzuela Racetrack*, Madrid, Spain (a)-reproduced from Montalar [2012]; Robert Maillart *Salginatobel Bridge*, Schiers, Switzerland (b)-reproduced from Schoenholz [2006].

use of reinforced concrete, trying to overcome the constraints linked to the production methods. He eliminates from his structures all that is not functional, as for the deck-stiffened arch for bridges which turns into a new structural element [Giedion, 1967]. The advent of concrete and new pre-compression techniques have greatly influenced the designers during the fifties and sixties, leading to non-conventional results in terms of shapes and efficient structures. Nowadays, the technical intuition runs in parallel with a dramatic technological development. In fact, the scientific progress and the multidisciplinary research make possible the optimization of several stages within the design process and new breath for the creativity.

In particular, a great impact in the integrated development of civil engineering and architecture is given by:

- Increasing cooperation between the domains of civil engineering and architecture due to complex infrastructure and integrated projects;
- Continuous research on common building materials and increasing study of innovative and sustainable materials;
- Development of computer science and increase of the computational power;
- Development of software and numerical tools increasingly wider and more sophisticated;
- Implementation of new technologies and growth of computer-controlled processes.

All these aspects are needed for the purpose of achieving optimal solutions for buildings and infrastructures. Focusing on the evaluation of the structural response, the availability of advanced software and numerical tools is essential, especially when non-trivial problems are tackled. As example, the simple design of non-prismatic and curved elements requires the use of accurate modeling strategies or refined numerical analysis, since the simple models are not effective in predicting their real behavior [Hodges et al., 2010]. Another key point is the actual potential in producing optimized shapes given by the contemporary technology improvements. Indeed, innovative technologies such as Additive Manufacturing (AM) and 3D printing open the possibility to overcome limits currently imposed by conventional manufacturing techniques and can represent the link step between classical optimization methods and application [Zegard and Paulino, 2016].

There are several contemporary designers and studios which have already actualized scientific and technological improvements in real projects. One recent example is provided by a research team lead by Arup which has applied the 3D printing technique for the production of steel joints. The team's idea was to give a solution for the joints of lightweight tensile structure characterized by a complex shape and very customized design. The process developed is based on additive laser sintering principle and employs steel derivatives as printing materials. Figure 1.2 shows the evolution of a steel node from the initial design to the final one. The three structural elements (nodes) are all designed to carry the same structural loads and forces. The third item is designed adopting the latest optimization methods. As commented by Salom Galjaard, the team leader, "By using additive manufacturing we can create lots of complex individually designed pieces far more efficiently. This has tremendous implications for reducing costs and cutting waste. But most importantly, this approach potentially enables a very sophisticated design, without the need to simplify it in a later stage to lower costs."

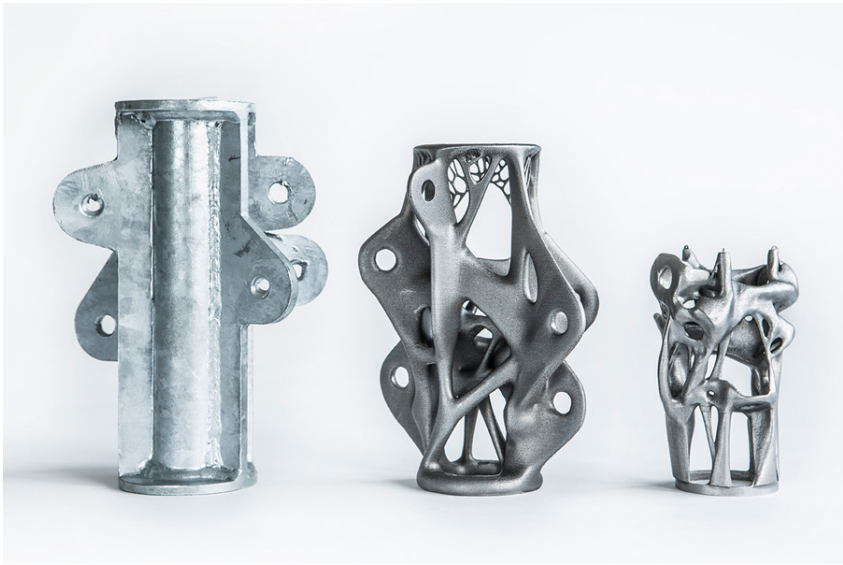

Figure 1.2. 3D Printing steel joints designed by the Arup's team: the three structural elements (nodes) are all designed to carry the same structural loads and forces (reproduced from ARUP [2014]).

It is from this background that arise the leading themes of this thesis. We want to investigate both the performance of structural software for complex design problem and a novel 3D printing approach for the construction of optimized concrete structural elements. In particular, the present work focuses on:

- The study of an accurate non-prismatic beam model and its comparison with the building software SAP2000 in real modeling problems;
- An innovative 3D printing method for the production of Reinforced Concrete (RC) elements and possible compatible topology optimization tools.

In the following Chapters all of these arguments are developed, as detailed in Section 1.1 which describes the organization of the work.

1.1 Outline of the work

After the introductory Chapter 1, the present dissertation is subdivided in six main Chapters.

- Chapter 2 opens with a literature review on analytic and numerical modeling approaches for the modeling of non-prismatic members. Then, a summary of the assumptions considered for the studied beam model are illustrated together with some preliminaries numerical results.

- Chapter 3 deals with practical applications of the presented non-prismatic beam model. Such model is compared with the structural software SAP2000 both in simple and complex problems.

- Chapter 4 gives an overview on the "state of art" of the AM impact in the construction field, with a particular focus on applications with concrete material. Then, a detailed description of the proposed 3D printing approach for the production of RC members and the 3D printed tests is reported.

- Chapter 5 delineates the starting optimization problem derived from the proposed 3D printing approach. A description of the developed Matlab optimization algorithm is provided together with some preliminary tests and results from a real case study of a concrete beam. Then, the software Kratos and its topology optimization application is evaluated in the analysis of 3D-printed objects. Finally, advantages and disadvantages of the analyzed optimization tools are discussed.

- Chapter 6 concludes the work by studying the mechanical behavior of the two full-scale beams manufactured with the proposed 3D printing strategy. Numerical and experimental results coming from the tests are commented. Finally, main issues and opportunities of this innovative production method are highlighted.

- Chapter 7 reports conclusions and future developments about the treated arguments.

2 Non-prismatic beam model

In many engineering fields non-prismatic structural elements are widely used since they allow to: satisfy special architectural and functional requirements, optimize the structural behavior, and reduce both manufacturing and operation costs. As an example, a non-prismatic beam allows to obtain the maximum strength with the minimum amount of material [Timoshenko, 1955]. Focusing the attention to civil engineering, non-prismatic beams result particularly advantageous in large span structures like bridges, industry roofing, sport arenas, as well as in multi-stories buildings.

However, the design of members with variable cross-section is not a trivial task due to the fact that the behavior of such elements is intrinsically different from prismatic ones leading to a greater complexity of the equations. Furthermore, recent contributions highlight that the main peculiarities of non-prismatic beams are a non-trivial stress distribution and a more complicated constitutive relation deeply influencing the whole beam behavior [Bennati et al., 2016, Balduzzi et al., 2016a, Zhou et al., 2016]. For this reason classical beam theories are not adequate for the description of non-prismatic beams and an accurate modeling becomes a crucial step for an effective design. In fact, if the model provides a coarse estimation of quantities of interest for practitioners like displacements or stress, the resulting design will be non-optimal and, in extreme situations, even critical [Paglietti and Carta, 2007, Beltempo et al., 2015a].

In this framework, the purpose of this Chapter is studying an accurate model (identified in the following with the name NP-Model) for the analysis of 2D linear elastic non-prismatic beams. Starting from the literature background, the concept of the evaluation of the stiffness matrix for non-prismatic beams is reviewed since it represents a fundamental step for any structural analysis and computations nowadays required in the engineering practice. Then, related applications will be presented in Chapter 3 through numerical examples. The NP-model comes from the generalization of a procedure illustrated in Auricchio et al. [2010], following developed by Balduzzi [2013] and Beltempo et al. [2015b]. The approach adopted for the beam model derivation is the so-called dimensional reduction method, starting from the stationarity of the Hellinger-Reissner (HR) functional.

To properly contextualize the proposed work, Section 2.1 opens with a literature review on analytic and numerical modeling approaches for non-prismatic beams with a particular focus on the evaluation of the stiffness matrix. Then, a summary of the assumptions considered for the NP-Model are illustrated in Section 2.2.

Here, the NP-model is tested and results from different hypotheses on the stress and displacement fields are compared and discussed.

2.1 Literature review

The analysis of non-prismatic members has been the subject of research effort starting from the seventies. In general, the governing differential equations of beams with variable depth (see the rigorous formulation given by Timoshenko and Goodier [1970]) are characterized by variable coefficients and this fact increases the difficulty of the solution. Due to the complexity inherent in the exact integration of equations, alternative strategies have been pursued adopting both analytic and numerical approaches.

2.1.1 Modeling approaches for non-prismatic beams

The classical modeling approach for non-prismatic beams consists in modifying the coefficients of prismatic beam Ordinary Differential Equations (ODEs) [Timoshenko and Young, 1965] to account for cross-section area and inertia variations [Portland and Cement Associations, 1958]. Consequently, the resulting ODEs are characterized by variable coefficients which lead to a non-polynomial, complex and difficult to evaluate solution [Timoshenko and Goodier, 1970, Romano and Zingone, 1992, Romano, 1996]. In the past, when computers were not easily available, the solution complexity leaded either to use simplified alternative approaches, e.g., the carry-over factors provided in Portland and Cement Associations [1958] (PCA) or to employ non-trivial approximated formulas [Medwadowski, 1984, Schneider and Albert, 2014]. Despite the strong impact on design practice for many years, several investigations show that such simplified strategies, as PCA tables, could lead to significant errors [El-Mezaini et al., 1991, Balkaya et al., 1996, Al-Ghatani and Khan, 1998]; similarly, Balduzzi et al. [2016b] demonstrates that formulas provided by Schneider and Albert [2014] could also significantly underestimate beam deflection, leading to non-negligible errors in the serviceability analysis of structures.

Generally, the weakness of the above mentioned approaches and also of the majority of similar contributions reported in literature is that they are based on formulas derived from prismatic beam theories. Unfortunately, such an approach is inadequate since non-prismatic beams behavior is significantly different from the prismatic ones for the following three main reasons:

- The smooth variation of cross section size along the beam axis produces non-trivial shear stress distributions, as highlighted in Timoshenko and Goodier [1970] and Bruhns [2003];
- The boundary equilibrium on lateral surface leads the shear stress distribution to depend not only on the vertical internal force (as usual for prismatic

beams), but also on the bending moment and on the horizontal internal force [Blodgett, 1966, Vu-Quoc and Léger, 1992]. According to this statement, several researchers notice that the violation of boundary equilibrium on the beam's lateral surface is an important source of error, especially when the slope of lateral surfaces is not negligible [Boley, 1963, Hodges et al., 2008, 2010];

- Finally, if the shear stress depends on all internal forces, also the shear deformation will do the same leading to more complicated constitutive relations. This peculiarity of non-prismatic beams was initially noticed by Vu-Quoc and Léger [1992] and then approached by Rubin [1999].

Looking at the large dedicated literature, the contributions that effectively tackle the three problems so far introduced are few. An initial attempt in this direction was proposed by Auricchio et al. [2015] that use a dimensional reduction method applied to the Hellinger-Reissner functional together with high order kinematics and highly refined assumptions on stress distribution. The model presented in Auricchio et al. [2015] is extremely accurate, nevertheless its complexity leads to ODEs which require numerical tools in order to be solved, even in the simplest cases. According to these encouraging results, Beltempo et al. [2015b] followed the same derivation procedure, adopting a simpler set of hypothesis on kinematics and stress distributions, which significantly reduces the model complexity without a significant loss in the accuracy. Finally, Balduzzi et al. [2016a] derives a non-prismatic beam model based on the Timoshenko kinematics; for such model, even if the resulting ODEs allows the analytical calculation of both homogeneous and particular solution, its complexity leads to restrict the practical usefulness of such analytical approach.

2.1.2 Numerical evaluation of non-prismatic beams stiffness matrix

As technology and computer science were developing, numerical analysis has become very popular in several engineering fields, resulting particularly useful in problems described by complex differential equations. For this reason, such techniques started to be frequently used for the study of beams with variable cross-section and for the derivation and implementation of the stiffness matrix. In the large body of research performed on beams with variable cross-section, alternative strategies have been pursued adopting numerical approaches.

The simplest numerical approach to solve non-prismatic beam problems is the so-called stepped beam, i.e., to approximate the non-prismatic beam as a sequence of prismatic elements [Kosko, 1982, Raymond and Wang, 1988, Patel and Acharya, 2016]. Obviously, such an approach needs a lot of elements to achieve a reasonable accuracy, turning out to be uselessly expensive if compared to the obtained solution

quality. Furthermore, according to remarks on modeling effectiveness introduced in Section 2.1.1, the stepped beam approach provides still wrong descriptions of both stress distribution and stiffness.

A slightly more refined strategy consists in solving numerically suitable weak formulations of the prismatic beam model ODEs with non-constant coefficients. Within this modeling strategy, one of the first contributions was provided by Just [1977] with a formulation based on the Euler Bernoulli (EB) theory and the virtual work principle. Here the stiffness matrix items are computed considering shape functions modified to account for variations in cross-section properties. According to this procedure, but aiming at providing a faster evaluation procedure, Browns [1984] presented a method where approximate interpolation functions were used to obtain bending stiffness matrix. Conversely, Eisenberger [1985] derived matrix components for members with variable cross-section taking into account height and width variation and starting from the flexibility method. Another approach based on flexibility method and Timoshenko formulation was presented by Tena-Colunga [1996], who including shear deformation and the variability of the cross-section in order to be effective both for 2D and 3D tapered members.

More recently, Zhi-Luo et al. [2007] exploited the transfer matrix method for continuous and discontinuous non-prismatic members, while Gimena et al. [2008a,b] studied spacial arch problems providing both analytical exact and numerical approximate procedures for curved beams with different support conditions. Following a similar procedure, Shooshtari and Khajavi [2010] investigated shape functions and stiffness matrices of non-prismatic beams. Balkaya [2001] studied the behavior of haunched beams[1] having T-section using 3D Finite Element (FE) models and proposed a two-node beam element having average inertia and area. Failla and Impollonia [2012] developed a method particularly useful in sensitivity, damage identification and optimization, based on the theory of generalized functions to solve non-uniform and discontinuous beams in static analysis. Finally, in a recent paper Trinh and Gan [2015] derived shape functions for a linearly tapered Timoshenko solid beam element starting from the Hamilton principle.

Unfortunately, all of the researches mentioned above consider only the variability of the area and inertia and neglect at least one of the three problems introduced in Section 2.1.1, undermining the effectiveness of all the proposed tools. To the authors' knowledge the only approach that overcomes this huge limitation is the 3D FE analysis proposed by El-Mezaini et al. [1991] that nevertheless turns out to be extremely expensive from the computational point of view.

Despite the research effort of the last decades, it is still noticed the need of an efficient approach in numerical methods involving non-uniform and discontinuous beam. In fact, some of the cited methods started from prismatic suitable formulations, for others it is not possible to retrieve shape functions which might be necessary for the analysis based on stiffness formulations. Furthermore, the

[1] Haunched beam: a beam whose cross section thickens toward its supports.

complexity and accuracy of the predictive model has to be balanced with analysis computational costs and time consumption.

2.2 Synopsis and evaluation of the NP-Model

In the following, the main steps at the base of the NP-Model derivation are reviewed. In particular, different adopted hypotheses on the stress and displacement fields are introduced and then compared to evaluate the model behavior. For a detailed description of the theory it is recommended to refer to Balduzzi [2013] and Beltempo et al. [2015b].

2.2.1 Geometry definition

The object of the study is a non-prismatic planar beam that behaves under the assumptions of small displacements and linear elastic isotropic constitutive law.

The beam is geometrically defined introducing a segment $[0, L]$ along the beam-axis direction x and two sufficiently smooth functions, $h_u(x)$ and $h_l(x)$ (such that $h_l(x) < h_u(x)\ \forall\ \mathrm{x} \in [0, L]$), describing the geometry of the beam upper and lower bounds (Figure 2.1). We may introduce $c(x)$ as the cross-section centroids and $t(x)$ as the cross-section depth, both of them expressed in terms of $h_u(x)$ and $h_l(x)$ as follows:

$$c(x) = \frac{h_u(x) + h_l(x)}{2} \tag{2.1a}$$

$$t(x) = h_u(x) - h_l(x) \tag{2.1b}$$

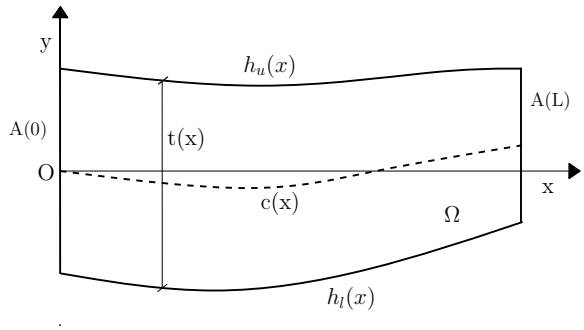

Figure 2.1. Geometric parameters of the generic non-prismatic beam.

2.2.2 NP-Model derivation

The NP-model derivation starts from a mixed Hellinger-Reissner functional whose expression is:

$$J_{HR}(\mathbf{s},\boldsymbol{\sigma}) = \int_\Omega (\boldsymbol{\sigma} : \nabla^s \mathbf{s})\, d\Omega - \frac{1}{2}\int_\Omega (\boldsymbol{\sigma} : \mathbf{D} : \boldsymbol{\sigma})\, d\Omega - \int_\Omega (\mathbf{s}\cdot\mathbf{f})\, d\Omega + \\ - \int_{\partial\Omega_s} (\boldsymbol{\sigma}\cdot\mathbf{n}\cdot\bar{\mathbf{s}})\, dS = 0 \quad (2.2)$$

where the displacement $\boldsymbol{s}$ and the stress $\boldsymbol{\sigma}$ are the two unknown bi-dimensional fields, i.e. $\boldsymbol{s} = \boldsymbol{s}(x,y)$ and $\boldsymbol{\sigma} = \boldsymbol{\sigma}(x,y)$. Then, a dimensional reduction method is exploited in order to reduce the 2D domain Hellinger-Reissner functional into a 1D domain problem associated to the beam axis. This is possible through the introduction of suitable hypotheses on displacements and stresses and the exploitation of the domain structure.

Within the derivation procedure, to enforce the boundary equilibrium the outward unit vectors on the lower and upper-limits result as follow:

$$\mathbf{n}|_{hl}\,(x) = \frac{1}{\sqrt{1+(h_l{}'(x))^2}} \begin{Bmatrix} h_l{}'(x) \\ -1 \end{Bmatrix} \quad (2.3a)$$

$$\mathbf{n}|_{hu}\,(x) = \frac{1}{\sqrt{1+(h_u{}'(x))^2}} \begin{Bmatrix} -h_u{}'(x) \\ 1 \end{Bmatrix} \quad (2.3b)$$

where $(\,\cdot\,)'$ means the derivative with respect to the independent variable x. As a consequence, the boundary equilibrium on lateral surface $\boldsymbol{\sigma}\cdot\mathbf{n}|_{h_l\cup h_u}$=0 could be expressed as follow:

$$\begin{bmatrix} \sigma_{xx}(x,y) & \sigma_{xy}(x,y) \\ \sigma_{xy}(x,y) & \sigma_{yy}(x,y) \end{bmatrix} \begin{Bmatrix} n_x \\ n_y \end{Bmatrix} \Big|_{h_u/h_l} = \begin{Bmatrix} 0 \\ 0 \end{Bmatrix}$$

$$\Longrightarrow \begin{cases} \sigma_{xy}(x,y)\,|_{h_u/h_l} = -(n_x/n_y)\sigma_{xx}(x,y)\,|_{h_u/h_l} \\ \sigma_{yy}(x,y)\,|_{h_u/h_l} = (n_x/n_y)^2\sigma_{xx}(x,y)\,|_{h_u/h_l} \end{cases} \quad (2.4)$$

It is worth to notice that equation (2.4) explicits one of the differences between prismatic and non-prismatic beam discussed in Section 2.2.1. In particular, the variable profile of the beam and consequently the particular expressions of the outward unit vectors lead to the dependence of the σ_{xy} and σ_{yy} components with the σ_{xx} one.

After the selection of the variational principle, the second step in the dimensional reduction procedure consists in the selection of cross shape functions to approxi-

mate each involved fields, and can be expressed as follows:

$$\gamma(x, \mathbf{y}) \approx \mathbf{r}_\gamma{}^T(\mathbf{y})(x, \mathbf{y})\hat{\gamma} \tag{2.5}$$

where γ is the generic field, $\mathbf{r}_\gamma$ is the storing vector of the cross-section shape functions. The cross-shape functions $\mathbf{r}_\gamma$ are a set of pre-assigned, linearly-independent functions. As a consequence, the field γ is uniquely determined by the axial coefficient functions $\hat{\boldsymbol{\gamma}}$ that are indeed the unknowns of the beam model.

Considering equation (2.5) and introducing the boundary equilibrium, we can rewrite the expression of $\mathbf{s}$ and $\boldsymbol{\sigma}$ fields in an engineering notation:

$$\mathbf{s} = \begin{Bmatrix} s_u(x,y) \\ s_v(x,y) \end{Bmatrix} \approx \begin{bmatrix} \boldsymbol{r}_u^T & \mathbf{0} \\ \mathbf{0} & \boldsymbol{r}_v^T \end{bmatrix} \begin{Bmatrix} \hat{\boldsymbol{u}} \\ \hat{\boldsymbol{v}} \end{Bmatrix} \tag{2.6}$$

$$\boldsymbol{\sigma} = \begin{Bmatrix} \sigma_{xx}(x,y) \\ \sigma_{yy}(x,y) \\ \sigma_{xy}(x,y) \end{Bmatrix} \approx \begin{bmatrix} \boldsymbol{r}_{\sigma x}^T & \mathbf{0} & \mathbf{0} \\ \boldsymbol{r}_{\sigma x}^T \boldsymbol{T}^{\mathbf{2}} & \boldsymbol{r}_{\sigma x}^T & \mathbf{0} \\ \boldsymbol{r}_{\sigma x}^T \boldsymbol{T} & \boldsymbol{r}_{\sigma x}^T & \mathbf{0} \end{bmatrix} \begin{Bmatrix} \hat{\boldsymbol{\sigma_x}} \\ \hat{\boldsymbol{\sigma_y}} \\ \hat{\boldsymbol{\tau}} \end{Bmatrix} \tag{2.7}$$

where $\boldsymbol{T}$ is a diagonal matrix defined as follows:

$$T_{ii} := \begin{cases} 0 & if \quad p_{\sigma_x i}\,|_{h_l} = p_{\sigma_x i}\,|_{h_u} = 0 \\ {h_l}' & if \quad p_{\sigma_x i}\,|_{h_l} \neq 0 \\ {h_u}' & if \quad p_{\sigma_x i}\,|_{h_u} \neq 0 \end{cases} \tag{2.8}$$

To apply the dimensional reduction procedure and the boundary equilibrium relations, we need to introduce suitable hypotheses on the unknown fields $\mathbf{s}$ and $\boldsymbol{\sigma}$ thus to define the $\mathbf{r}_\gamma$ coefficients. In particular, to test the NP-model behavior three different set of hypotheses have been selected, with a progressive increase in the polynomial degree for the shape functions. Table 2.1 summarizes the assumptions made in choosing the degree of the shape functions; we assume that the $deg(r_\gamma)$ denotes the highest polynomials degree of the generic cross-section shape function with respect to y.

The explicit expressions of the three considered set of hypotheses are reported in the following.

Hypotheses		r_u	r_v	$r_{\sigma x}$	$r_{\sigma y}$	r_τ
Hp1	$deg(r_\gamma)$	1	0	1	0	2
Hp2	$deg(r_\gamma)$	1	0	1	-	2
Hp3	$deg(r_\gamma)$	1	2	1	3	2

Table 2.1. Highest polynomials degree with respect to y of generic cross-section shape function.

- **Hp1**

$$s_u(x,y) = u0(x) + \tilde{y}\frac{t(x)}{2}\theta(x) \tag{2.9a}$$
$$s_u(x,y) = v0(x) \tag{2.9b}$$

$$\sigma_{xx}(x,y) = \sigma_{x0}(x) + \tilde{y}\sigma_{x1}(x) \tag{2.10a}$$
$$\sigma_{yy} = 0 \tag{2.10b}$$
$$\sigma_{xy} = h_l{}'(x)(\sigma_{x0}(x) + \sigma_{x1}(x))\frac{h_u(x) - y}{h_u(x) - h_l(x)} + h_u{}'(x)(\sigma_{x0}(x)+$$
$$-\sigma_{x1}(x))\frac{y - h_l(x)}{h_u(x) - h_l(x)} + \tilde{b}\tau(x) \tag{2.10c}$$

- **Hp2**

$$s_u(x,y) = u0(x) + \tilde{y}\frac{t(x)}{2}\theta(x) \tag{2.11a}$$
$$s_u(x,y) = v0(x) \tag{2.11b}$$

$$\sigma_{xx}(x,y) = \sigma_{x0}(x) + \tilde{y}\sigma_{x1}(x) \tag{2.12a}$$
$$\sigma_{yy} = h_l{}'(x)^2(\sigma_{x0}(x) + \sigma_{x1}(x))\frac{h_u(x) - y}{h_u(x) - h_l(x)} +$$
$$+h_u{}'(x)^2(\sigma_{x0}(x) - \sigma_{x1}(x))\frac{y - h_l(x)}{h_u(x) - h_l(x)} \tag{2.12b}$$
$$\sigma_{xy} = h_l{}'(x)(\sigma_{x0}(x) + \sigma_{x1}(x))\frac{h_u(x) - y}{h_u(x) - h_l(x)} +$$
$$+h_u{}'(x)(\sigma_{x0}(x) - \sigma_{x1}(x))\frac{y - h_l(x)}{h_u(x) - h_l(x)} + \tilde{b}\tau(x) \tag{2.12c}$$

- **Hp3**

$$s_u(x,y) = u0(x) + \tilde{y}\frac{t(x)}{2}\theta(x) \tag{2.13a}$$

$$s_u(x,y) = v0(x) + \tilde{y}\frac{t(x)}{2}v1(x) + \tilde{b}v2(x) \tag{2.13b}$$

$$\sigma_{xx}(x,y) = \sigma_{x0}(x) + \tilde{y}\sigma_{x1}(x) \tag{2.14a}$$

$$\sigma_{yy} = \sigma_{x0}(x)(c'(x)^2 - \tilde{y}c'(x)t'(x) + \frac{t'(x)^2}{4}) + \sigma_{x1}(x)(\tilde{y}(c'(x)^2 + \frac{t'(x)^2}{4}))$$

$$-\sigma_{x1}(x)(c'(x)t'(x)) + \tilde{b}\sigma_{y1}(x) + \tilde{b}\tilde{y}\sigma_{y2}(x) \tag{2.14b}$$

$$\sigma_{xy} = c'(x)\sigma_{x0} - \frac{t(x)}{2}\sigma_{x1} + \tilde{y}(\frac{t(x)}{2}\sigma_{x0} - c'(x)\sigma_{x1}) + \tilde{b}\tau(x) \tag{2.14c}$$

where the linear function $\tilde{y}$ and the quadratic function $\tilde{b}$, introduced for convenience of representation, are defined as follow:

$$\tilde{y} = (c(x) - y)\frac{2}{t(x)} \qquad \tilde{b} = 1 - (c(x) - y)^2\frac{4}{t(x)^2} \tag{2.15}$$

In particular, function $\tilde{y}$ is equal to 1 at $h_l(x)$, 0 at $c(x)$ and -1 at $h_u(x)$. While function $\tilde{b}$ is the so-called bubble-function and it is equal to 0 at $h_u(x)$ and $h_l(x)$, and 1 at c(x).

For the illustrated hypotheses, $u0(x)$, $\theta(x)$ and v0(x) are the new displacement independent variables, while $\sigma_{x0}(x)$, $\sigma_{x1}(x)$ and $\tau(x)$ are the new stress independent variables of the problem. To enrich the beam model a greater number of variables are necessary. In fact, the last set of hypotheses (Hp3) are also characterized by v1(x) and v2(x) for the displacement field and by $\sigma_{y1}(x)$ and $\sigma_{y2}(x)$ for the stress field. As shown by the expressions reported above, for all the three models we assume that the horizontal $s_u(x,y)$ displacement and the $\sigma_{xx}(x,y)$ are linear function of y, whereas $\sigma_{xy}(x,y)$ is a quadratic function of y. Hp1 and Hp2 differentiate for the $\sigma_{yy}(x,y)$ stress component that is imposed null ("-" in Table 2.1) in the first one. For Hp3 $v_s(x,y)$ and $\sigma_{xx}(x,y)$ are a quadratic and a cubic function of y, respectively.

Starting from the weak formulation of equation (2.2) and introducing the chosen hypotheses it is possible to directly obtain the resulting ODEs systems. In the following, the systems of equations are explicitly reported for the three set of hypotheses indicated above.

- **System of ODEs for Hp1**

$$\sigma_{x0}' = -f_1 - \frac{\sigma_{x0} t'}{t}$$
$$\sigma_{x1}' = \frac{-4\tau + \sigma_{x1} t'}{t}$$
$$\tau' = \frac{-12\sigma_{x1} c'^2 + 2t'(-2\tau + 3\sigma_{x0} c') + 3t(-2f_2 - 2c'\sigma_{x0}{}' + t'\sigma_{x1}{}' - 2\sigma_{x0} c'' + \sigma_{x1} t'')}{4t}$$
$${u_0}' = \frac{-12Ev_0 c' t' + t(\sigma_{x0}(6 + 12(1+\nu)c'^2 + (1+\nu)t'^2) + 2c'(4(1+\nu)(\tau - \sigma_{x1} t') - 3E{v_0}'))}{6Et}$$
$${\theta_0}' = \frac{3Ev_0(4c'^2 + t'^2) + t(\sigma_{x1}(2 + 4(1+\nu)c'^2 + 3(1+\nu)t'^2) - t'(4(1+\nu)(\tau + 2\sigma_{x0} c')}{Et^2}$$
$$+ \frac{3E(\theta - {v_0}'))}{Et^2}$$
$${v_0}' = \frac{5E\theta + (1+\nu)(8\tau + 5(2\sigma_{x0} c' - \sigma_{x1} t'))}{5E}$$

- **System of ODEs for Hp2**

$$\sigma_{x0}' = -f_1 - \frac{\sigma_{x0} t'}{t}$$
$$\sigma_{x1}' = \frac{-4\tau + \sigma_{x1} t'}{t}$$
$$\tau' = \frac{t'(-4\tau - 6\sigma_{x0} c' + 3\sigma_{x1} t') + 3t(-2c'\sigma_{x0}' + t'\sigma_{x1}' - 2(f_2 + \sigma_{x0} c'' + \sigma_{x1} t'')}{4t}$$
$${u_0}' = \frac{\sigma_{x0}(48(1+c'^2)^2 + 8t'^2(1 - 2\nu + 5c'^2) + 3t'^4 - 16c'(-4(1+\nu)\tau)}{48E}$$
$$- \frac{16(\sigma_{x1} t'(4 + 4c'^2 + t'^2) + 3Ev_0')}{48E}$$
$${\theta_0}' = \frac{\sigma_{x1}(16(1+c'^2)^2 + 8t'^2(3 + 2\nu + 7c'^2) + t'^4) - 8t'(4(1+\nu)\tau}{8Et}$$
$$+ \frac{2\sigma_{x0} c'(4 + 4c'^2 + t'^2) + 3E(\theta - v_0'))}{8Et}$$
$${v_0}' = \frac{5E\theta + (1+\nu)(8\tau + 5(2\sigma_{x0} c' - \sigma_{x1} t'))}{5E}$$

- **System of ODEs for Hp3**

$$\sigma'_{x0} = \frac{-f_1 t - 4\sigma_{x1}c' + \sigma_{x0}t'}{t}$$
$$\sigma'_{x1} = \frac{-4\tau + \sigma_{x1}t'}{t}$$
$$\tau' = -\frac{-2t'(2\tau + 9\sigma_{x0}c') + 3\sigma_{x1}(8c'^2 + t'^2) + 3t(-2c'\sigma_{x0}{}' + t'\sigma_{x1}{}')}{4t}$$
$$+ \frac{3t(2(f_2 + \sigma_{x0}c'') - \sigma_{x1}t'')}{4t}$$
$$\sigma_{y1} = \frac{8\tau c' + \sigma_{x0}t'^2 - tt'\sigma_{x0}{}' + 2tc'\sigma_{x1}{}' + \sigma_{x1}(-2c't' + 2tc'') - t\sigma_{x0}t''}{8}$$
$$\sigma_{y2} = \frac{2t'(2\tau + 15\sigma_{x0}c') - 5\sigma_{x1}(8c'^2 + t'^2) + t(10c'\sigma_{x0}{}' - 5t'\sigma_{x1}{}' + 8\tau')}{8}$$
$$+ \frac{t(10(f_2 + \sigma_{x0}c'') - 5\sigma_{x1}t'')}{8}$$

$$u_0{}' = \frac{160Et'(-3u_0 + c'(3v_0 + 2v_2)) - 20Et^2t'v_1{}' + t(-160\nu\sigma_{y1} + 320(1+\nu)\tau c'}{240Et}$$
$$+ \frac{5\sigma_{x0}(48(1+c'^2)^2 + 8t'^2(1 - 2\nu + 5c'^2) + 3t'^4) - 4(8\sigma_{y2}c't' + 15Ev_1t'^2 - 10\sigma_{y1}(4c'^2 + t'^2))}{240Et}$$
$$+ \frac{-4(20\sigma_{x1}c't'(4 + 4c'^2 + t'^2) + 60Ec'v_0{}' + 40Ec'v_2{}')}{240Et}$$

$$\theta_0{}' = \frac{320Ec'(3u_0 - c'(3u_0 + 2v_2)) + 40Et^2c'v_1{}' + t(5\sigma_{x1}(16(1+c'^2)^2 + 8t'^2(3 + 2\nu + 7c'^2))}{40Et^2}$$
$$+ \frac{5\sigma_{x1}tt'^4 - 8(\sigma_{y2}(4\nu - 4c'^2 - t'^2) + 5t'(3E\theta + 4(1+\nu)\tau - 3Ev_1c'}{40Et^2}$$
$$+ \frac{2c'(2\sigma_{y1} + c(4 + 4c'^2 + t'^2)) - E(3v_0{}' + 2v_2{}')}{40Et^2}$$

$$v_0{}' = \frac{-2Ev_2t' + t(5E\theta + 8(1+\nu)\tau + 5c'(-Ev_1 + 2(1+\nu)\sigma_{x0}) - 5(1+\nu)\sigma_{x1}t' - 4Ev2')}{5Et}$$
$$v_1 = \frac{-16\sigma_{y1} + 20\sigma_{x1}c't' + 5\sigma_{x0}(4\nu - 4c'^2 - t'^2)}{20E}$$
$$v_2 = \frac{t(4(4\sigma_{y2} - 7\sigma_{x0}c't') + 7\sigma_{x1}(-4\nu + 4c'^2 + t'^2))}{112E}$$

For the illustrated hypotheses, $u0(x)$, $\theta(x)$ and v0(x) are the new displacement independent variables, while $\sigma_{x0}(x)$, $\sigma_{x1}(x)$ and $\tau(x)$ are the new stress independent variables of the problem. To enrich the beam model a greater number of variables are necessary. In fact, the last set of hypotheses (Hp3) are also characterized by v1(x) and v2(x) for the displacement field and by $\sigma_{y1}(x)$ and $\sigma_{y2}(x)$ for the stress field. As shown by the expressions reported above, for all the three models we assume that the horizontal $s_u(x, y)$ displacement and the $\sigma_{xx}(x, y)$ are linear function of y, wherease $\sigma_{xy}(x, y)$ is a quadratic

function of y. Hp1 and Hp2 differentiate for the $\sigma_{yy}(x, y)$ stress component that is imposed null ("-" in Table 2.1) in the first one. For Hp3 model $v_s(x, y)$ and $\sigma_{xx}(x, y)$ are a quadratic and a cubic function of y, respectively.

2.2.3 Comparison of the hypotheses considered for the NP-model

In the present Section the models correspondent to the three set of hypotheses presented before are compared, showing how the accuracy of the solution changes. From now on, NP-mod Hp1, NP-mod Hp2 and NP-mod Hp3 will indicate the models obtained adopting respectively the sef of hypotheses Hp1, Hp2 and Hp3. Furthermore, results coming from simulations carried out with the finite solver Abaqus [SIMULIA Dassault Sistèmes, 2012] are taken as reference solution for the calculus of errors. To determine the most suitable set of hypotheses for real design problems, the comparison is made considering different cases of non-prismatic beams under different load conditions.

Definition of the considered geometries

The geometries considered in the comparison are listed below and illustrated in Figure 2.2:

(i) Prismatic beam

(ii) Linearly tapered symmetric beam

(iii) Linearly tapered non-symmetric beam

(iv) Curvilinearly tapered symmetric beam

(v) Curvilinearly tapered non-symmetric beam

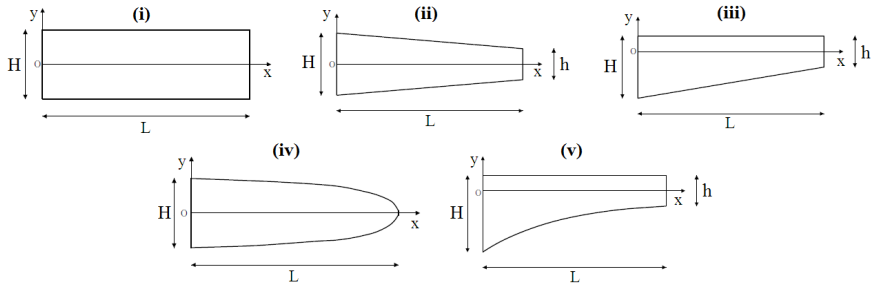

Figure 2.2. Considered geometries in the comparison of the three modeld.

Considering Figure 2.2, for all the geometries the maximum height and the minimum height of the cross-section are respectively equal to $H = 1$ m and $h = 0.5$ m. For the case (iv), the depth h at the free edge of the beam is different from zero but sufficiently small to be considered negligible. This is made because the cross-section area must be sufficiently big to transmit the shear force and an horizontal outward unit vector would

lead to a not defined stresses (see Equation (2.4)). For all the cases the length L is equal to 10 m with a slenderness $\lambda = 1/10$, which is a conventional value for slender beams. The case (v) represents the most complex geometry, because it is non-symmetric, curvilinear and less slender with a $L = 5$ m ($\lambda = 1/5$), thus with a greater taper.

Boundary conditions and considered models

For all the considered geometries, the beam studied is clamped at x=0 and subjected to a transverse concentrated load $P = -100$ kN directing downwards applied at x=L (load case A); for the non-symmetrically curvilinear beam we consider also an axial concentrated load $P = 100$ kN applied at x=L (load case B).

In order to solve the ODEs systems presented in section 2.2.2, for all the geometries under the load case A the following boundary conditions have been adopted:

$$\begin{aligned} u_0(0) &= 0 \quad & \sigma_{x0}(L) &= 0 \\ v_0(0) &= 0 \quad & \sigma_{x1}(L) &= 0 \\ \theta_0(0) &= 0 \quad & \tau(L) &= P/h \end{aligned} \tag{2.16}$$

For the curvilinearly tapered non-symmetric beam (case (v)) under the load case B the following boundary conditions have been adopted:

$$\begin{aligned} u_0(0) &= 0 \quad & \sigma_{x0}(L) &= P/h \\ v_0(0) &= 0 \quad & \sigma_{x1}(L) &= 0 \\ \theta_0(0) &= 0 \quad & \tau(L) &= 0 \end{aligned} \tag{2.17}$$

Finally, as material parameters, the values of Young's modulus $E = 10 \cdot 10^7\ kN/m^2$ and Poisson's ratio $\nu = 0.3$ are assumed. Mathematica [Mathematica, 2017] solver is adopted for the solution of the ODEs systems reported in Section 2.2.2. Substituting the expressions of $c(x)$ and $t(x)$ (which define the beam geometry) in the ODEs system the solution for each beam is easily calculated by imposing the boundary conditions (2.16) and (2.17). All the analysis have run on the same computer (Intel(R) Core(TM) i7, 8 GB of RAM, 64 bit operating system) and the computational time is always reasonable, of the order of seconds. In this study, all these systems are numerically solved but it is worth to notice that the displacement unknowns related to the NP-mod Hp1 model are also analytically available (see Balduzzi et al. [2016a]).

Solutions obtained from the three set of hypotheses are compared with those calculated with the FE software Abaqus and are considered as the reference solutions. The 2D FE over-killed analyses performed through the Abaqus software present a mesh of 4-node bi-linear CPS4R plane-stress quadrilateral elements [SIMULIA Dassault Sistèmes, 2012] characterized by an appropriate element size to obtain an accurate convergence, ensuring that the numerical error is smaller than the number of digits used to report the results.

Results of the comparison

Tables 2.2-2.7 show the results obtained from the different geometries referring to each model considered. The quantities of interest considered for the comparison are the following:

- the transverse displacement $v(L)$ evaluated at the free edge;
- the maximum value of the shear stress σ_{xy} at half length of the beam;
- the horizontal displacement $u(L)$ evaluated at the free edge (only for the load case B);
- the maximum value of the axial stress σ_{xx} at half length of the beam (only for the load case B).

As already stated, the Abaqus FE solution is considered as the reference solution. Relative errors of each considered quantity are calculated using the expression:

$$e_r = \frac{|q - q_{ABQ}|}{|q_{ABQ}|} \tag{2.18}$$

where q is the considered quantity calculated with the NP-Model (for each set of hypotheses) and q_{ABQ} the corresponding one calculated with Abaqus.

Model	v(L)[m]	$\sigma_{xy_{(x=L/2)}}[\mathrm{kN}/m^2]$	$e_v[\%]$	$e_{\sigma_{xy}}[\%]$
NP-mod Hp1	$-4.031 \cdot 10^{-3}$	$-1.500 \cdot 10^{2}$	$1.702 \cdot 10^{-1}$	$2.109 \cdot 10^{-1}$
NP-mod Hp2	$-4.031 \cdot 10^{-3}$	$-1.500 \cdot 10^{2}$	$1.702 \cdot 10^{-1}$	$2.109 \cdot 10^{-1}$
NP-mod Hp3	$-4.031 \cdot 10^{-3}$	$-1.500 \cdot 10^{2}$	$1.702 \cdot 10^{-1}$	$2.109 \cdot 10^{-1}$
Abq	$-4.024 \cdot 10^{-3}$	$-1.503 \cdot 10^{2}$		

Table 2.2. Results for prismatic beam, load case A.

Model	v(L)[m]	$\sigma_{xy_{(x=L/2)}}[\mathrm{kN}/m^2]$	$e_v[\%]$	$e_{\sigma_{xy}}[\%]$
NP-mod Hp1	$-6.578 \cdot 10^{-3}$	$-1.728 \cdot 10^{2}$	$1.218 \cdot 10^{-1}$	$2.954 \cdot 10^{1}$
NP-mod Hp2	$-6.577 \cdot 10^{-3}$	$-1.333 \cdot 10^{2}$	$1.012 \cdot 10^{-1}$	$4.648 \cdot 10^{-1}$
NP-mod Hp3	$-6.574 \cdot 10^{-3}$	$-1.333 \cdot 10^{2}$	$5.691 \cdot 10^{-2}$	$4.648 \cdot 10^{-1}$
Abq	$-6.570 \cdot 10^{-3}$	$-1.334 \cdot 10^{2}$		

Table 2.3. Results for linearly tapered symmetric beam, load case A.

Comparing the numerical solutions of the models and considering the errors respect to the FE over-killed solution and the accuracy of the hypotheses, NP-mod Hp2 and NP-mod Hp3 seem to be the more suitable models. In fact, the NP-mod Hp1 model is in line with the other ones only for the standard case of the

Model	v(L)[m]	$\sigma_{xy_{(x=L/2)}}[\mathrm{kN}/m^2]$	$e_v[\%]$	$e_{\sigma_{xy}}[\%]$
NP-mod Hp1	$-4.703 \cdot 10^{-3}$	$-3.126 \cdot 10^{2}$	$2.850 \cdot 10^{1}$	$1.716 \cdot 10^{1}$
NP-mod Hp2	$-6.586 \cdot 10^{-3}$	$-2.667 \cdot 10^{2}$	$1.157 \cdot 10^{-1}$	$2.661 \cdot 10^{-2}$
NP-mod Hp3	$-6.574 \cdot 10^{-3}$	$-2.667 \cdot 10^{2}$	$6.478 \cdot 10^{-2}$	$2.661 \cdot 10^{-2}$
Abq	$-6.578 \cdot 10^{-3}$	$-2.668 \cdot 10^{2}$		

Table 2.4. Results for linearly tapered non-symmetric beam, load case A.

Model	v(L)[m]	$\sigma_{xy_{(x=L/2)}}[\mathrm{kN}/m^2]$	$e_v[\%]$	$e_{\sigma_{xy}}[\%]$
NP-mod Hp1	$-6.287 \cdot 10^{-2}$	$-3.770 \cdot 10^{2}$	$6.968 \cdot 10^{2}$	$2.475 \cdot 10^{2}$
NP-mod Hp2	$-7.857 \cdot 10^{-3}$	$-1.076 \cdot 10^{2}$	$4.309 \cdot 10^{-1}$	$8.605 \cdot 10^{-1}$
NP-mod Hp3	$-7.855 \cdot 10^{-3}$	$-1.076 \cdot 10^{2}$	$4.540 \cdot 10^{-1}$	$8.605 \cdot 10^{-1}$
Abq	$-7.891 \cdot 10^{-3}$	$-1.085 \cdot 10^{2}$		

Table 2.5. Results for curvilinear tapered symmetric beam, load case A.

prismatic beam and the simple case of the linearly tapered symmetric beam. For both geometries, the three models present almost the same order of error except for the $e_{\sigma_{xy}}[\%]$ one, which is around 29% for the NP-mod Hp1 model.

Moving to a non-symmetric tapered configuration, it is possible to register a greater error in the NP-mod Hp1 model also in the displacement estimate. This example (see Table 2.4) underlines the effect of the simplified hypotheses on the σ_{yy} stress component in NP-mod Hp1 and the importance of the respect of the surface boundary equilibrium. Indeed, choosing $\sigma_{yy} = 0$ this equilibrium is neglected and it reflects on the extent of the displacement and the shear stress which naturally depends also on the σ_{yy} component. In a simple configuration like the linearly tapered symmetric case, the contribution of the σ_{yy} component is negligible thus the use of the the NP-mod Hp1 model can be acceptable for the estimate of the displacements; tackling slightly more complex cases, as the non-symmetric cor-

Model	v(L)[m]	$\sigma_{xy_{(x=L/2)}}[\mathrm{kN}/m^2]$	$e_v[\%]$	$e_{\sigma_{xy}}[\%]$
NP-mod Hp1	$-1.879 \cdot 10^{-2}$	$-4.075 \cdot 10^{2}$	$5.596 \cdot 10^{1}$	$5.559 \cdot 10^{0}$
NP-mod Hp2	$-1.210 \cdot 10^{-3}$	$-3.840 \cdot 10^{2}$	$2.519 \cdot 10^{-1}$	$5.496 \cdot 10^{-1}$
NP-mod Hp3	$-1.208 \cdot 10^{-3}$	$-3.840 \cdot 10^{2}$	$1.133 \cdot 10^{-1}$	$5.496 \cdot 10^{-1}$
Abq	$-1.207 \cdot 10^{-3}$	$-3.861 \cdot 10^{2}$		

Table 2.6. Results for curvilinear tapered non-symmetric beam, load case A.

Model	v(L)[m]	$\sigma_{xy_{(x=L/2)}}[\mathrm{kN}/m^2]$	$e_v[\%]$	$e_{\sigma_{xy}}[\%]$
NP-mod Hp1	$-3.999 \cdot 10^{-5}$	$7.509 \cdot 10^{0}$	$5.971 \cdot 10^{0}$	$1.996 \cdot 10^{1}$
NP-mod Hp2	$-3.780 \cdot 10^{-5}$	$6.400 \cdot 10^{0}$	$1.547 \cdot 10^{-1}$	$2.259 \cdot 10^{0}$
NP-mod Hp3	$-3.755 \cdot 10^{-5}$	$6.400 \cdot 10^{0}$	$5.153 \cdot 10^{-1}$	$2.259 \cdot 10^{0}$
Abq	$-3.7741 \cdot 10^{-5}$	$6.259 \cdot 10^{0}$		

Model	u(L)[m]	$\sigma_{xx_{(x=L/2)}}[\mathrm{kN}/m^2]$	$e_u[\%]$	$e_{\sigma_{xx}}[\%]$
NP-mod Hp1	$1.229 \cdot 10^{-5}$	$2.449 \cdot 10^{2}$	$1.429 \cdot 10^{0}$	$4.143 \cdot 10^{0}$
NP-mod Hp2	$1.215 \cdot 10^{-5}$	$2.560 \cdot 10^{2}$	$2.508 \cdot 10^{-1}$	$1.875 \cdot 10^{-1}$
NP-mod Hp3	$1.214 \cdot 10^{-5}$	$2.560 \cdot 10^{2}$	$1.321 \cdot 10^{-1}$	$1.875 \cdot 10^{-1}$
Abq	$1.212 \cdot 10^{-5}$	$2.555 \cdot 10^{2}$		

Table 2.7. Results for curvilinear tapered non-symmetric beam, load case B.

responding one, the influence of the σ_{yy} component in determining displacement and stresses is significant and can not be neglected. Focusing on NP-mod Hp2 and NP-mod Hp3 models, the use of the latter one does not lead to a significant improvement in terms of percentage of error if compared with the former one. Furthermore, NP-mod Hp2 equations are easily understandable and less complex than those related to NP-mod Hp3. Thus, from now on, the set of hypotheses Hp2 is adopted since considered reasonably efficient for the purpose of the work.

3 NP-Model in real design problems

Focusing on the evaluation of the non-prismatic elements stiffness matrix, Chapter 3 presents the potential of the NP-model when applied to real design problems. To underline the practical value of the present work, the handled examples are also analyzed with the well-known software SAP2000 [Computer & Structures Inc., 2011], taken as example in the wide range of building-oriented programs. As many structural engineers work daily with such programs it is extremely useful to evaluate the accuracy of the software output when compared with the solution obtained with a rigorous model reported in literature. Furthermore, results coming from simulations carried out with the FE solver Abaqus [SIMULIA Dassault Sistèmes, 2012] are taken as reference solution for the calculus of errors.

Chapter 3 is organized as follows. Section 3.1 summarizes the assumptions considered for the NP-Model, the method of approximations available for non-prismatic beams in the software SAP2000 and the modeling approach adopted in Abaqus. Section 3.2 studies the stiffness matrix evaluation problem at the *element-scale* through a parametric study made on a non-symmetric tapered beam, useful also to validate the proposed model. In parallel, focusing on RC tapered members, Section 3.3 analyzes the problem at the *frame-scale* with the description of a 2D-frame considered as case study. Here, a comparison of the results obtained from the different modeling strategies of the 2D-frame is illustrated. For the considered cases, stiffness matrix coefficients, displacements and stresses are recovered. Finally, some conclusions and future developments are reported.

3.1 Adopted modeling approaches

The present part resumes the main steps of the NP-Model (Section 3.1.1), describes how the modeling of non-prismatic beams can be treated in SAP2000 (Section 3.1.2), and reports our modeling approach of such beams through the use of Abaqus (Section 3.1.3).

3.1.1 Modeling of non-prismatic beams with the NP-model

In finding the stiffness matrix for a generic tapered beam, the governing differential equations (refer to the ODEs system for the set of hypotheses Hp2, Section 2.2.2) are solved using the appropriate boundary conditions (displacement based approach). Then stress solutions are used to compute beam characteristic forces

(N, T, M). Stiffness matrix coefficients are associated to the set of nodal degrees of freedom (DOFs) and sign convention reported in Figure 3.1. In particular, we assume that the unknown vector $\underline{\hat{\mathbf{u}}}$ and the load vector $\underline{\mathbf{f}}$ of the stiffness equation are in the form:

$$\underline{\mathbf{K}} \cdot \underline{\hat{\mathbf{u}}} = \underline{\mathbf{f}} \tag{3.1}$$

with:

$$\underline{\hat{\mathbf{u}}} = \left\{ \hat{u}_1 \quad \hat{v}_1 \quad \hat{\theta}_1 \quad \hat{u}_2 \quad \hat{v}_2 \quad \hat{\theta}_2 \right\} \tag{3.2a}$$

$$\underline{\mathbf{f}} = \left\{ N_1 \quad V_1 \quad M_1 \quad N_2 \quad V_2 \quad M_2 \right\} \tag{3.2b}$$

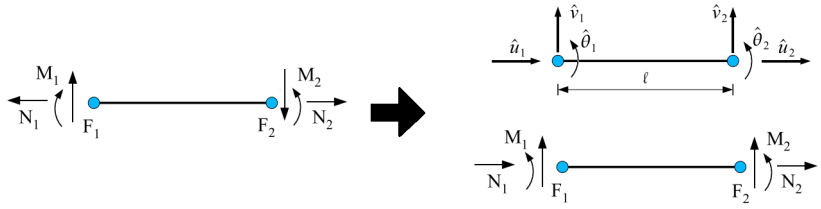

Figure 3.1. Set of nodal DOFs and sign convention.

3.1.2 Modeling of non-prismatic beams with SAP2000

The software SAP2000 is a general building-oriented FE program, thus it allows to choose among 1D, 2D, and 3D (solids, shell) elements for the modeling. Nevertheless, in common practice, the element type most frequently used to model beams, columns, braces, and trusses both in planar and 3D systems is the *frame element* (1D) since efficient and computationally economic. Thus, within the present study, we will focus on 1D elements.

According to the CSI Analysis Reference Manual for SAP2000 [Computer & Structures Inc., 2011], cross-sections are defined independently from the frame element and then assigned to the element. In particular, for non-prismatic beams, properties may vary along the element length by interpolating the values assigned at the two ends, referring to two or more previously defined cross-section geometries. Within the subtopic "Non-prismatic Sections" of the cited manual, we can find details on how cross-section features are used to define non-prismatic members. The properties for a segment are:

- cross-section properties at the extremities of the segment;

- segment length specified as either a variable length or an absolute length;
- variation of bending stiffness which can be linear, quadratic and cubic.

Regarding the remaining properties (axial and shear stiffness, mass and weight), they are assumed to vary linearly between the ends of each segment. The user may also specify the element length is divided into any number of segments without needing to be set of equal length. Even this option could be seen as an advantage, it is well known that the straightforward technique of dividing a tapered beam into a number of uniform elements is scarcely efficient and inaccurate [Zeinali et al., 2013]. In conclusions, in SAP2000 the modeling of non-prismatic beams adopting frame elements could be seen as an approximation which simply takes into account variable properties of the beam [Tena-Colunga and Becerril, 2012].

3.1.3 Modeling of non-prismatic elements with Abaqus

We now introduce the use of the FE software Abaqus for the modeling of non-prismatic beams, software which is used to construct the reference solution for the problems investigated in Sections 3.2 and 3.3. To facilitate the understanding of the adopted modeling strategy, Figure 3.2 introduces the concepts of 1D-scheme and 2D-scheme to respectively indicate a discretization scheme with 1D and 2D elements.

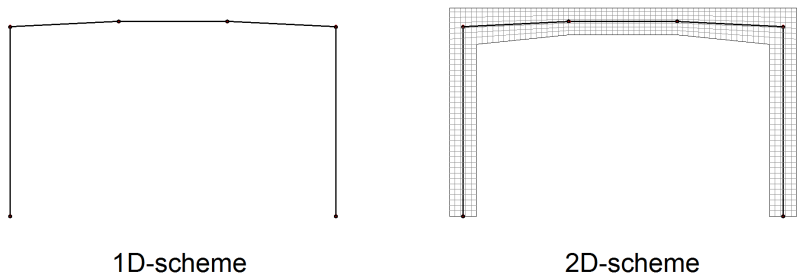

Figure 3.2. 1D-scheme and 2D-scheme discretization strategies.

For the parametric study at the *element-scale* (see Section 3.2), the Abaqus solution is obtained discretizing the chosen geometry with 4-node bilinear CPS4R plane-stress quadrilateral elements [SIMULIA Dassault Sistèmes, 2012] (2D-scheme, Figure 3.2). Then, we obtain the stiffness matrix of the global beam or column simply applying the displacement based approach and recovering the nodal quantities and the two ends.

With respect to the analysis at the *frame-scale* (see Section 3.3) both in the studied NP-Model and in SAP2000 the frame is schematized with 1D elements

connected by nodes in which there is continuity (1D-scheme, Figure 3.2). To consider comparable structural problems we adopt the same procedure in the Abaqus model. We calculate elementary stiffness matrices for each element of the frame (beam portions or columns) starting from the 2D-scheme, then proceeding with the recovery of nodal quantities as in the 1D-scheme adopted in the NP-Model and in SAP2000. In fact, considering the 2D-scheme for the *frame-scale* problem in Abaqus leads to take into account some effects whose inclusion in the NP-Model and in SAP2000 is not trivial and requires a careful modeling. For example, the effect of the stiffening of the beam-column connections, which would be considered in the Abaqus 2D-scheme, requires some particular considerations due to the tapered portions (see as example [Balkaya, 2001]). In this paper we neglect the modeling of connections, being aware that the integration of this aspect should be considered in a future work.

3.2 Stiffness matrix evaluation at the element-scale

Here in the following, the stiffness matrix accuracy is tested by studying the problem at the *element-scale* and comparing the three modeling approaches presented in Section 3.1.

3.2.1 Parametric study on a non-symmetric tapered beam geometry

For the parametric study presented in this section, among the possible geometries, a non-symmetric tapered beam as in Figure 3.3 is chosen. The parametric study is reported for a non-symmetric tapered beam because this specific geometry also recurs in the 2D-frame analyzed in Section 3.3. To study the NP-Model and SAP2000 accuracy, the obtained results have been compared with those calculated with the FE software Abaqus.

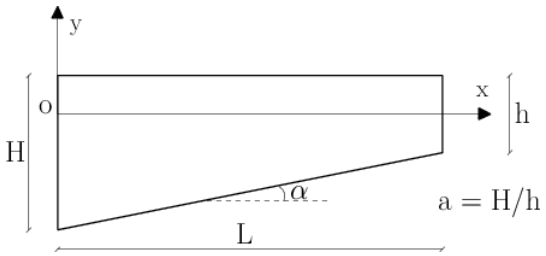

Figure 3.3. Non-symmetric tapered beam geometry.

The parametric study consists in varying the taper ratio expressed as $a = H/h$, where H is the maximum height and h is the minimum height of the cross-section.

We consider different values of the parameter a to explore if a progressive taper could influence the stiffness matrix accuracy. For each value of the parameter a we perform two analysis, considering the case of a slender beam ($H/L = 1/10$) and the case of a squat beam ($H/L = 1/5$). The angles between the lower edge of the beam and the horizontal axis (indicated in Figure 3.3 with the generic symbol α), are α_1 and α_2 respectively for the slender and the squat beam cases. Table 3.1 summarizes characteristics of the 16 considered cases. Moving from one case to another, the height H is kept constant while the minimum height h is variable.

H [m]	h [m]	a [-]	α_1 [◦]	α_2 [◦]
0.4	0.4	1	0	0
0.4	0.32	1.25	1.2	2.3
0.4	0.2666	1.5	1.9	3.8
0.4	0.2286	1.75	2.5	4.9
0.4	0.2	2	2.9	5.7
0.4	0.1	4	4.3	8.5
0.4	0.0666	6	4.8	9.5
0.4	0.05	8	5	10

Table 3.1. Summary of the studied geometries varying a for the slender and the squat beam cases.

In the following, we compute the average error of the stiffness matrices for the three models, respectively indicated with $\boldsymbol{K_{NPM}}$ (NP-Model), $\boldsymbol{K_{ABQ}}$ (Abaqus) and $\boldsymbol{K_{SAP}}$ (SAP2000).

The average error of the stiffness matrix relating to each single case is evaluated through the sum of all component relative errors, i.e.:

$$er_m = \sum_{i,j=1..N} (k_{er})_{i,j} \tag{3.3}$$

in which $(k_{er})_{i,j}$ is the component relative error, i.e.:

$$(k_{er})_{i,j} = \frac{|k_{NPM_{i,j}} - k_{ABQ_{i,j}}|}{|k_{ABQ_{i,j}}|} \tag{3.4}$$

where $k_{NPM_{i,j}}$ (substituted with $k_{SAP_{i,j}}$ when the SAP2000 relative errors are evaluated) is the generic coefficient of $\boldsymbol{K_{NPM}}$ and $k_{ABQ_{i,j}}$ is the corresponding coefficient of $\boldsymbol{K_{ABQ}}$. The k_{er} error is calculated for all elements of the stiffness matrices and for each of the 16 considered cases.

It is interesting to observe that we adopt expression (3.3) with the goal of properly

weight the relative error of each single stiffness component. For this reason we do not use the more classical mathematically-appropriate matrix norms (such as L_1 or L_2). Figures 3.4 shows the NP-Model and SAP2000 average errors, varying the parameter a from 1 (prismatic beam) to 8 (very tapered beam) for slender beams ($H/L = 1/10$) and squat beams ($H/L = 1/5$). The error made with the NP-Model is very low and it increases moving from the constant section to the tapered section. On the other hand, even if the trend is very similar, the order of magnitude of the error made with SAP2000 is about four times greater. According to the illustrated results, in both cases, the errors are generally greater in the squat beam case, as expected. It can be noticed a significant increase of the error going from $a = 1$ (prismatic beam) to the first tapering value $a = 1.25$ (tapered beam); once the value of 1.25 is exceeded the trend flattens and the value of the average error remains around the value of 1 and 4, respectively for the NP-Model and SAP2000. In fact, results do not seem to be strongly influenced by the taper ratio a after exceeding the value 1 corresponding to the constant cross-section case.

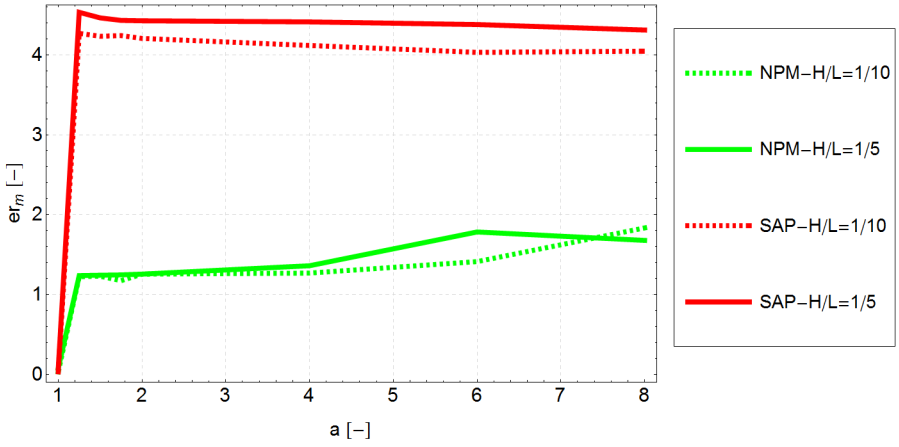

Figure 3.4. NP-Model and SAP2000 stiffness matrix average error varying the taper ratio $a = H/h$, for slender beams ($H/L = 1/10$) and squat beams ($H/L = 1/5$).

It is worth to recall that the average error er_m comes from the sum of all the 36 relative errors calculated for each coefficient of the matrix and that an average error of 1 represent a good value, as the following discussion will highlight. Generally, we can conclude that the NP-Model response better approximates the reference solution calculated with Abaqus.

3.2.2 Explicit stiffness matrix of a non-symmetric tapered beam

We explicitly report the stiffness matrix coefficients of a non-symmetric tapered beam obtained respectively with the NP-Model ($\boldsymbol{K_{NPM}}$), Abaqus ($\boldsymbol{K_{ABQ}}$) and SAP2000 ($\boldsymbol{K_{SAP}}$). This explicit comparison is made to understand where differences between the NP-Model and SAP2000 stiffness matrix evaluation come from and explore the results presented in Figure 3.4.

The geometry we refer is one of the case reported in Table 3.1, in particular we consider $a = 2$ and $H/L = 1/5$. For the specific considered case, the stiffness matrices are:

$$\boldsymbol{K_{NPM}} = \begin{bmatrix} 861480 & & & & & \\ 41152 & 19697 & & & & \\ \mathbf{-2743} & 23564 & 36968 & & & \\ -861480 & -41152 & 2743 & 861480 & & \\ -41152 & -19697 & -23564 & 41152 & 19697 & \\ \mathbf{-1102} & 11714 & 10434 & 1102 & -11714 & 13105 \end{bmatrix}$$

$$\boldsymbol{K_{ABQ}} = \begin{bmatrix} 860686 & & & & & \\ 40896 & 19621 & & & & \\ \mathbf{-2938} & 23488 & 36880 & & & \\ -860686 & -40896 & 2938 & 860686 & & \\ -40896 & -19621 & -23488 & 40896 & 19621 & \\ \mathbf{-1339} & 11666 & 10388 & 1339 & -11666 & 13077 \end{bmatrix}$$

$$\boldsymbol{K_{SAP}} = \begin{bmatrix} 862425 & & & & & \\ 42236 & 19813 & & & & \\ \mathbf{-1180} & 23603 & 36876 & & & \\ -862425 & -42236 & 1180 & 862425 & & \\ -42236 & -19814 & -23603 & 42236 & 19814 & \\ \mathbf{-590} & -11801 & 10449 & 590 & -11801 & 13214 \end{bmatrix}$$

From an inspection of the matrix coefficients, we can observe that the diagonal term values are in very good correlation and there are no significant differences with the $\boldsymbol{K_{ABQ}}$ matrix. On the contrary, the off-diagonal terms of the $\boldsymbol{K_{SAP}}$ matrix are quite different when compared to the correspondent in $\boldsymbol{K_{ABQ}}$. This behavior reflect on the trend of the stiffness matrix average error illustrated in Figure 3.4. Considering the error corresponding to $a = 2$ for the $H/L = 1/5$ NP-Model curve, the relative error of each coefficient remains always lower than 1%. This is true except for the bold off-diagonal terms in the matrices correspondent to the coupling stiffness between the translational and the rotational DOFs which present larger errors (around 10%). While, SAP2000 errors calculated for the same

matrix coefficients reach values around the 50%.

The off-diagonal terms error can be justified from the fact that we consider non-symmetric geometries and by the definition of non-prismatic beams in SAP2000 when frame elements are choosen for the modeling. Referring to the instructions given in [Computer & Structures Inc., 2011] and resumed in Section 3.1, for each element we can only define cross-section properties at the two ends to obtain a variable cross-section along the beam. In particular, there are no further options which take into account the slope of the center-line in case of non-symmetric geometries. The unique possibility is to draw an inclined element (see Figure 3.5(b)) which practically means starting from an initial symmetric configuration (see Figure 3.5(a)) and rotating it by the proper angle α. In this case, the program calculates the stiffness matrix of the asymmetric beam simply rotating the matrix correspondent to the symmetric one. In fact, we can exactly recover the matrix indicated above as $\boldsymbol{K_{SAP}}$ by applying:

$$\boldsymbol{K_{SAP}} = \boldsymbol{R^T K_{Orig} R} \tag{3.5}$$

where $\boldsymbol{K_{Orig}}$ is the stiffness matrix of the symmetric beam and $\boldsymbol{R}$ is the rotation matrix. This approximation naturally leads to the errors underlined here and in Section 3.2.1, because the considerations made in Section 2.1.1 about the different behavior of prismatic and non-prismatic beams are neglected.

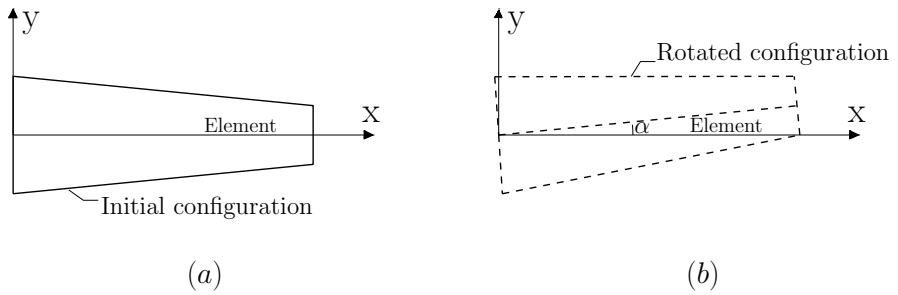

Figure 3.5. Rotation from a symmetric tapered beam (a) to a non-symmetric tapered beam (b).

3.3 2D RC frame with non-prismatic beams

In the present Section the study of a more realistic structural problem, in particular a RC frame, is reported to illustrate a real case in which the model under investigation is compared with the commercial software SAP2000 and Abaqus.

Due to the difficulties linked to the correct modeling of non-prismatic beams, commercial software started to include such elements in their libraries only from

the early 2000s. Since then, the use of these programs in problems involving non-prismatic members is worldwide diffused among practitioners. In the research field, some authors use these programs to validate their models, as in the recent paper by Zeinali et al. [2013]. Here, a Chebyshev polynomial approach is used to solve differential equations comparing results with those obtained from SAP2000. As in the present work, some others researchers focused their attention on the study of software's accuracy as in the proceeding of Tena-Colunga and Becerril [2012]. The authors evaluate how accurate is the solution obtained with the structural software ETABS and STAAD-Pro when haunched beam problems are studied, comparing results with those from traditional beam theories. Although the work is quite recent and the parametric study accurate, the comparison is made including standard stiffness coefficients taken from Tena-Colunga [1996] in which, again, the stress coupling effect is not considered.

3.3.1 Description of the studied 2D RC frame

In the following, we analyze a 2D RC frame having haunched members and characterized by three stories and two bays. The considered frame is part of a building with a public destination of use, localized in an area classified as "ZONA I" for the seismic hazard. For the design hypotheses we refer to the Italian [NTC, D.M. January 14 and 2008] and the European [Eurocode 2, 2004, Eurocode 8, 2004] normative codes.

Table 3.2 summarizes material properties while Figure 3.6 shows the main dimensions of the structure and the geometry of the tapered portions. For the columns we assume a constant section over the height of 50cm x 30cm.

Reinforced concrete class	$C28/35$
Young modulus E $[kN/m^2]$	32300000
Poisson's ratio ν	0.2
Density ρ $[kN/m^3]$	25

Table 3.2. Material properties.

The adopted analysis method is the linear static analysis. Accordingly, distributed vertical loads are calculated considering the dead loads and the destination of use of the building; for the seismic contribute a triangular distribution of static horizontal forces is applied to the frame. In Figure 3.7 we report the resulting values for the distributed load and the horizontal forces. In terms of load combinations we use the safety factors provided in NTC [D.M. January 14 and 2008] for the seismic combination at the ultimate limit state. We want to notice that it is important to consider the decoupled combinations of horizontal and vertical distributed loads to underline if the type of load can determines a different model

response in the software respect to the NP-Model. To sum up, the analyzed load combinations are:

- **COMB1** : only horizontal forces;
- **COMB2** : only vertical distributed load;
- **COMB3** : combination of horizontal and vertical loads.

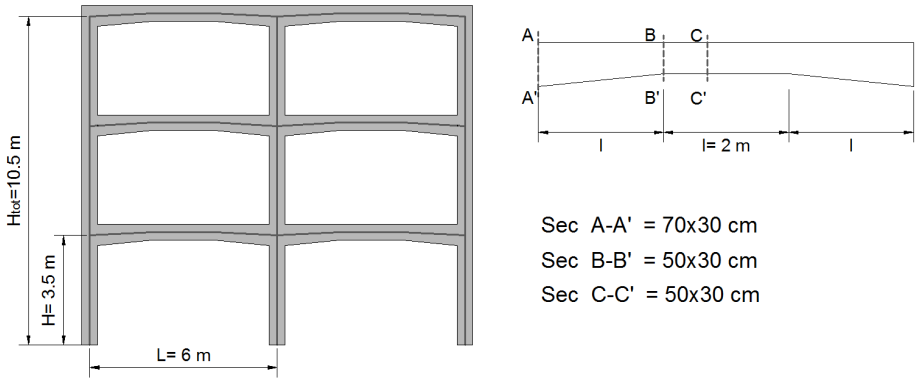

Figure 3.6. Geometry of the studied RC frame.

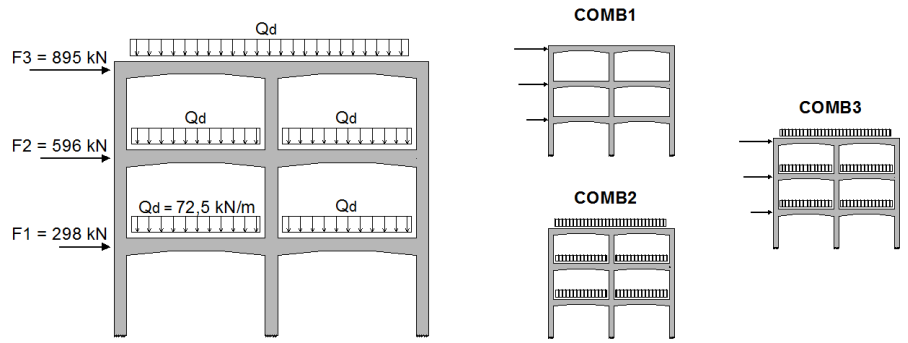

Figure 3.7. Applied lateral and vertical loads for the three-story RC frame and corresponding load combinations.

3.3.2 Comparison of the numerical results

In this Section we analyze results obtained for the 2D RC frame analysis, particularly comparing the following quantities:

- Element forces and moments
- Nodal displacements and rotations
- Stresses on the tapered portion

Results from the NP-Model and SAP2000 software are compared with the results obtained with Abaqus, which represents the reference solution. Relative errors of each considered quantity are calculated using the expression:

$$e_r = \frac{|q - q_{ABQ}|}{|q_{ABQ}|} \tag{3.6}$$

where q is the considered quantity (alternatively for the NP-Model and SAP2000) and q_{ABQ} the corresponding one calculated with Abaqus.

Element forces and moments

In reporting results of the element forces and moments we consider as representative beam the continuous one corresponding to the first storey of the first bay, from now on identified as *RBeam* (Figure 3.8 (a)). This choice comes from the fact that this beam is one of the most stressed in the structure thus more interesting to analyze. In correspondence of the columns (having prismatic cross-sections) the errors calculated with the NP-Model and SAP2000 are comparable and always under the 1%. For this reason it is not considered necessary to report forces and moments related to column elements.

Figures 3.9-3.17 show the NP-Model, Abaqus and SAP2000 diagrams of internal forces (axial, shear, and moment, respectively) for the three load combinations and the corresponding trend of the relative error. From the performed analysis we can do the following observations:

- Analyzing results from COMB1 we can notice that there are not significant differences between the NP-Model and SAP2000 response for the case of horizontal forces. This is evident from the element forces comparison where the maximum error reached is around 4-5%, which corresponds to the axial and shear action values.
- Paying attention on COMB2, from the element forces point of view Figures 3.12-3.14 show a very good correlation between NP-Model and Abaqus results. Significant relative errors, instead, can be noticed from the side of SAP2000 results. Considerable errors with the maximum going from around

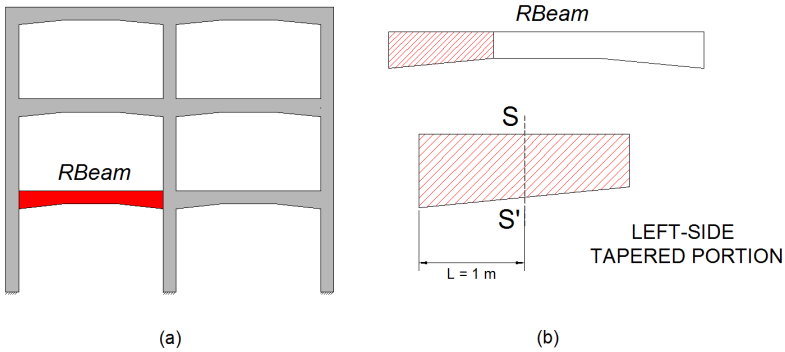

Figure 3.8. *RBeam* representative continuos beam (a); left-side non-prismatic portion of the *RBeam* (b).

25% to 70% are concentrated at the beam level (having non-prismatic cross-section portions). Most likely, the differences come from the fact that the distributed vertical load generates on beams forces and moments directly related to the approximation of the tapered element, highlighting the issues on the SAP2000 stiffness matrix evaluation described in Section 3.2.2.

- Results from COMB3 confirm that is the distributed vertical load which leads to an effective different behavior between the SAP2000 and NP-Model approaches. From the design point of view, results from horizontal-vertical load are also interesting since there is the coupling of the effects of the two load conditions.

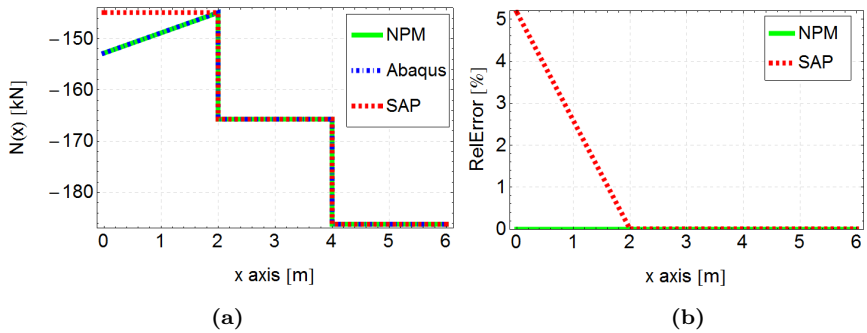

Figure 3.9. COMB1: NP-Model, Abaqus and SAP2000 axial diagrams for RBeam (a); NP-Model and SAP2000 relative errors considering Abaqus as reference solution (b).

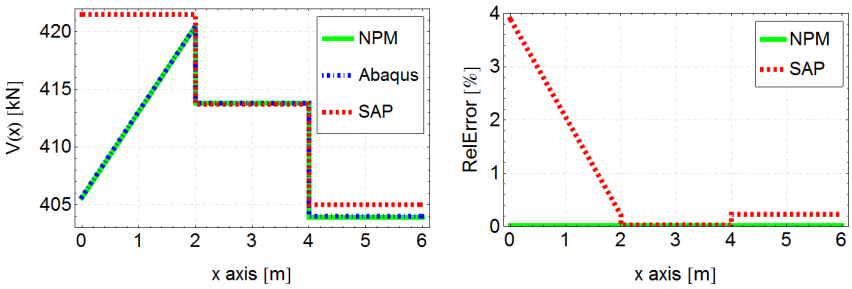

(a) (b)

Figure 3.10. COMB1: NP-Model, Abaqus and SAP2000 shear diagrams for RBeam (a); NP-Model and SAP2000 relative errors considering Abaqus as reference solution (b).

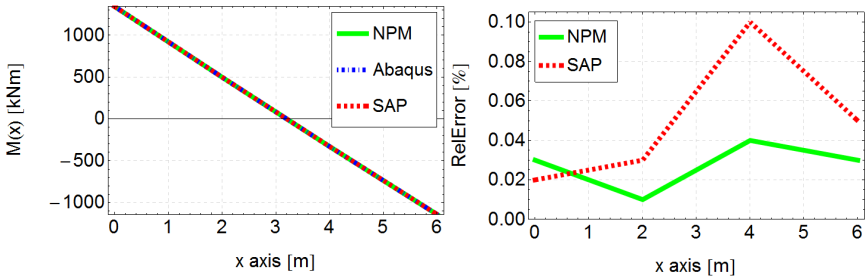

(a) (b)

Figure 3.11. COMB1: NP-Model, Abaqus and SAP2000 moment diagrams for RBeam (a); NP-Model and SAP2000 relative errors considering Abaqus as reference solution (b).

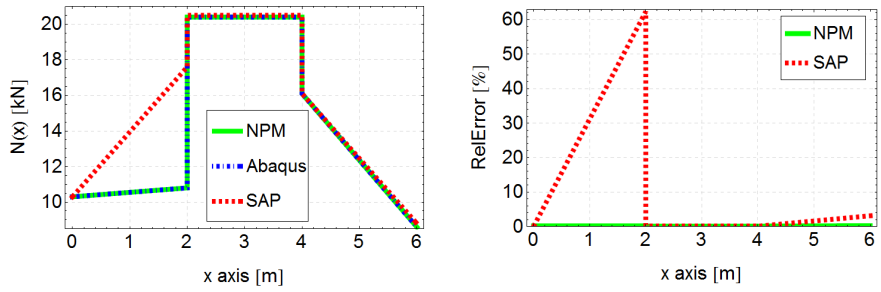

(a) **(b)**

Figure 3.12. COMB2: NP-Model, Abaqus and SAP2000 axial diagrams for RBeam (a); NP-Model and SAP2000 relative errors considering Abaqus as reference solution (b).

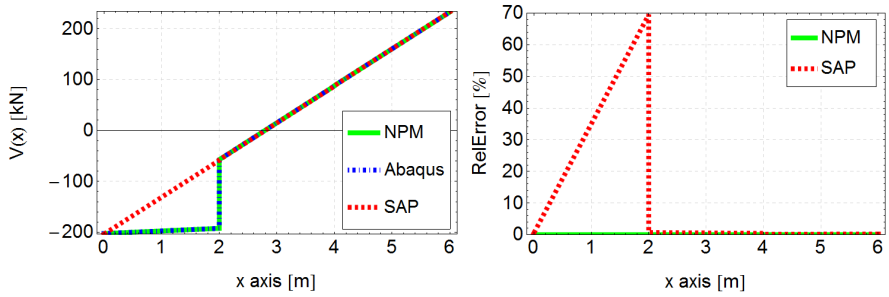

(a) **(b)**

Figure 3.13. COMB2: NP-Model, Abaqus and SAP2000 shear diagrams for RBeam (a); NP-Model and SAP2000 relative errors considering Abaqus as reference solution (b).

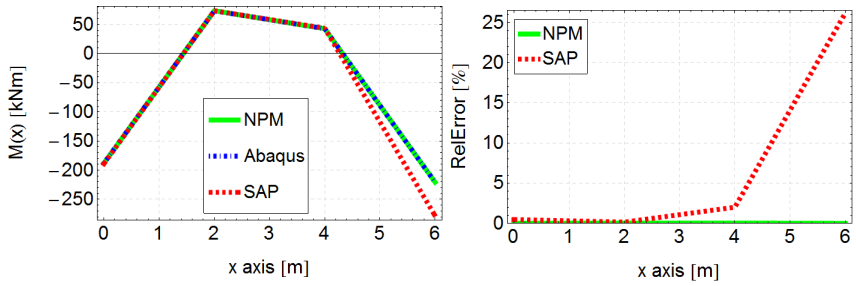

(a) **(b)**

Figure 3.14. COMB2: NP-Model, Abaqus and SAP2000 moment diagrams for RBeam (a); NP-Model and SAP2000 relative errors considering Abaqus as reference solution (b).

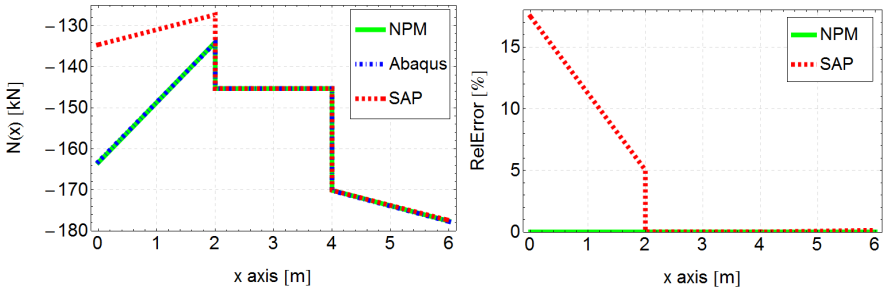

(a) **(b)**

Figure 3.15. COMB3: NP-Model, Abaqus and SAP2000 axial diagrams for RBeam (a); NP-Model and SAP2000 relative errors considering Abaqus as reference solution (b).

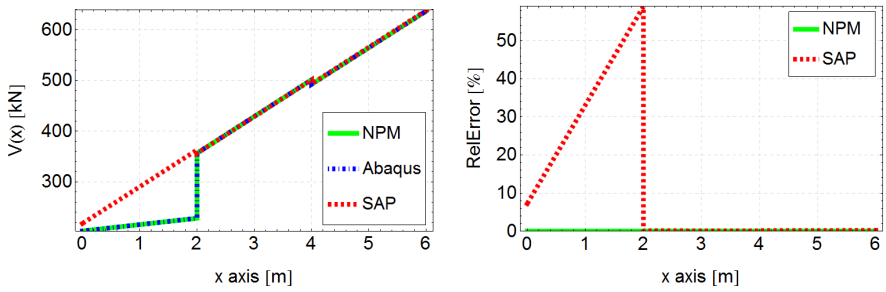

(a) **(b)**

Figure 3.16. COMB3: NP-Model, Abaqus and SAP2000 axial diagrams for RBeam (a); NP-Model and SAP2000 relative errors considering Abaqus as reference solution (b).

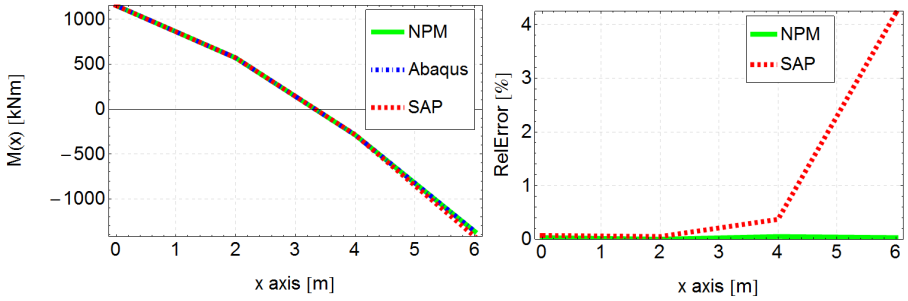

(a) **(b)**

Figure 3.17. COMB3: NP-Model, Abaqus and SAP2000 moment diagrams for RBeam (a); NP-Model and SAP2000 relative errors considering Abaqus as reference solution (b).

Nodal displacements and rotations

Referring to displacements and rotations, we observe a general good correlation between output obtained with the NP-Model and SAP2000. Tables 3.3-3.5 report NP-Model and SAP2000 relative errors of nodal displacements and rotations for the three considered load combinations. To facilitate the comprehension of Tables 3.3-3.5, Figure 3.18 shows a scheme of the numbering of elements and nodes of the frame model. As illustrated by the arrows in the left-hand side of Figure 3.18 , we consider the bottom-up positive orientation for the column elements, and the orientation from left to right for the beam elements.

Looking at the solution coming from COMB1 (Table 3.3), SAP2000 errors are slightly greater than NP-Model errors but at the same time not significant considering also the entity of the measured displacements and rotations. Results from COMB3 (Table 3.5) show that the extent and the distribution of the errors remains close to the horizontal one, since the predominant effect depends on the action of the horizontal forces.

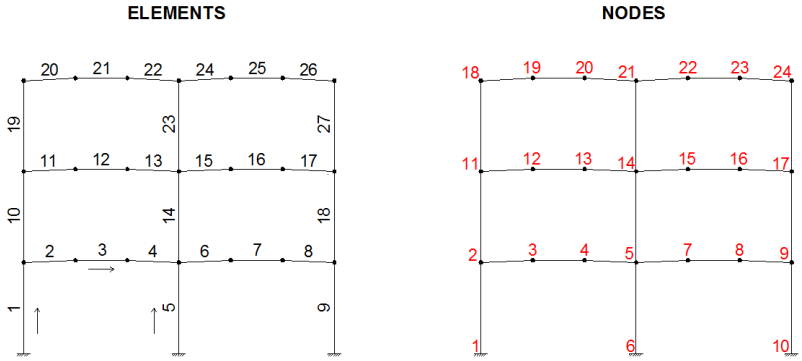

Figure 3.18. Numbering of elements and nodes for the studied frame.

	Displ. NPM			Displ. SAP			NPM Rel. Errors			SAP Rel. Errors		
Node	u	v	r	u	v	r	u_{err}	v_{err}	r_{err}	u_{err}	v_{err}	r_{err}
-	[mm]	[mm]	[rad]	[mm]	[mm]	[rad]	[%]	[%]	[%]	[%]	[%]	[%]
1	0.0	0.0	0.00	0.0	0.0	0.00	-	-	-	-	-	-
2	35.7	0.6	-0.01	35.7	0.7	-0.01	0.26	0.15	0.22	0.28	0.21	0.25
3	36.0	-6.5	0.00	36.0	-6.4	0.00	0.26	0.18	0.32	0.24	0.44	2.43
4	35.9	1.3	0.00	35.9	1.3	0.00	0.26	0.02	0.07	0.24	1.26	0.94
5	35.8	0.0	-0.01	35.8	0.0	-0.01	0.26	0.07	0.23	0.27	1.06	0.35
6	0.0	0.0	0.00	0.0	0.0	0.00	-	-	-	-	-	-
7	35.8	-1.2	0.00	35.8	-1.2	0.00	0.26	0.06	0.06	0.24	1.99	0.87
8	35.8	6.6	0.00	35.8	6.5	0.00	0.26	0.17	0.37	0.24	0.33	2.60
9	35.3	-0.7	-0.01	35.4	-0.7	-0.01	0.26	0.15	0.22	0.28	0.17	0.24
10	0.0	0.0	0.00	0.0	0.0	0.00	-	-	-	-	-	-
11	78.5	1.0	-0.01	78.6	1.0	-0.01	0.26	0.16	0.24	0.28	0.13	0.29
12	78.7	-4.3	0.00	78.7	-4.3	0.00	0.25	0.23	0.25	0.26	0.67	2.03
13	78.5	1.9	0.00	78.5	1.9	0.00	0.25	0.01	0.09	0.26	0.42	1.11
14	78.2	0.0	0.00	78.3	0.0	0.00	0.26	0.04	0.23	0.28	0.86	0.32
15	78.3	-1.6	0.00	78.3	-1.6	0.00	0.25	0.07	0.05	0.26	1.43	0.95
16	78.2	4.5	0.00	78.2	4.5	0.00	0.25	0.20	0.36	0.26	0.30	2.46
17	77.8	-1.0	-0.01	77.9	-1.0	-0.01	0.26	0.16	0.24	0.28	0.20	0.27
18	105.9	1.1	0.00	105.9	1.1	0.00	0.26	0.16	0.28	0.28	0.20	0.34
19	105.8	-1.6	0.00	105.8	-1.6	0.00	0.26	0.40	0.24	0.28	1.48	2.22
20	105.5	0.9	0.00	105.6	0.9	0.00	0.26	0.14	0.11	0.28	0.86	1.33
21	105.3	0.0	0.00	105.3	0.0	0.00	0.26	0.04	0.24	0.28	0.83	0.35
22	105.2	-0.5	0.00	105.2	-0.4	0.00	0.26	0.04	0.02	0.28	3.02	0.80
23	105.1	2.2	0.00	105.1	2.2	0.00	0.26	0.24	0.91	0.28	0.11	5.22
24	104.9	-1.1	0.00	104.9	-1.1	0.00	0.26	0.16	0.27	0.28	0.19	0.28

Table 3.3. COMB1: NP-Model and SAP2000 errors on nodal displacements and rotations.

	Displ. SAP			**Displ. NPM**			**SAP Rel. Errors**			**NPM Rel. Errors**		
Node	**u**	**v**	**r**	**u**	**v**	**r**	u_{err}	v_{err}	r_{err}	u_{err}	v_{err}	r_{err}
-	[mm]	[mm]	[rad]	[mm]	[mm]	[rad]	[%]	[%]	[%]	[%]	[%]	[%]
1	0.0	0.0	0.00	0.0	0.0	0.00	-	-	-	-	-	-
2	-0.2	-0.4	0.00	-0.2	-0.4	0.00	0.13	0.16	0.25	3.78	0.41	0.41
3	-0.1	-2.5	0.00	-0.1	-2.5	0.00	0.16	0.35	0.17	4.21	0.78	2.02
4	-0.1	-2.4	0.00	-0.1	-2.4	0.00	0.23	0.35	0.11	3.89	1.78	0.60
5	0.0	-1.0	0.00	0.0	-1.0	0.00	0.26	0.16	0.22	0.00	4.50	0.00
6	0.0	0.0	0.00	0.0	0.	0.00	-	-	-	-	-	-
7	0.1	-2.4	0.00	0.1	-2.4	0.00	0.24	0.35	0.11	5.46	1.78	0.61
8	0.1	-2.5	0.00	0.1	-2.5	0.00	0.17	0.35	0.17	5.26	0.78	2.02
9	0.2	-0.4	0.00	0.2	-0.4	0.00	0.13	0.16	0.25	4.37	0.42	0.39
10	0.0	0.0	0.00	0.0	0.0	0.00	-	-	-	-	-	-
11	-0.2	-0.7	0.00	-0.2	-0.7	0.00	0.16	0.16	0.30	4.06	0.37	1.02
12	-0.1	-2.8	0.00	-0.1	-2.8	0.00	0.24	0.34	0.15	3.65	1.12	2.49
13	-0.1	-2.9	0.00	-0.1	-3.0	0.00	0.29	0.32	0.13	3.50	2.27	1.32
14	0.0	-1.7	0.00	0.0	-1.6	0.00	0.00	4.44	0.00	0.25	0.17	0.09
15	0.1	-2.9	0.00	0.1	-3.0	0.00	0.30	0.32	0.13	5.67	2.27	1.32
16	0.1	-2.8	0.00	0.1	-2.8	0.00	0.25	0.34	0.15	5.60	1.12	2.49
17	0.2	-0.7	0.00	0.2	-0.7	0.00	0.17	0.16	0.30	4.87	0.37	1.02
18	-0.1	-0.9	0.00	-0.1	-0.9	0.00	0.43	0.16	0.24	5.44	0.34	1.11
19	0.0	-3.5	0.00	0.0	-3.5	0.00	3.12	0.31	0.17	25.03	1.01	2.84
20	0.0	-3.4	0.00	0.0	-3.5	0.00	0.59	0.31	0.09	5.80	2.24	1.37
21	0.0	-1.9	0.00	0.0	-2.0	0.00	0.25	0.16	0.51	0.00	4.44	0.00
22	0.0	-3.4	0.00	0.0	-3.5	0.00	0.62	0.31	0.09	9.44	2.24	1.37
23	0.0	-3.5	0.00	0.0	-3.5	0.00	3.65	0.31	0.17	44.21	1.01	2.84
24	0.1	-0.9	0.00	0.1	-0.9	0.00	0.44	0.16	0.24	6.77	0.34	1.11

Table 3.4. COMB2: NP-Model and SAP2000 errors on nodal displacements and rotations.

	Displ. SAP			Displ. NPM			SAP Rel. Errors			NPM Rel. Errors		
Node	u	v	r	u	v	r	u_{err}	v_{err}	r_{err}	u_{err}	v_{err}	r_{err}
-	[mm]	[mm]	[rad]	[mm]	[mm]	[rad]	[%]	[%]	[%]	[%]	[%]	[%]
1	0.0	0.0	0.00	0.0	0.0	0.00	-	-	-	-	-	-
2	35.5	0.2	-0.01	35.5	0.2	-0.01	0.26	0.15	0.22	0.26	0.52	0.27
3	35.9	-9.0	0.00	35.9	-9.0	0.00	0.26	0.23	0.92	0.23	0.01	7.75
4	35.9	-1.1	0.00	35.9	-1.1	0.00	0.26	0.77	0.03	0.23	6.39	0.85
5	35.8	-1.0	-0.01	35.8	-1.0	-0.01	0.26	0.17	0.23	0.27	4.61	0.35
6	0.0	0.0	0.00	0.0	0.0	0.00	-	-	-	-	-	-
7	35.9	-3.6	0.00	35.9	-3.6	0.00	0.26	0.25	0.12	0.25	0.74	1.01
8	35.8	4.0	0.00	35.9	4.0	0.00	0.26	0.05	0.17	0.25	1.22	0.90
9	35.5	-1.1	-0.01	35.5	-1.1	-0.01	0.26	0.15	0.21	0.30	0.33	0.23
10	0.0	0.0	0.00	0.0	0.0	0.00	-	-	-	-	-	-
11	78.4	0.3	-0.01	78.4	0.3	-0.01	0.26	0.16	0.25	0.27	0.95	0.34
12	78.6	-7.1	0.00	78.6	-7.1	0.00	0.26	0.27	1.04	0.26	0.15	10.90
13	78.4	-1.1	0.00	78.4	-1.0	0.00	0.26	0.90	0.04	0.26	8.10	1.16
14	78.2	-1.7	0.00	78.3	-1.6	0.00	0.26	0.17	0.23	0.28	4.65	0.32
15	78.3	-4.5	0.00	78.3	-4.6	0.00	0.25	0.23	0.12	0.27	1.15	0.80
16	78.3	1.8	0.00	78.3	1.7	0.00	0.25	0.01	0.14	0.27	3.02	0.40
17	78.0	-1.7	-0.01	78.1	-1.7	-0.01	0.25	0.16	0.24	0.29	0.28	0.21
18	105.8	0.2	0.00	105.8	0.2	0.00	0.28	0.18	0.27	0.26	01.30	0.53
19	105.8	-5.1	0.00	105.8	-5.1	0.00	0.28	0.44	0.64	0.26	0.34	8.62
20	105.5	-2.5	0.00	105.5	-2.6	0.00	0.26	0.47	0.01	0.28	3.19	1.35
21	105.3	-1.9	0.00	105.3	-2.0	0.00	0.26	0.17	0.24	0.28	4.65	0.35
22	105.3	-3.9	0.00	105.3	-3.9	0.00	0.26	0.27	0.17	0.28	1.90	0.73
23	105.1	-1.3	0.00	105.2	-1.3	0.00	0.26	0.41	0.08	0.28	3.74	0.97
24	105.0	-2.0	0.00	105.0	-2.0	0.00	0.26	0.16	0.28	0.29	0.33	0.04

Table 3.5. COMB3: NP-Model and SAP2000 errors on nodal displacements and rotations.

Stresses on the tapered portion

Finally, we focus our attention on the recovery of the stress distribution on the tapered portion of the beam. Among the available output, the software SAP2000 reports stress values at specific points over the beam cross-section for the different stress components. The comparison of stress solution among the NP-Model, Abaqus and SAP2000 aims again at highlight limits coming from an inaccurate beam modeling in case of non-prismatic members. As representative case we consider the left-side non-prismatic portion (see Figure 3.8 (b)) of the *RBeam* under the horizontal-vertical load combination because is the most interesting from the design point of view.

Figure 3.19 illustrates normal and shear stress distributions for the tapered beam portion at half length of the beam ($L = 1$ m). For the normal stress there is consistency in results between the three models. The shear stress recovered for the NP-Model agrees very well with Abaqus, while SAP2000 diverges from Abaqus solution. As shown in Figure 3.19, the stress values indicated in SAP2000 perfectly trace the conventional Jouransky parabolic distribution valid for prismatic cross-sections. On the contrary, the shear distribution obtained with the NP-Model and Abaqus presents a different shape, with a maximum value greater than the one predicted by SAP2000 and corresponding to the bottom fiber of the section, not to the midpoint. It is worth to notice that, as already discussed in 2.1.1, this non obvious result is a consequence of the non-trivial dependence in the stress distribution linked to the non-prismatic beam behavior.

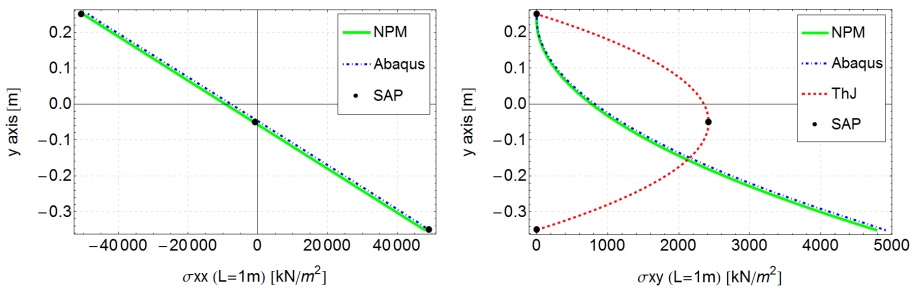

(a) **(b)**

Figure 3.19. COMB3: σ_{xx} stress distribution at half length of the beam (a); σ_{xy} stress distribution at half length of the beam (b).

3.4 Conclusive considerations

A comprehensive 2D model for the study of non-prismatic beams and particularly for the evaluation of the stiffness matrix of such special members is analyzed. The work presented in Chapter 2 and Chapter 3 shows firstly the flexibility of the proposed NP-Model in the choice of the starting hypotheses and then its reliability when used in real design applications.

Chapter 2 illustrates how the NP-Model allows to consider different stress and displacement distributions only changing the hypotheses on these field, leading automatically to the final system of ODEs. To evaluate how the accuracy of the hypotheses reflects on the problem solution, the models correspondent to the three set of hypotheses presented in Section 2.2.2 are compared. The comparison is made on five different non-prismatic beam geometries. Furthermore, results coming from FE Abaqus simulations are taken as reference solution for the calculus of errors. Final results show a good response of the NP-Model for the symmetric tapered beam case, independently from the chosen set of hypotheses. On the other hand, moving towards more complex geometries (as example to a non-symmetric case) the simpler hypotheses (Hp1) are insufficient for a correct evaluation of stress and displacements, especially underlying how significant is the contribute of the σ_{yy} stress variable. Between the more accurate hypotheses Hp2 and Hp3, the first one seem to be the more suitable in terms of errors and computational cost. The use of Hp3 does not lead to a significant improvement and corresponds to less understandable equations than those related to Hp2. Thus, for the cases studied in Chapter 3, the Hp2 is considered reasonably efficient for the purpose of work.

To show the capability of the model in a real application case, Chapter 3 focuses on a study of a 2D RC frame with haunched beams. The problem is analyzed considering results from the model under investigation, the commercial software SAP2000 and the FE software Abaqus, considered as the reference solution. This is made to evaluate how the accuracy of the modeling approach is of crucial importance, especially when non-trivial problems have to be handled. Particularly, in our case, the variability of the cross-section leads to some modifications in governing equations which are neglected in the SAP2000 modeling. The error of approximation made by SAP2000 is already evident at the *element-scale*, comparing the stiffness matrices related to the asymmetric tapered portion (Section 3.2.2). The wrong terms that appears in the SAP2000 matrix are consistent with the formulation included in the software for non-prismatic beams, when 1D frame elements are chosen for the modeling. Concerning to the RC frame problem studied in Section 3.3, several main conclusions can be drawn. SAP2000 present a different response and greater errors, especially in terms of element forces and stresses, if compared to the NP-Model and Abaqus results when the load combinations including distributed vertical load are considered. This underlines the importance of being aware user of the commercial software to evaluate the correctness of the solution, particularly when non-conventional elements have to be modeled.

The case study of the RC frame shows how the NP-Model could represent a good theoretical method for the developing of a FE for non-prismatic beams. The simplicity of the NP-Model derivation, in fact, makes possible to implement and integrate such method in commercial software. Furthermore, the analyzed NP-Model can be the base of future studies such as for the development of a 3D non-prismatic beam code, non-homogeneous non-prismatic beams, and non-prismatic beams characterized by more complex constitutive laws.

4 AM in construction engineering

AM and 3D printing are innovative technologies with an impact on industrial production in many fields such as medical, civil and automotive. In the last few decades AM has changed not only the production paradigms, but also the distribution chain with new implications from a technological, social, and economic point of view. In architecture and civil engineering, it is expected that such approach will reduce costs and the production time leading to much freedom on design of shapes. Indeed, AM opens the possibility to overcome limits currently imposed by conventional manufacturing techniques as for the casting of RC members. This new technology is a promising step towards shape optimization and material saving, thus lightening the RC elements and reducing costs and environmental impacts.

The new approach presented in this Chapter has the goal of fabricating RC members exploiting the 3D printing technology. The proposed method is based on the subdivision of a RC member into concrete segments separately printed and then assembled into a unique monolithic element along with the rebar reinforcement system. Following such innovative approach, the production of complex and optimized elements with variable cross-section will be possible against the common concrete casting process. In particular, the optimization of the shapes of the concrete segments enables a reduction in the concrete volume used to fabricate RC members, while still guaranteeing good mechanical performances of the final elements.

Summarizing the content of Chapter 4, Section 4.1 gives an overview on the "state of art" of the AM impact in the construction field, with a particular focus on applications with the concrete material. Then, Section 4.2 reports a detailed description of the proposed 3D printing approach for the production of RC members, i.e., the definition of the design concept for the concrete segments, the 3D printing equipment and the study of the optimized material. Finally, Section 4.2.5 introduces geometric features and configuration of the 3D printed tests that will be treated in Chapters 5 and 6.

4.1 Background and literature review

AM has been defined as "the process of joining materials to make objects from 3D model data, usually layer upon layer, as opposed to subtractive manufacturing methodologies, such as traditional machining" [ASTM, 2012]. AM technologies are increasingly having an impact on industrial processes in many fields and numerous applications have been developed so far, ranging from, for example, automotive

to medical, security and aerospace sectors [Berman, 2012, Lipson and Kurman, 2013, Rengier et al., 2010]. Advocates of AM argue that this technology represents a new industrial revolution and is enabling the mass customization of industrial production, where small quantities of customized products can be built affordably [Campbell et al., 2011, Berman, 2012, Petrick and Simpson, 2013].

Until a few years ago, AM technologies were mostly applied to rapid prototyping (RP), i.e., the fabrication of prototypes used for iterative design, inspection and communication tools. In fact, AM technologies were not considered to be able to process common materials with adequate mechanical and physical properties [Kruth et al., 2007]. However, the emerging digital fabrication, defined as the application of digital modeling and technologies to the production of custom material objects, promises to revolutionize the traditional manufacturing schemes. This new technology represents also an opportunity towards forms optimization and material saving, thus reducing costs and environmental impacts [Agustí-Juan et al., 2017]. Nowadays AM technologies are successfully implemented to fabricate objects made of ceramic [Scheithauer et al., 2015], metals [Ladd et al., 2013], and polymers [Inzana et al., 2014] with adequate mechanical properties. AM technologies are attracting a growing interest in construction industry as well, especially in the concrete technology. Construction is already an "additive" process (excluding prefabrication), in fact whether it is brick laying or casting of concrete, building forms are generated layer upon layer from below upwards. It is thought that the idea of using AM in large scale manufacturing is born only in the latter years, while actually in the mid-90s, Joseph Pegna [Pegna, 1997, Pegna et al., 1999] already saw the possibility of designing entire buildings extruding subsequent layers of concrete and sand. The interest in exploiting AM technologies in this sector is mainly the result of the expectation of new freedom in terms of the design of shapes, elements and structures, enabling new aesthetic and functional features (often referred to as free-form constructions). Indeed, in the construction industry, single components are in most cases unique in dimension. Therefore, standardized/traditional manufacturing processes require pieces to be cut through subtractive technologies (in which the material is machined away to produce the final object - e.g. natural stone, ceramic pavements) or proper molds to be created. In the latter case, molds are utilized in combination with formative technologies (where the fresh material is cast in a mold - e.g. reinforced concrete elements) to achieve the final shape of the object [Buswell et al., 2007]. It is evident that the automation in such processes could lead to a better organization, a reduced manpower and time of construction.

From a practical point of view, AM technologies are still a novelty in this field since the inherent properties of this material, such as the great flexibility in terms of handling and placement, are not yet explored in the word of digital fabrication [Wangler et al., 2016]. Nevertheless, different products and applications that adopt the AM approach have been already developed and tested to print concrete objects/elements (e.g. contour crafting [Khoshnevis, 2004], concrete printing [Lim et al.,

2012], D-shape [Tibaut et al., 2016], slip-forming (smart dynamic casting [Lloret et al., 2015]). The detailed review of the methods of digital fabrication with concrete (often referred to as "digital concrete"), including the above-mentioned cases of concrete printing, is reported in Wangler et al. [2016]. To date, most developments in digital fabrication of concrete-like products have been focused on layered extrusion technology (such as contour crafting, concrete printing), probably because its overall operating procedure is based on the more widespread production scheme of polymeric customized parts. However, its application in construction processes requires much larger printers (or, more in general, robotic machines) than those used for metal or plastic objects, due to the dimensions of the final objects to be printed. The automated machinery used for layered extrusion of concrete generally includes a digitally controlled moving printing head (or nozzle) which precisely lays down the concrete or mortar material layer-by-layer, enabling the opportunity to create customized structures and/or functional voids into the printed elements [Perkins and Skitmore, 2015, Le et al., 2012]. The engineering challenges related to layered extrusion technology are multiple. Indeed, to effectively exploit the functional/mechanical properties of 3D printed concrete products, the layered extrusion of concrete elements requires the fresh printed material to have some specific rheological properties [Valkenaers et al., 2014]:

- Workability: the capacity to be worked and moved to the printing head through a pumping system throughout a given time interval.
- Extrudability: the capability to be properly extruded through the printing head with a continuous material flow.
- Buildability: the capacity to both remain stacked in layers after the extrusion and sustain the weight of the subsequent layers that are deposited by the printing process.

Therefore, the concrete/mortar rheology must be optimized to achieve a balance between the need for workability and extrudability on the one hand - which would require reduced viscosity - and the need for buildability on the other - which would require an increased viscosity. The printing speed is a critical parameter as well, and can have an impact on the mechanical properties of the printed elements. Printing speed must be set based on the rheology of the printed mortar, the dimensions of the objects and the dimensions of the extrusion head. In fact, the time elapsed between the deposition of two layers must be long enough to let the first layer adequately harden and become capable of sustaining the weight of the second layer, but short enough to guarantee that the first layer is still sufficiently fresh to develop a good bond with the second layer [Wangler et al., 2016, Perrot et al., 2016]. Given all the issues and challenges related to the AM of concrete elements, this technology is still not mature to be used in the market. In addition, steel reinforcement integration in 3D printed concrete structures is characterized

by a slow technological progress. Indeed, available examples concern the mesh mold approach which consists in digitally fabricate metal wires formworks that act as reinforcement during the concreting process [Wangler et al., 2016] or, alternatively, the use of fibers in printable mortars. An effective approach for steel reinforced concrete elements is not yet a developed concept, mainly due to the scarce versatility of "classical" reinforcing steel (in the form of rebar) with regard to AM technologies. Nevertheless, researchers in this field are increasingly interested in the opportunities that AM is able to provide in the future also for steel reinforcement integration. This work aims to contribute to this promising line of research, reporting the outcomes of the developed novel approach for the design and fabrication of RC beam elements, based on AM technology.

4.2 Novel approach for 3D Printed RC elements

The project of 3D printing RC members comes from the collaboration between University of Pavia and University "Federico II" of Naples, with the support of the STRESS consortium [STRESS, 2015]. The main goal of this project is to exploit the potential of AM technology and researchers' knowledge on concrete mortar manufacturing and design to produce optimized RC elements. 3D printing technology, indeed, opens the possibility of realizing shapes that are impossible to obtain with usual methods.

4.2.1 Approach to element design

The objective of the approach herein presented consists in manufacturing steel rebar RC beams using AM technology of concrete. The implementation of the proposed approach enables the to built structural elements with complex shapes. In particular, the fabrication process allows the final beam to be curved - in the plane containing the longitudinal axis - with variable cross-section heights $h(x)$ (Figure 4.1). A further fundamental characteristic is that AM allows the beam to be partially hollow (once it has been properly designed) in order to save material, provide functional uses and reduce the final weight, maintaining adequate mechanical properties related to the structural application. A beam configuration characterized by a curved profile and holes would require the arrangement of complex (and costly) formwork systems when using classical concrete casting technology (i.e. polystyrene molds, multiple wooden formworks etc.).

The presented method is based on the idea that the concrete beam can be cut into several "segments" (see Figure 4.2 (a)) that are 3D printed separately and then assembled together to create the final curved shape. Each beam segment is printed through the thickness of the beam, i.e., the orthogonal direction to the plane of the beam (z direction in Figure 4.1 (a)). This allows to print only elements with equal cross-section through the height, with no need to shift the concrete flow layer-by-

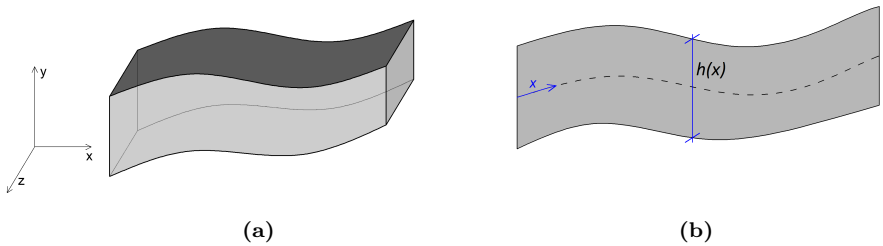

Figure 4.1. 3D view (a) and planar section (b) of the target beam with a curved longitudinal axis x and a variable cross-section height h(x).

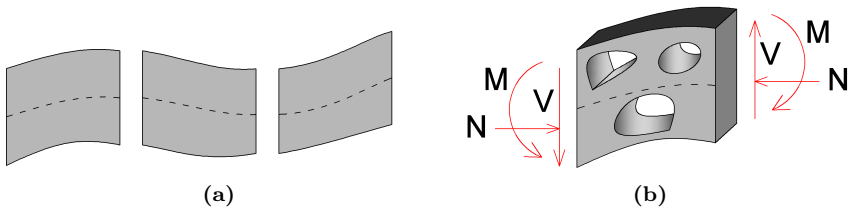

Figure 4.2. Possible configuration of the cut segments for the target beam (a); topologically optimized segment with several voids to save material and guarantee adequate mechanical performances related to the internal forces (b).

layer during the printing process to fabricate curved shapes. This choice is linked to the low shear strength of the fresh concrete, which is a major constraint when curved shapes are printed by shifting the layers through the height of the element. In this case, only smooth curved shapes can be fabricated (e.g., see Rudenko [2017]) as a result of the difficult optimization of the printing speed, the flow viscosity, the extrusion force, the layer thickness and other material parameters. Once the number of segments is defined (mainly depending on the printer capabilities) each beam segment is designed to accomplish proper mechanical requirements related to the internal forces acting on the beam (shear, axial forces and bending moment). To this end, concrete segments can be topologically optimized with a number of voids, to save material while still guaranteeing the required mechanical performances (see Figure 4.2 (b)). Currently, this step of the design process is an ongoing activity since the optimization strategies reported in literature and implemented in software cannot directly be applied to the proposed 3D printing approach. For these reasons, preliminary attempts towards a defined and customized optimization strategy are proposed in Chapter 5 together with a detailed framework of the problem and its

peculiarities.

In a second stage, only after the segments are assembled together, the steel rebar reinforcement is installed externally to the beam by anchoring the steel elements in specific holes made in the segments during the printing process (Figure 4.3 (a)). To do this, each steel rebar can be bent at both ends to ensure there are two

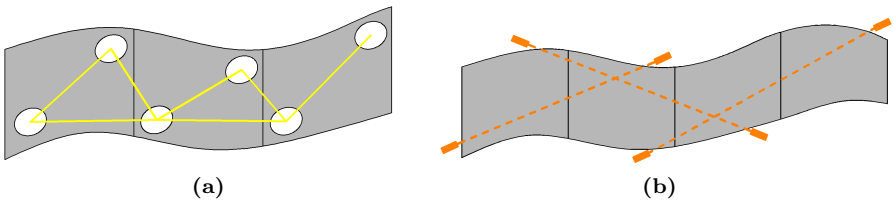

Figure 4.3. Rebar reinforcement scheme (a); post-tensioned cable scheme (b).

proper anchoring dowels for insertion into the holes. These are then fixed, for examples, with a mortar or structural adhesives. An alternative method consists in an in-plane (X-Y) rebar system and an out-of-plane system of threaded rods (Z direction), as specifically described in Section 4.2.4. As a result, the steel rebar is designed also to fix the segments together and lock them into a single monolithic element. In the case of long beams, post-tensioned cables can be installed through the concrete segments (for example, into cavities drilled once the beam has been assembled) to fix them together and apply axial forces that increase the flexural strength/stiffness of the beam (Figure 4.3 (b)). This technique is similar to that adopted for the segmented concrete bridges in which external pre-stressing and dry joints are used to form continuous concrete beams [Xanthakos, 1994].

4.2.2 3D Printing process and equipment

The first tests related to the presented approach have been conducted using the BigDelta WASP printer from the Italian CSP company [WASP, 2015]. The printing area of this machine is a triangle, with each side being about 4.0 m. The printing head is sustained by three braces whose ends are moved along three vertical pillars (Figure 4.4). By controlling the movement of the braces, the printing head is moved horizontally and vertically and can reach a maximum height of 1.5 m. The printing head is composed of a conical container with a capacity of about 20 liters of fresh concrete. The concrete is extruded by a rotating endless screw through a hole with a variable diameter. In our case, a 25 mm diameter is used. A control unit guides the movement of the printing head by processing an STL file which includes the layer by layer printing paths. Figure 4.5 depicts a phase of the printing process of a concrete object. The input to the printer is the path that the printing head has to follow during the manufacturing process and includes the planar path for each

layer, the height of the layers, and the speed of the printing head.

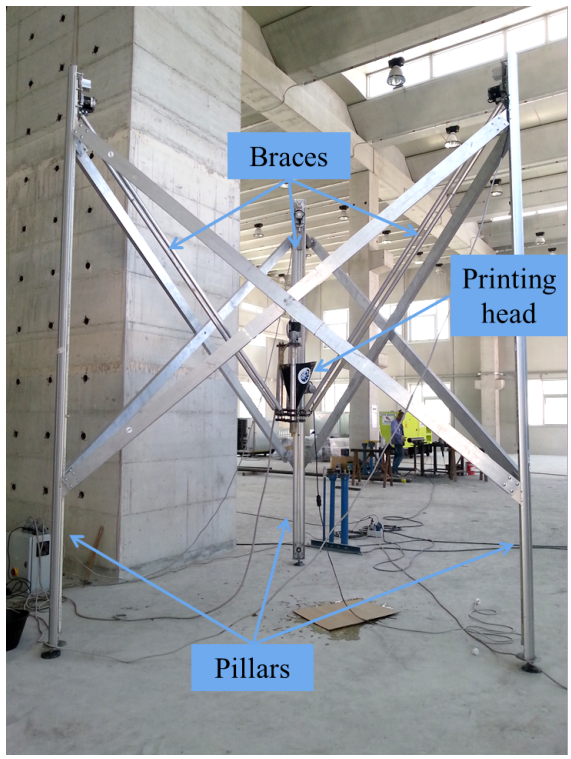

Figure 4.4. The WASP printing machine.

The final printed element is composed of walls that are built layer by layer during the printing process. A number of parameters, including the flow viscosity, the extrusion force, the extrusion head diameter, the layer thickness and the printing speed control the final thickness of these walls. Indeed, the thickness of the walls increases with the increase of the extrusion force and the diameter of the extrusion head, and it is reduced with the increase of the flow viscosity and the printing speed. The thickness of the walls can also be increased with multiple adjacent path lines, enabling a final thickness that is roughly a multiple of the thickness of a single path line. An optimal balance among these parameters is also important to guarantee that the extruded material can remain stacked and bonded in layers and sustain the weight of the other layers which are deposited above during the printing process.

Figure 4.5. A phase of the 3D printing process.

4.2.3 The concrete material

The concrete material used in the printing process is designed to overcome a number of constraints related to its mechanical and physical properties:

- An optimal viscosity of the fresh mortar is needed, to make it both extrudable, i.e., capable of being ejected through the extrusion head, and buildable, i.e., capable of being stacked in layers;
- High strength is required, to compensate for the potential weakness of the connection points between the contiguous layers;
- The maximum aggregate size has to be compatible with the extrusion head diameter.

Given these limitations, a cement-based mortar is fine-tuned with a 0.39 water/cement ratio and a maximum diameter of the aggregates of 4 mm. To increase the viscosity, 0,5% in weight of polypropylene short fibres is also added. The mix is adjusted with viscosity modifying admixtures and superlasticizer. The slump class of the concrete is evaluated according to the EN 12350-2:2009 procedure [EN-12350, 2009] and is equal to S1. The average cubic strength R_{cm} of the concrete after 28 days of curing is determined over four specimens and is equal to 53.5 MPa [EN-12390, 2009]. The average cylindrical strength f_{cm} is estimated as 83% of the cubic strength, i.e., 44.4 MPa.

In order to assess whether the printing process affects the material strength in the 3D printed elements, a set of hollow cylinders are designed to be printed and tested along the axial direction. The cross-section of the cylinder is designed with one printing line, drawing a circumference with a diameter of 200 mm. The height

of the cylinder is equal to 200 mm and composed of 10 layers. Three cylinders have been printed with the process parameters previously described. The thickness of the cylinder walls is about 29 mm. The top and bottom surfaces are properly flattened and the specimens are tested in compression by means of a load controlled machine (Figure 4.6 (a)). The average cross-section area for each cylinder is computed by means of multiple measures of the external and the internal diameters along the height of the cylinders. The peak force is recorded and the peak stress is computed over the average cross-section area. The average compression strength f_{cpm} of the printed cylinders is derived as the average of the peak stress values and is equal to 37.2 MPa. These details are also reported in Table 4.1. The obtained value for f_{cpm} is lower than the cylindrical bulk strength of the material, with a reduction equal to 16% of f_{cm}. This gap can be justified by the weakness surfaces between two contiguous layers. In fact, two phenomena can lead to a reduced strength: an imperfect bond between the layers that can initiate the failure of the specimen, and a reduced thickness of the wall, that can lead to a stress concentration and may trigger the failure of the specimen (Figure 4.6 (b)). These circumstances suggest that a careful evaluation of the 3D printed material properties should be considered when designing 3D printed objects with structural features.

Specimen	$D_{ext,avg}$ [mm]	$D_{int,avg}$ [mm]	A_{avg} [mm^2]	F_{max} [kN]	f_{cp} [MPa]	f_{cpm} [MPa]
C1	218	160	17039	594	34.9	37.2
C2	218	165	15763	545	34.6	37.2
C3	218	173	13776	579	42	37.2

Table 4.1. Compression tests on the 3D printed cylinders.

4.2.4 Assembly and connection system of the 3D printed segments

The rebar scheme consists on an in-plane (X-Y) system and an out-of-plane system of threaded rods (Z direction) as illustrated in Figure 4.7 (a). The orthogonal steel rods (Z direction) are positioned into the holes of each modulus and secured with a high strength flowable cement-based mortar. The threaded rods of the in-plane system are linked to the out-of-plane system through male thread connectors and hex nut rod pipes (Figure 4.7 (b)). Table 4.2 (a) reports technical specification of the connection system constituents. This particular connection system makes possible the assembly and disassembly of the beam thus opening the horizon to the concepts of reusable modulus or design for deconstruction. The small grooves between the segments on the top side of the beam are sealed with a low viscosity cementitious mortar to secure the contact between the segments in correspondence

(a) (b)

Figure 4.6. Printed specimen during the uniaxial compression test (a); thickness reduction of the printed walls between two contiguous layers (b).

Male thread connector	M12 x 75 mm UNI 6058, DIN 444
Hex nut rod pipe	M16 x 60 mm UNI 6058, DIN 444

Table 4.2. Technical specification of the connection system constituents.

with the longitudinal top concrete chord. The beam segments and the rebar system are designed to provide a final monolithic configuration with the following features:

- A top continuous concrete chord to bear the compression forces induced by the flexural behavior;
- A bottom steel chord to balance the top compression stresses and bear the tensile forces;
- Diagonal compression concrete struts and opposite diagonal steel struts in the lateral segments to bear the shear forces.

4.2.5 Introduction to the studied 3D printed test cases

In the following, the 3D printed beams adopted as test cases for the numerical and experimental analysis reported in Chapter 6 are presented. The same geometries

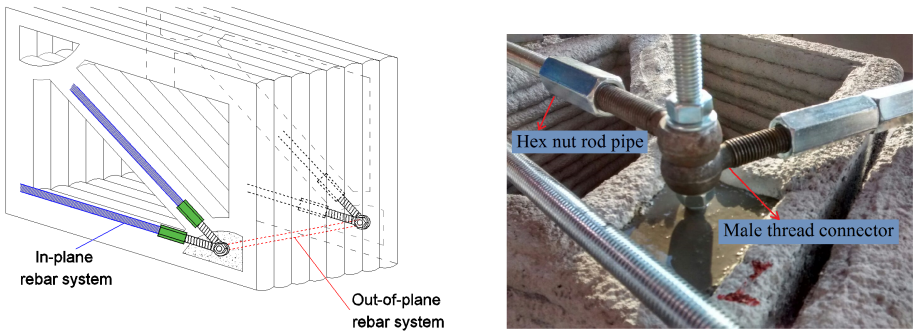

Figure 4.7. Representation of the in-plane and out-of-plane rebar systems (a); details of the connection system (b).

will be considered as starting configurations for the topology optimization problems analyzed in Chapter 5.

Test 1: curved shape 3D printed RC beam

As first test a curved 3D printed beam has been produced and consists in an irregular arc (longitudinal profile of the Vesuvius volcano) of about 4.00 m long with a width equal to 0.25 m. The whole shape is characterized by a double path line of printed concrete with the exception of the bar hole edges (Figure 4.8). For the reinforcement of the beam we adopt bars characterized by a diameter of 16 mm and the connection system described in Section 4.2.4.

Such an irregular shape has been chosen to exploit the potentialities of AM opportunities, consisting in 3D printing of free-form concrete elements with respect to traditional manufacturing techniques. In fact, as it can be noticed from Figure 4.8, in this case each 3D printed concrete segment is different from the others without the constraint of producing pieces with the same shape. The final configuration of the printed beam is depicted in Figure 4.9. In this preliminary phase of the work, we have optimized the shape of each beam segment according to a numerical estimation of the internal stress distribution for a similar arch-shaped solid concrete beam. This allows the "ideal" removal of concrete material from the solid beam configuration, still guaranteeing proper segment strength and stiffness properties.

Test 2: straight 3D printed RC beam

As second test we have fabricated a straight 3D printed beam with a constant height. The target concrete beam is 3.0 m long and characterized by a rectangular cross section with 0.20 m and 0.45 m of width and height, respectively. The straight

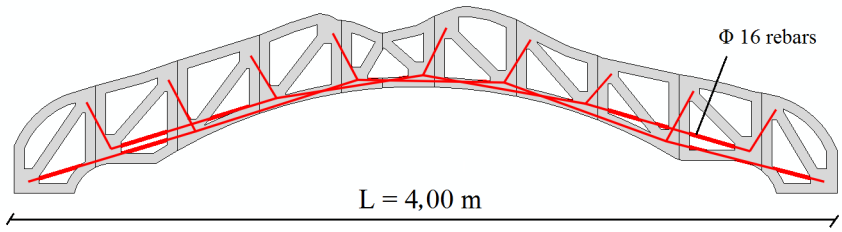

Figure 4.8. Geometric configuration of the curved shaped printed beam.

Figure 4.9. 3D printed RC beam with a variable curved cross section.

beam is studied through numerical analysis and is the specimen of the full-scale experimental test. This choice is motivated by the opportunity to easily compare these preliminary results with classical beam theory, while the general approach is applicable to more general cases. Furthermore, it allows to avoid possible critical issues arising from complex shapes, as example, the experimental setting and arrangement.

The 3 m long beam is cut into five segments of two typologies, namely A and B in Figure 4.10 (a). In detail, with respect to the left side of Figure 4.10 (a), the segment type A is designed to be installed in its overturned position on the right side of the beam. While the type B, placed at the mid-span, connects the two sides. According to the procedure, each segment can go through a topological optimization to save as much material as possible and guarantee satisfactory mechanical performances against the internal forces acting on the segment. Furthermore, a number of holes need to be designed to anchor the rebar or, alternatively, install the external steel reinforcing system. By assuming that a distributed constant load (gravity load) and a concentrated load at the mid-span act on the beam, each segment should resist variable bending moments and shear forces. The strut and tie model [Schlaich et al., 1987, Schlaich and Anagnostou, 1990] is a rational approach to represent a complex structural member with an appropriate simplified truss system considering all the acting forces simultaneously. For the experimental purposes, since we want simply to study the flexural behavior of the straight beam, we decided to adopt such a well-known approach as optimization strategy to design

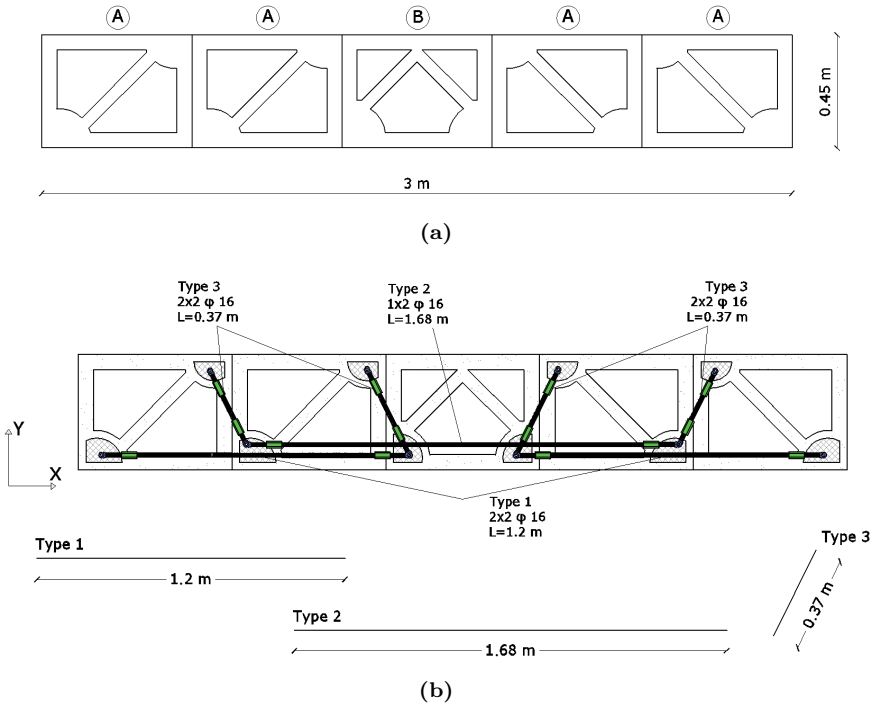

Figure 4.10. Schematic representation and dimensions of the beam segments A and B (a) and the correspondent printed segments (b).

segments A and B. Thus, the geometric configuration and dimensions for the two segment types illustrated in Figure 4.11 (a) will be assumed for the experimental test of Chapter 6. However, more accurate optimization methods should be used and topology optimization represents a fundamental step forward to develop a reliable framework in the printing of RC beams. The printed segments A and B are shown in Figure 4.11 (b). Each segment is composed of 10 layers with a total height of 20 cm. The diameter of the nozzle is 2.5 cm and the average thickness of the walls is roughly equal to 6 cm since correspondent to a double thickness-printing path. The beam segments are designed along with the rebar system to guarantee the tensile reinforcement (at the bottom side of the beam) and to lock the segments in a single monolithic element. The total weight of the beam is 36 kN, which is about 12 kN/m of distributed weight. This equates to about 54% of the weight of an equivalent solid beam, i. e., with the same cross-section.

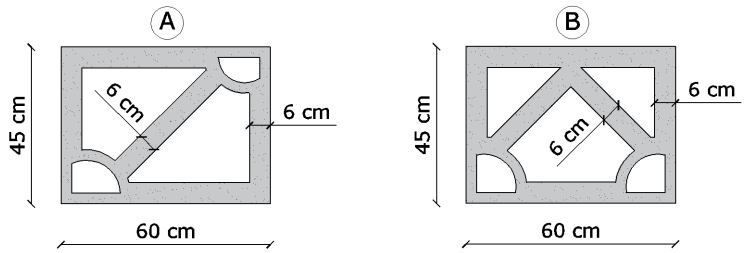

(a)

(b)

Figure 4.11. Schematic representation and dimensions of the beam segments A and B (a) and the correspondent printed segments (b).

5 3D printing of RC elements: topology optimization

In the present Chapter we want to summarize some preliminary studies on topology optimization oriented to the novel approach for the 3D printing of RC elements. Trough the research on optimization methods, it is possible to obtain innovative shapes of components providing the desired performance in terms of static stiffness and aesthetic benefits, but with the least possible weight and with respect to predetermined constraints. Nevertheless, the application of classical optimization strategies for AM purposes is not straightforward. Firstly, the choice of the optimization method should be based both on the final scope of the printed object and on the parameters of interest. As example, among designers, optimization methods able to solve stress-constrained problems are more significant than those focused on compliance minimization problems. Furthermore, some inherent issues of the optimization technique may be magnified resulting in an unfeasible product and additional analysis steps within the design process. Secondly, there are both technological constraints which can still limit the physical realization of the optimal topology and limitations connected to the printing material. Regarding this point, as example, standard optimization methods based on Von Mises stress have limited usefulness when applied to the design of concrete objects.

From this considerations starts the idea of deepening the research on new optimization strategies aligned with the proposed 3D printing project. In particular, the period of research spent at the Technische Universität München (TUM) is part of the aforementioned project. Aim of the collaboration with Professor K. U. Bletzinger, head of the Statik Chair, and his group is to combine UniPV experience on AM with the expertise on structural and shape optimization of the hosting lab. To investigate different 3D printing problems we exploit the capabilities of the application developed in the open-source Kratos [CIMNE, 2017] code for the optimization of 3D solid structures. In parallel, remaining focused on topology optimization methods for AM, a stress-constrained Matlab optimization code tuned for concrete applications has been developed. This work has also involved the collaboration of Paola Festa and Tommaso Pastore from the Department of Mathematics of University "Federico II" of Naples. The proposed algorithm, from now on identified with the name PSTOpt, is a non-gradient based method, easy to implement, and characterized by a constraint based on principal stresses rather than standard Von Mises stresses (normally more suitable for metal materials).

Resuming the contents of Chapter 5, Section 5.1 reports a brief review on topology optimization methods applied to AM and concrete modeling. In Section 5.2, details about the starting optimization problem derived from the 3D printing approach are provided. The PSTOpt algorithm structure and principal features are presented in Section 5.3 together with some preliminary tests and results from a real case study of a concrete beam. Then, Section 5.4 illustrates the outcomes of the work conducted during the period abroad on the evaluation of the software Kratos for topology optimization analysis of 3D-printed objects. Finally, in Section 5.5 final remarks are reported, advantages and disadvantages of the analyzed optimization tools are also discussed.

5.1 Literature review

Topology optimization is the most general form of structural optimization. In continuum case it aims at determining efficient solutions starting from very few prescribed specifications such as load case, boundary conditions and admissible design spaces [Rozvany, 2014]. This method has been used for years in the industry to create innovative, low-weight, and structurally efficient designs. The development of AM and 3D printing technologies makes possible to produce extremely complex structures which until recently, using traditional production methods, would have been impossible to accomplish or would require unreliable efforts and unacceptable costs. To maximize the potential of 3D printing, it is really important to optimize component design using topology optimization from the earliest stages of its conceptual development.

During the last decades, the interest on topology optimization applied to AM is increased in the scientific community and several research groups start to work on the matter. Without the ambition of providing a complete literature review, here in the following some contributions on the topic are reported. Chahine et al. [2010] present a research focused on the well-known voxel-based topology and a truss-based topology methodologies invested in the AM field. Gaynor [2015] and Aremu et al. [2010] develop and test new topology optimization algorithms for AM purposes. Sundararajan [2010] and Chu et al. [2008] propose new tools for AM of customized meso-structures and cellular materials, trying to exploit the flexibility of AM towards new materials and innovative combination of them. Regarding this point, a design and fabrication process for the realization of three-phase, multiple-material compliant mechanism is proposed in [Gaynor et al., 2013a]. A literature survey on current design optimization approaches and on the impact of AM in the manufacturing field is presented by Doubrovski et al. [2011]. In the works of Zegard and Paulino [2016] and Brackett et al. [2011] a constructive overview on issues and opportunities on bridging optimization tools to the 3D printing technology is given.

This encouraging and dynamic trend leads researchers to study the coupling of structural optimization and additive technologies in a wide variety of applica-

tion fields. However, focusing on civil engineering and particularly on 3D printing technology available for the concrete material, such coupling is still difficult to be reached. Indeed, even if there is the will of exploring new optimization tools and their integration within the large-scale AM process for concrete [Gosselin et al., 2016], the contributions on the matter are still few. This is probably due to the fact that printing concrete and cement-based materials present more difficulties and technological constraints if compared, as example, to plastic materials. The study on topology optimization methods applied to concrete structures, instead, has received considerable attention in recent years. Liang et al. [2000], Bruggi [2009] and Liang et al. [2001] investigate on the so-called strut-and-tie models for RC members obtained from topology optimization. The content of these references is particularly interesting since practical examples and real material parameters are examined. Other significant contributions are related to the parallel optimization of concrete and steel to obtain an optimal conceptual design [Bogomolny and Amir, 2012]. On this topic, a conventional approach is to represent the concrete by a gradient-enhanced continuum model while the reinforcement is modeled as elastic bars that are embedded into a truss ground structure [Amir, 2013, Amir and Sigmund, 2013, Sved and Ginos, 1968, Gaynor et al., 2013b]. In spite of the great effort in this research route, unfortunately, most of the cited methods do not tackle stress-constrained optimization problems and often make use of the Von Mises stress which is suitable for metal materials rather than cementitous ones. Furthermore, there is still a lack in the linking topology optimization strategies to AM and 3D printing of concrete.

It is from this background which comes the idea of deepening the research on topology optimization methods customized for the 3D printing approach proposed for the manufacturing of RC members. To delineate constraints to be overcame and individuate possible optimization strategies, in the following, the starting optimization problem is described in detail. Then, motivations which has led to the development of the Matlab algorithm and the study of the Kratos topology application are provided.

5.2 Starting problem

The idea behind the project of 3D printing RC is to exploit the potential of 3D printing technology and researchers' knowledge on concrete manufacturing and design to produce optimized RC elements. Recalling the overall strategy (see Figure 5.1) it starts with the cutting of the structural element (as example a beam) into "segments" separately printed. Each beam segment is printed through the thickness of the beam, i.e., in the direction orthogonal to the plane of the beam (z direction in Figure 5.1). This allows to print only elements with equal cross-section through the height, with no need to shift the concrete flow layer-by-layer during the printing process to fabricate curved shapes. According to the procedure,

each concrete segments can be topologically optimized with a number of voids, to save material while still guaranteeing the required mechanical performances. Finally, the optimized pieces are placed side by side and assembled to create complex shapes. When the assembly is completed, a steel rebar reinforcement is externally

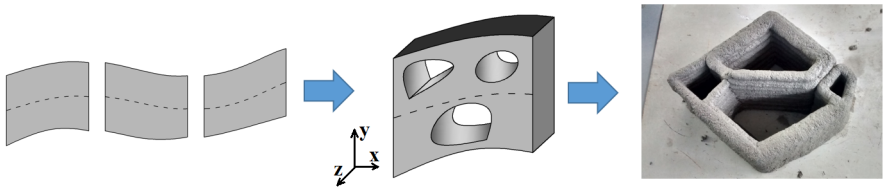

Figure 5.1. Overall strategy for the 3D printing of RC members: from the cutting of the initial object to the topology optimization of the concrete modulus to be printed.

installed and also mortar materials are employed to assure the continuity and the monolithic behavior of the segments. The typical assembly view of a 3D printed beam is shown in Figure 5.2.

Looking at the design and production process, the topology optimization of the concrete element is a key step within this chain. In fact, topology optimization is a powerful tool for determining the best distribution of material within a defined design domain, perfectly aligned with the new opportunities offered by the AM technology. However, although the manufacturing constraints for AM are much less significant than traditional manufacturing routes there are still limitations that require consideration [Brackett et al., 2011]. In particular, focusing on the proposed 3D printing method, there are some important aspects which should be pointed out connected to the implementation of a topology optimization strategy for AM purposes:

- *Topology optimization problem*: within the framework of AM applied to the construction of RC elements, the study of minimum weight stress-constrained problems is the most representative for practical structural issues. Indeed, the primary goal for designers is to obtain the lightest structure having a straight control on the stress level.

- *Stages of the design process*: designers and engineers usually follow a process flow consisting in several steps before reaching the final product. The integration of a topology optimization tool leads to the achievement of better and performing solutions but at the same time to add further steps within the design process. The ideal pipeline from the starting CAD model to the solution that has to be manufactured should be developed in a single platform/environment. Otherwise, it should require the minimum number of commercial software or tools already available on the market.

- *Printing material*: the material adopted for the proposed manufacturing technique is the concrete. The particular constitutive behavior of the concrete material can not be properly characterized by conventional measures of stress like the Von Mises one, which are instead more suitable for steel and, in general, metal based materials.

- *Technology peculiarities*: the adopted 3D printing technology is extrusion-based, i.e., the concrete material is extruded through a printing head with a fixed diameter. Due to the particular features of this technology, the printing process present some physical constraints as the direction and the diameter of the extrusion allowed by the printer.

Figure 5.2. Typical assembly view of a 3D printed RC beam with a variable cross-section.

Considering all the aspects mentioned above, the formulation of a topology optimization strategy customized for the proposed approach is not trivial. Just reviewing the available literature, it is possible to notice that most of the optimization methods are limited to compliance minimization problems. This problem is considered classical in the optimization community and simpler to be solved if compared to the stress constrained one. Stress problems, indeed, bear more challenging difficulties such as high non-linearity [París et al., 2009, Le et al., 2010]. On the other hand, even if several researchers tackle the stress problem, in most of the cases the constraint defined is based on the classical Von Mises stress. Furthermore, more refined stress formulation lead to an higher complexity in terms of implementation and computational effort, as for the gradient-based methods [Patel et al., 2008]. Starting from these considerations, the aim of the work is to propose an efficient and simple algorithm which tries to overcome the *Topology optimization problem* and *Printing material* issues listed above. The developed algorithm, from

now on identified with the name PSTOpt, takes inspiration from the heuristic Proportional Topology Optimization (PTO) technique [Biyikli and To, 2015] and can solve both compliance minimization and stress-constrained problems. Focusing on stress-constrained problems, we introduce a constraint based on principal stress in order to better represent the real behavior of the concrete material. A first attempt towards the *Stages of the design process* issue is provided testing the Kratos software. The goal is to explore the capabilities of the TopOpt application developed in Kratos in the optimization analysis and post-processing of complex and realistic AM problems.

It is worth to notice that in this preliminary phase of the research we neglect the limitations connected to the proposed printing technology (*Technology peculiarities* issue), accepting optimized solutions which can not be directly printed. Furthermore, the parallel optimization of the concrete and steel systems is currently not considered. Nevertheless, improvements on the matter are essential for a full solution of the optimization problem and they will be tackled in future research steps.

5.3 PSTOpt Algorithm

In the following, a description of the studied optimization problem and of the stress-constrained PSTOpt algorithm is provided. A particular focus is dedicated to the constraint based on the principal stress evaluation and on the construction of the starting solution. Then, considerations linked to the introduced principal stress constraint are set out through several numerical examples.

5.3.1 Topology optimization problem: volume minimization

The optimization problem we want to focus on is the design of stress-constrained light-weight structures. In particular, the stress problem consists in the minimization of the volume (or mass) fraction while satisfying the stress constraints. The optimization problem reads:

$$\begin{cases} \min \sum_{i=1}^{N} x_i \\ \text{subject to} \\ \quad \boldsymbol{K}\boldsymbol{u} = \boldsymbol{f} \\ \quad \boldsymbol{\sigma} < \boldsymbol{\sigma}_{\boldsymbol{lim}} \\ \quad \mathbf{0} < \boldsymbol{x}_{\boldsymbol{min}} \leq \boldsymbol{x} \leq \mathbf{1}, \end{cases} \tag{5.1}$$

where $\boldsymbol{x}$ is the vector of design variables representing the density of the elements of the mesh, x_i is the elemental density and N indicates the number of elements. While, $\boldsymbol{x}_{\boldsymbol{min}}$ is a vector of minimum relative densities (strictly greater than zero to avoid singularities). $\boldsymbol{K}$, $\boldsymbol{u}$ and $\boldsymbol{f}$ are the global stiffness matrix, the global

displacement and force vectors respectively. Concerning the stress constraint, $\boldsymbol{\sigma}$ is the vector of the calculated stress, and $\boldsymbol{\sigma_{lim}}$ is the vector whose components are all equal to the maximum limit stress allowed.

5.3.2 Algorithm structure

As in the vast majority of topology optimization algorithms, the PSTOpt algorithm runs in an iterative fashion: starting from a seed solution, at each iteration it evaluates the objective function and the constraints, then, accordingly to the used optimization strategy, update the current solution up to convergence (see Figure 5.3). In the following, a detailed description of the main algorithm features and steps is reported.

Description of the continuum domain

The approach used to model the material domain of problem related to equations ((5.1)) is the *density-based approach*. Such approach uses density design variables, x_i, defined for each element of the mesh, and requires that $0 < x_i \leq 1$ for all $i = 1, \ldots, N$. Since a solid-void solution which does not contemplate intermediate densities is desirable, a penalization technique is necessary to obtain densities which tend to 0 - 1 values. The most diffused penalization technique in literature is the *SIMP* (Solid Isotropic Material with Penalization) method [Bendsøe, 1989, Zhou and Rozvany, 1991, Andreassen et al., 2011]. Such method is based on a heuristic relation between x_i and the elemental Young's modulus E_i, given by:

$$E_i = E_i(x_i) = x_i^p E_0 \quad x_i \in (0, 1]\,, \tag{5.2}$$

where E_0 is the Young's modulus of the solid material and p is the penalization power (usually $p \geq 3$). In order to avoid singularity of the global stiffness matrix $\boldsymbol{K}$, a modified *SIMP* approach uses the adjusted relation:

$$E_i = E_i(x_i) = E_{min} + x_i^p \left(E_0 - E_{min}\right) \quad x_i \in (0, 1]\,, \tag{5.3}$$

whit E_{min} being the non-zero elastic modulus of the void material.

Density filtering

Two pathological behavior normally arise from topology optimization analysis, i.e., the *mesh-dependecy* Bendsøe and Sigmund [2004] and *checkerboard pattern* Sigmund and Petersson [1998a], Zhou et al. [2001], Sigmund [2007a] phenomenon. The first one is the inconsistency in the quality of the results depending on which finite elements mesh is used, while the *checkerboard pattern* phenomenon consists of alternating areas with void and solid spaces in the optimized configuration. The

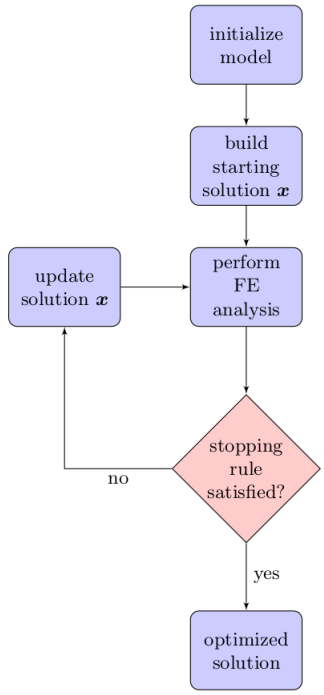

Figure 5.3. General outline of a topology optimization algorithm.

latter problem is related to poor FE modeling and it shows up especially when first order finite elements are used. In order to mitigate *mesh-dependecy* and *checkerboard pattern* occurrence, one of the most common approach consists in using a *density filter*, which rescales the density of the element of the mesh with respect to its neighbors. The procedure adopted in this work is nothing but a weighted local average [Bruns and Tortorelli, 2001] given by the following equation:

$$\bar{x}_i = \frac{\sum_j w_{ij} x_j}{\sum_j w_{ij}} \tag{5.4}$$

where

$$w_{ij} = \begin{cases} \frac{r_{min} - r_{ij}}{r_0} & \text{when} \quad r_{ij} < r_{min} \\ 0 & \text{otherwise.} \end{cases} \tag{5.5}$$

Figure 5.4. Example of checkerboard pattern in simply supported beam, figure taken from Sigmund and Petersson [1998b].

Here $\bar{x_i}$ is the filtered density of the ith-element and x_j is the density of the jth-element before the filtering operation, r_{ij} is the Euclidean distance between the centers of elements i and j, and r_{min} is the filter radius.

5.3.3 Optimization Technique

The optimization method on which the PSTOpt algorithm relies on is a modified version of the heuristic technique proposed in Biyikli and To [2015], which finds a sub-optimal solution without using any gradient information. The algorithm is a simple to implement, iterative method, which carries out at each step a FE analysis and a computation of the stresses. After such computations, the stopping criteria is checked, that is whether the maximum measure of the stress in the structure is close to the stress limit within a prescribed tolerance. In order to avoid premature convergence to poor quality solutions a minimum number of iteration is as well required to terminate the execution of the algorithm. If the criterion returns true, the simulation terminates, otherwise, the algorithm continues to optimize the topology.

At the beginning of the optimization phase a check on the stresses is performed in order to determine the total amount of material needed in the structure. If the computations reveal that the structure is over-stressed, i. e., that the maximum measure of the stress among all elements of the mesh is greater than the stress limit, then some material is added to the structure, otherwise, if the stresses computed are within the stress limits, some material is subtracted.

The target amount of total material needed in the structure (`xTarget`) is computed as follows:

$$\texttt{xTarget} = \begin{cases} \sum_i^N x_i + 0.001 \cdot N, & \text{if the structure is over-stressed} \\ \sum_i^N x_i - 0.001 \cdot N, & \text{otherwise.} \end{cases} \tag{5.6}$$

At this point, each component x_i of the vector of the densities is set to zero and the `xTarget` is distributed proportionally among the elements of the mesh. Such distribution is carried out in accordance with a measure of the stress: in this way

elements with higher stress value are filled with more material. In particular, the amount of material to be distributed to x_i in the i^{th}-element is proportional to the the elemental stress values. It has to be noted that, during this process, the actual amount of total material distributed (`xDist`) can be less than `xTarget` and this is due to the filtering procedure and to a control on the bounds imposed on the design variables, which can result in the truncation of the values x_i that exceed the bounds. The remaining material, `xRemaining`, obtained as the difference between `xTarget` and `xDist`, is then iteratively and with the same proportional strategy distributed to a certain threshold value among the elements of the mesh. For the sake of clarity, a scheme of the described optimization strategy is reported in Algorithm 1.

Algorithm: PSTOpt Algorithm
Set up FE, stress analysis and computation of the filtering matrix W;
Perform FE and stress analysis;
if *(the stresses are below the limits* AND *loop*> 50*)* **then**
  break;
end
if *(the structure is over-stressed)* **then**
  `xTarget`$= \sum_i^N x_i + 0.001 \cdot N$;
else
  `xTarget`$= \sum_i^N x_i - 0.001 \cdot N$;
end
`xRemaining` = `xTarget`;
$x_i = 0 \quad \forall i = 1, \ldots, N$;
Calculation of the vector of the proportion to be distributed (σ_{prop});
while *(xRemaining* > 0.001*)* **do**
  `xDist(i)`=`xRemaining(i)` $\cdot\, \sigma_{prop}(i) \quad \forall i = 1, \ldots, N$;
  $x_i = x_i + W \cdot$ `xDist(i)`;
  check on the bounds imposed on x and cut-off procedure;
  `xRemaining`=`xTarget`-$\sum_i^N x_i$;
end

Algorithm 1: Pseudo-code for the proposed PSTOpt algorithm.

5.3.4 The constraints: principal stress

The main feature of the PSTOpt algorithm consists in the new formulation of the stress constraint. In literature, generally, the Von Mises criterion is used (σ_{vms}) to express the boundary limit for the stress constraint. Henceforth, such constraint

can be expressed as follows:

$$\sigma_{vms} \leq \sigma_{LIM}, \quad \text{for each node of the structure} \tag{5.7}$$

where σ_{LIM} is the maximum value allowed to the Von Mises stress. Starting from the original PTO algorithm, we explore the possibility of a new formulation of the constraints which allows to overcome the use of the Von Mises criterion. This measure of the stress appears to be not highly suitable for concrete design purposes, being more representative of a metal body rather than a concrete structure. The new implemented constraint is based on principal stresses since they can better represent the real behavior of the concrete material, considering at the same time a tension and a compression limit. Consequently, the constraint and the material distribution law (see σ_{prop} term in Algorithm 1) are modified as follows. During the generic iteration, a finite element analysis is performed and the stress tensor $\boldsymbol{\sigma}$ of the current structure is computed. At this point, rather than compute the Von Mises stress we express the tensor $\boldsymbol{\sigma}$ in terms of principal stresses. After such computation, two separate bounds are forced on, respectively, the maximum and the minimum values of the principal stresses. In this way is possible to control asymmetrically the stresses both in case of compression (bound on the minimum value) and traction (bound on the maximum value). Considering a 2D problem, we indicate with σ_x e σ_y the two principal stresses in the x and y principal directions. The new constraints can be represented with the help of Figure 5.5, where for each element in the structure: a value of $\sigma_x = 0$ indicates that the element is not stressed, a value of $\sigma_x < 0$ indicates that the element examined is compressed, while $\sigma_x > 0$ shows that the element is in traction[1].

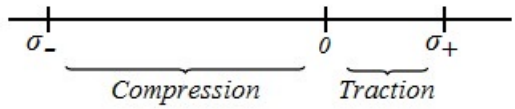

Figure 5.5. Representation of the new constraints where σ_+ e σ_- are respectively the maximum and minimum values allowed to the principal stresses.

Hence, for each integration point, and for each direction, we write the two following constraints:

$$\begin{cases} \sigma_- \leq \sigma_x \leq \sigma_+ \\ \sigma_- \leq \sigma_y \leq \sigma_+. \end{cases} \tag{5.8}$$

In order to complete such new formulation we define the risk factors RF_1 and RF_2

[1] The same applies to σ_y.

for each principal stress direction:

$$\begin{cases} RF_1 = \max\left(\dfrac{\sigma_x}{\sigma_+}, \dfrac{\sigma_x}{\sigma_-}\right) \\ RF_2 = \max\left(\dfrac{\sigma_y}{\sigma_+}, \dfrac{\sigma_y}{\sigma_-}\right) \end{cases} \tag{5.9}$$

Mathematically speaking this procedure consists in the measure of how much the values σ_x e σ_y computed are within the allowed interval $[\sigma_-, \sigma_+]$. Consequently, whenever $RF_i > 1$ then the stress is outside the interval $[\sigma_-, \sigma+]$ and the current solution is not feasible.

Summarizing, the PSTOpt updated strategy translates the PTO algorithm in terms of principal stresses and risk factors. As stated above, with our new formulation of the stress constraints, the structure is considered to be over-stressed once there are elements such that at least one of their associated risk factors, RF_1 and RF_2, is greater than one. According to the new stress constraint, the material distribution has to be modified with the update proportional factor:

$$\sigma_{prop} = \frac{RF_1^q + RF_2^q}{\sum (RF_1^q + RF_2^q)}. \tag{5.10}$$

Recalling the stopping rule of the algorithm, it is inherited from Biyikli and To [2015] except from the inclusion of the RF_i parameter. This criterion lets the algorithm stop if and only if both of the two following statements occur:

1. A minimum number of iterations has been performed;
2. the maximum of the risk factor RF_i is close to 1 within a certain value (in the present study the tolerance is set equal to 0.001).

The first condition prevents premature convergence to sub-optimal solutions, and the second condition is related to the heuristic observation that the most lightweight structure is obtained once that is no longer possible to subtract any amount of material due to the stress limitation, i.e. when the stresses cannot be pushed any forward.

5.3.5 Construction of the starting solution and FE code

Normally, in topology optimization algorithms proposed in literature, a starting solution is obtained by considering a matrix x, whose dimensions are $nelx \times nely$ as the number of elements in the FE mesh, filled with a certain value of the density such that as example:

$$x_i = 0.5 \quad \forall e \text{ in the mesh} \tag{5.11}$$

In the proposed algorithm, by means of the switch parameter `start`, the user can choose the starting filling value or an alternatively option called *split* strategy better explained in the following. The definition of this parameter it is not trivial, because depending on the mesh and on the problem features can lead, at the same time, to some advantages and shortcomings.

- `start`= 1

Choosing the option `start`= 1 it is possible to start the optimization with any desired density value. Setting a value of 0.1, as example, means to start with an almost empty configuration. Since the algorithm fills gradually the solid body, starting from this extremely light (and obviously unfeasible) solution, the feasible region is approached "from below", thus often producing as result an extremely light beam. The main drawback of this approach is the potential high number of iterations required to convergence. On the other hand, choosing a filling value of 0.85, thus with a solution almost totally filled, it is very likely to start from a feasible solution.

- `start`= 2

The choice `start`= 2 builds the solution with a construction phase which is an innovative feature of the algorithm: the `split` procedure. Its setup works as follows. It is assumed that the initial problem is characterized by a `nelx` $\times$ `nely` mesh. The algorithm, in a first step, computes a solution $\bar{\boldsymbol{x}}$ obtained solving the same initial problem on a coarser mesh, as example $\lceil \frac{\texttt{nelx}}{4} \rceil \times \lceil \frac{\texttt{nely}}{4} \rceil$; then, as starting point for the optimization scheme, uses a matrix obtained by "splitting" the components of $\bar{\boldsymbol{x}}$ in accordance with the required accuracy of the finer mesh. Such procedure can strongly improve the algorithmic performances since the construction of a good solution, often near to the final optimized configuration, comes at the reasonable price of solving the problem on the coarser mesh. In Figure 5.6 a graphical depiction of the split procedure is shown.

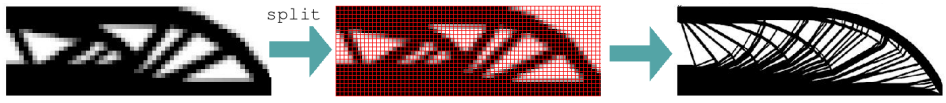

Figure 5.6. Graphical breakdown of the optimization algorithm with the split configuration.

Concerning the FE code, an isoparametric bi-linear quadrilateral element is implemented and the Gauss-Legendre quadrature [Golub and Welsch, 1969] is adopted

as numerical integration technique for the calculus of the elemental stiffness matrix. The code can handle any kind of rectangular geometries (beam-like objects). Element connectivity, nodes coordinates, boundary and load conditions are automatically defined through a subroutine insert in the code. From this point of view, the PSTOpt algorithm is more general and flexible if compared with the PTO code.

5.3.6 Preliminary results

In the following, some preliminary tests are shown comparing results obtained from four different type of mesh, characterized by an increasing refinement. The set boundary conditions correspond to half of the classical "MBB-beam" [Rozvany, 1998] (Figure 5.7). For all four mesh cases, material properties are input as 1 for the Young's modulus E_0 of the solid material, 0.3 for Poisson's ratio ν, and 10^{-9} for the Young's modulus E_{min} assigned to void regions. Penalty value for modified SIMP approach is set to 3. Lower and upper bounds x_{lim} on the elemental density are limited to 0 and 1. A unitary force is applied vertically at the mid-span of the beam. Element edge length L and filter radius r_{min} are set to 1 and 1.5, respectively.

For each type of mesh, different bounding values σ_+ and σ_- are tested to asses the influence of the stress condition in the final layout of the beam. The bounding values adopted for the parametric study are calibrated considering maximum and minimum principal stress values calculated for an equivalent bulk beam. For each couple of σ_+ and σ_-, outcomes from both the switch statement `start`= 1 and `start`= 2 (*split* strategy) are displayed. In reporting results, the fraction of the final optimized volume and the total computation time are specified for each beam. The optimized configuration is represented by the plot of the density $\boldsymbol{x}$ over the domain.

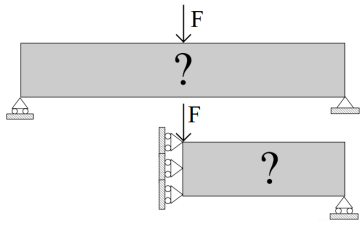

Figure 5.7. Representation of the classical "MBB beam" instance.

Mesh 120x40

(a) $m = 0.65$, $t = 30.58s$ **(b)** split, $m = 0.69$, $t = 43.46s$

Figure 5.8. Optimized beams obtained with the normal procedure (a) and the *split* strategy (b) considering as imposed stress limits $\sigma_- = -0.85$, $\sigma_+ = 0.5$.

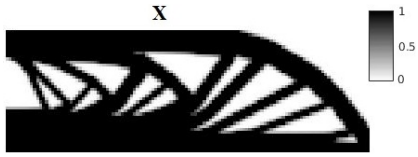

(a) $m = 0.66$, $t = 37.10s$ **(b)** split, $m = 0.62$, $t = 56.26s$

Figure 5.9. Optimized beams obtained with the normal procedure (a) and the *split* strategy (b) considering as imposed stress limits $\sigma_- = -0.9$, $\sigma_+ = 0.5$.

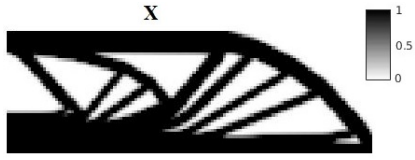

(a) $m = 0.57$, $t = 51.03s$ **(b)** split, $m = 0.57$, $t = 64.02s$

Figure 5.10. Optimized beams obtained with the normal procedure (a) and the *split* strategy (b) considering as imposed stress limits $\sigma_- = -0.1$, $\sigma_+ = 0.5$.

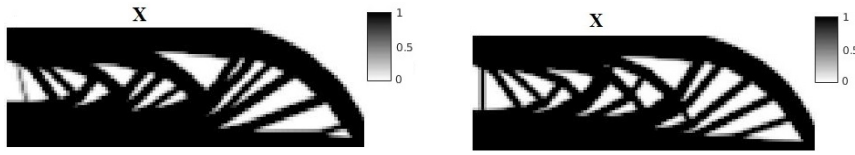

(a) $m = 0.73$, $t = 21.42s$ **(b)** split, $m = 0.70$, $t = 53.61s$

Figure 5.11. Optimized beams obtained with the normal procedure (a) and the *split* strategy (b) considering as imposed stress limits $\sigma_- = -0.85$, $\sigma_+ = 0.6$.

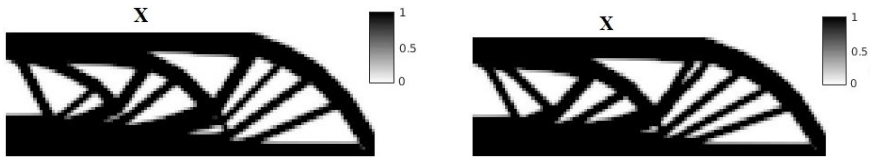

(a) $m = 0.63$, $t = 40.46s$ **(b)** split, $m = 0.63$, $t = 53.40s$

Figure 5.12. Optimized beams obtained with the normal procedure (a) and the *split* strategy (b) considering as imposed stress limits $\sigma_- = -0.9$, $\sigma_+ = 0.6$.

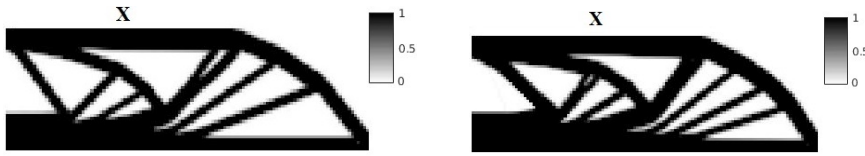

(a) $m = 0.53$, $t = 58.56s$ **(b)** split, $m = 0.60$, $t = 59.15s$

Figure 5.13. Optimized beams obtained with the normal procedure (a) and the *split* strategy (b) considering as imposed stress limits $\sigma_- = -1$, $\sigma_+ = 0.6$.

(a) $m = 0.60$, $t = 43.65s$ **(b)** split, $m = 0.63$, $t = 54.11s$

Figure 5.14. Optimized beams obtained with the normal procedure (a) and the *split* strategy (b) considering as imposed stress limits $\sigma_- = -0.9$, $\sigma_+ = 0.7$.

(a) $m = 0.53$, $t = 55.48s$ **(b)** split, $m = 0.53$, $t = 68.91s$

Figure 5.15. Optimized beams obtained with the normal procedure (a) and the *split* strategy (b) considering as imposed stress limits $\sigma_- = -1$, $\sigma_+ = 0.7$.

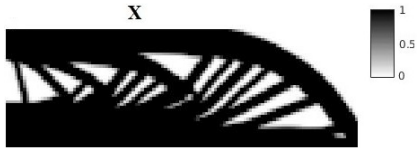

(a) $m = 0.73$, $t = 22.39s$ **(b)** split, $m = 0.73$, $t = 43.97s$

Figure 5.16. Optimized beams obtained with the normal procedure (a) and the *split* strategy (b) considering as imposed stress limits $\sigma_- = -0.85$, $\sigma_+ = 0.7$.

Mesh 240x80

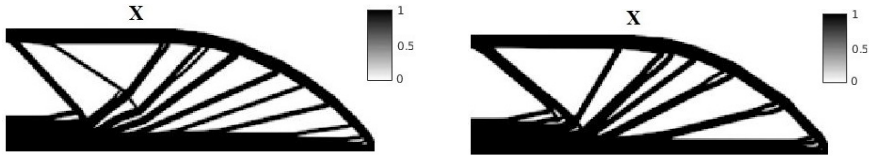

(a) $m = 0.44$, $t = 391.39s$ **(b)** split, $m = 0.43$, $t = 281.79s$

Figure 5.17. Optimized beams obtained with the normal procedure (a) and the *split* strategy (b) considering as imposed stress limits $\sigma_- = -0.85$, $\sigma_+ = 0.28$.

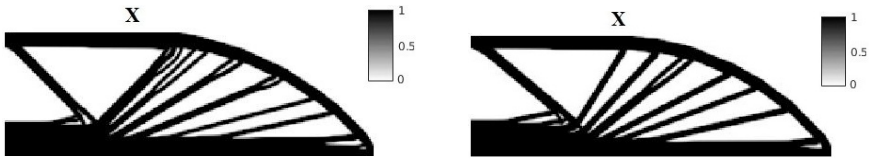

(a) $m = 0.44$, $t = 363.16s$ **(b)** split, $m = 0.42$, $t = 273.47s$

Figure 5.18. Optimized beams obtained with the normal procedure (a) and the *split* strategy (b) considering as imposed stress limits $\sigma_- = -0.9$, $\sigma_+ = 0.28$.

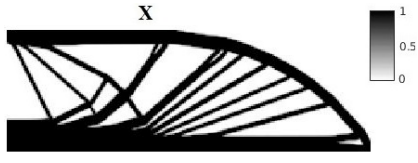

(a) $m = 0.43$, $t = 343.74s$ **(b)** split, $m = 0.41$, $t = 246.37s$

Figure 5.19. Optimized beams obtained with the normal procedure (a) and the *split* strategy (b) considering as imposed stress limits $\sigma_- = -0.85$, $\sigma_+ = 0.3$.

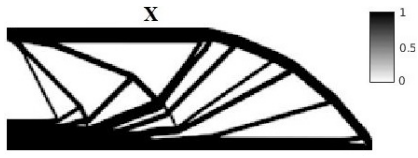

(a) $m = 0.40$, $t = 356.75s$ **(b)** split, $m = 0.40$, $t = 260.23s$

Figure 5.20. Optimized beams obtained with the normal procedure (a) and the *split* strategy (b) considering as imposed stress limits $\sigma_- = -0.85$, $\sigma_+ = 0.38$.

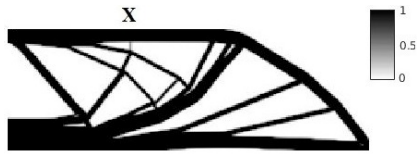

(a) $m = 0.41$, $t = 359.41s$ **(b)** split, $m = 0.37$, $t = 271.92s$

Figure 5.21. Optimized beams obtained with the normal procedure (a) and the *split* strategy (b) considering as imposed stress limits $\sigma_- = -0.85$, $\sigma_+ = 0.4$.

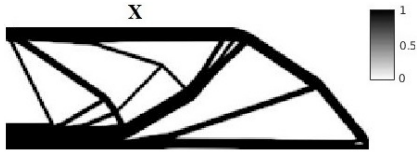

(a) $m = 0.36$, $t = 387.79s$ **(b)** split, $m = 0.35$, $t = 323.37s$

Figure 5.22. Optimized beams obtained with the normal procedure (a) and the *split* strategy (b) considering as imposed stress limits $\sigma_- = -0.85$, $\sigma_+ = 0.5$.

Looking at the results reported for the first two set of meshes (120x40 and 240x80) it is already possible to derive some interesting considerations. Concerning the efficiency of the algorithm, we can immediately noticed that the *split* strategy (`start`= 2) does not produce an improvement in the computational time if the mesh adopted is particularly coarse. Indeed, for all the analyzed case of the 120x40 mesh, the time t related to the *split* case is always greater than the one related to the option `start`= 1. While, moving to the second 240x80 mesh, the computational time registered with the *split* procedure decreases in all the cases. In addition, *split* solutions related to the finer mesh cases (240x80 mesh) are closer to the ones obtained with the option `start`= 1. Thus, the starting strategy should be chosen according to the mesh and the *split* case adopted when enough accurate mesh are used for the discretization. Comparing results from the two set of mesh, the topologies are mesh dependent since a different layout is obtained considering the same set of bounding stresses but different meshes. An example of this effect is clearly shown by comparing the beams depicted in Figures 5.8 and 5.17. Furthermore, we can notice that the optimized configurations from the first mesh tend to have thicker structural members while those from the second mesh incline towards a greater number of thinner structural members, as expected.

Mesh 480x160

The purpose of the following tests is simply to the show solution quality obtained with a finer mesh. Same conclusions, in fact, would be recovered from a detailed parametric study on this mesh cases. For this reason, because of the high amount of elements, here the algorithm is stopped at the first feasible solution after a minimum number of iterations (Min_It). To save computational time, we decide to report only the outcome obtained with the *split* strategy. The same choice is made for the 960x320 mesh.

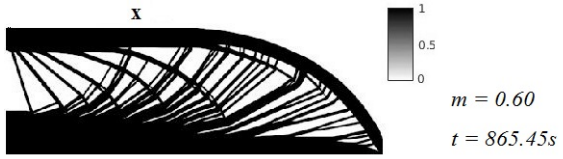

Figure 5.23. Optimized beam obtained with the *split* strategy considering as imposed stress limits $\sigma_- = -0.82$, $\sigma_+ = 0.271$ and $Min\_It = 200$.

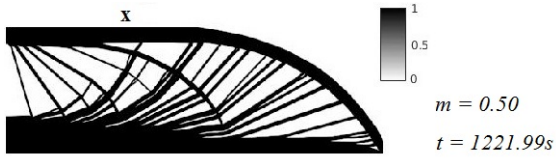

Figure 5.24. Optimized beam obtained with the *split* strategy considering as imposed stress limits $\sigma_- = -0.82$, $\sigma_+ = 0.271$ and $Min\_It = 300$.

Mesh 960x320

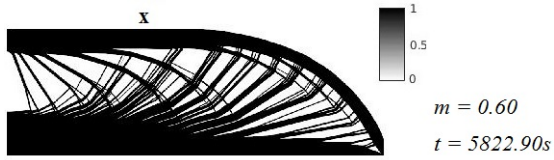

Figure 5.25. Optimized beam obtained with the *split* strategy considering as imposed stress limits $\sigma_- = -0.82$, $\sigma_+ = 0.271$ and a $Min\_It = 200$.

Solutions from the 480x160 and 960x320 meshes underline the effect induced by a principal stress-driven optimization, i.e., that the shape of the final structures seem to follow principal stress lines directions. This is very interesting since the final topologies closely recall the optimal grid-like continua studied by Michell [1904] who contributed to exact analytic solutions for several well-known truss structures. The comparison of the last beams (Figure 5.23-5.25) suggests that the algorithm is going in the right direction because the related density distributions are very similar. Consequently, for such beams the mesh-dependency effect is also reduced.

Another point that should be commented is the optimization response to the variation of the stress constraint values. Considering the cases studied with the 120x40 mesh, as example, a slight modification on the σ_- and σ_+ values produce significant differences in the final layouts. On one hand this effect makes difficult the evaluation of the quality of the solution, also because there are no examples coming from other literature methods comparable with it. On the other hand, the optimized beam present a reasonable shape, especially looking at the solutions reported for the 480x160 and 960x320 meshes. In addition, considering a case study with real material parameters, it is important to take into account the different order of magnitude that can characterize the stress bound values. As example for the concrete material the traction limit σ_+ is normally of a lower order of magnitude if compared with the σ_- limit, because of its better behavior in compression. For

this reasons and considering the following numerical analysis on a real case stud, it is considered appropriate to update equation (5.10) with:

$$\sigma_{prop} = \frac{1}{2} \cdot \left(\frac{RF_1^q}{\sum (RF_1^q)} + \frac{RF_2^q}{\sum (RF_2^q)} \right) \tag{5.12}$$

This simple modification allows to consider the possible different order of magnitude of the stress limits and correctly weight their contribution in the material distribution law. The updated algorithm is tested in Section 5.3.7 with the study on a concrete beam characterized by material parameters, load conditions and stress limits taken from a real case study.

5.3.7 Real case study: concrete beam

According to the considerations made in the previous Section, here in the following, the PSTOpt algorithm is evaluated on a realistic concrete beam, characterized by dimensions depicted in Figure 5.26. Results obtained from three different type of mesh characterized by an increasing refinement are compared. Concerning the optimization parameters, we maintained the same penalty value P and lower and upper bounds x_{lim} used in the preliminary tests.

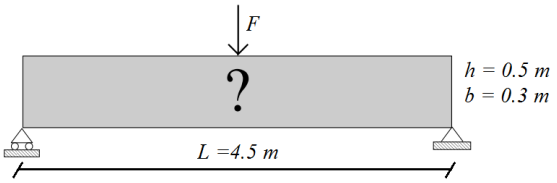

Figure 5.26. Geometry and BCs of the concrete studied beam.

The material parameters adopted for the concrete are $E_0 = 30000$ N/mm^2 for the solid elements and a $\nu = 0.2$. Regarding the value assigned to the void elements we assume an $E_{min} = 0.005$. This particular choice allows to avoid numerical singularities and bad conditioning of the stiffness matrix linked to low values of the E_{min}. More details about this issue are reported in Section 5.4. The initial load conditions considered for the test is a concentrated force F applied at the mid-span of the beam. The following limit values are assumed for the principal stresses:

- σ_{compr} = -20 N/mm^2
- $\sigma_{trac} = 1$ N/mm^2

It is worth to notice that, in this test, the stress bounding values are chosen according to the real behavior of the material, which present a different response

in traction and compression. The value of the force F is recovered considering the classic Navier's formula for determining the stress (equation (5.13)) in a beam under simple bending. Choosing and appropriate value for the maximum stress allows to recover a force value so that there is margin for the optimization without overcoming the stress limits. Figure 5.27 shows the conventional stress distribution in a rectangular beam.

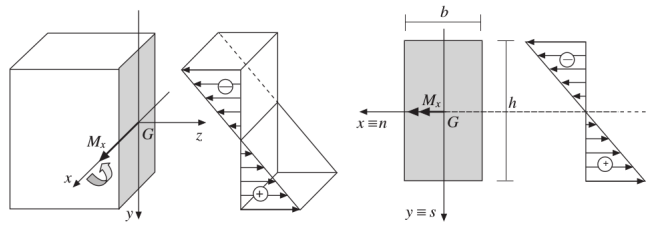

Figure 5.27. Deflection of a beam deflected symmetrically and stress diagram.

$$\sigma_{max} = \frac{M_x}{I_x}\frac{h}{2} \tag{5.13}$$

Considering a simply supported beam with a rectangular cross section under a concentrated load the moment at the mid-span is $M_x = FL/4$ (where L is the lenght of the beam) and equation (5.13) becomes:

$$\sigma_{max} = \frac{3FL}{2bh^2} \rightarrow F = \frac{2\sigma_{max}bh^2}{3L} \tag{5.14}$$

By imposing a $\sigma_{max} = 0.5Mpa$ and considering geometric data reported in Figure 5.26 we obtain an F = 5555 N.

Analysis on the bulk beam

Before going towards optimization analysis and results, some considerations about the bulk beam and load case described above are reported. Figure 5.28 shows the contour plot of the principal stresses $sigmaprinc_1$ and $sigmaprinc_2$. The unit of measure for the principal stress is Mpa. Table 5.1 resumes the values of some significant parameters obtained from the numerical analysis.

Comparing the vertical displacement u_y calculated at the point A (see Figure 5.28) with the analytic solution (f) there is good agreement between the values, as foreseen. At the same time, we expect stress singularities at the application point of the load. As we keep refinement on the mesh, the stress at this point

keeps increasing and increasing, thus not converging towards a specific value. This effect is clearly visible by looking at the plots reported in Figure 5.28 and the concentration of the stress in the upper left corner.

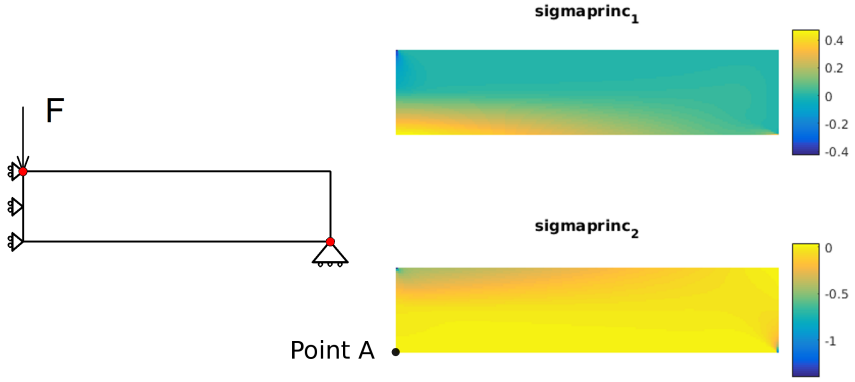

Figure 5.28. Plot of the principal stresses $sigmaprinc_1$ and $sigmaprinc_2$.

u_y	$max\sigma_{11}$	$max\sigma_{12}$	$max\sigma_{22}$	$max\sigma_{princ}$	$min\sigma_{princ}$
-0.1189 mm	0.48 Mpa	0.06 Mpa	0.49 Mpa	0.48 Mpa	-1.40 Mpa

Table 5.1. Significant parameters obtained from the numerical analysis on the bulk beam.

- **Analytical solution**: $f = \dfrac{FL^3}{48EJ} = -0.11138$ mm

It is immediately clear that this issue affects the PSTOpt algorithm since is stress-driven. At each iteration, in fact, all the stress values are compared with the bounding limits and if one or more elements are over-stressed the optimization process is compromised. The algorithm will always find a value overcoming the stress limits and, as a consequence, will continue to increase the amount of mass without reaching an optimal solution. Obviously, such behavior easily occurs in refined and accurate mesh for the reasons explained above. A typical solution from the PSTOpt algorithm for a combination of mesh and stress limits affected by stress singularities is reported in Figure 5.29. For this case, a 450x100 mesh is adopted together with the bounding values and the load force indicated above. This problem has been already faced by the topology optimization community [Le et al., 2010, Picelli et al., 2017] but most of the proposed solutions are applied to gradient-based methods rather then heuristic ones, which are less diffused. For this reason,

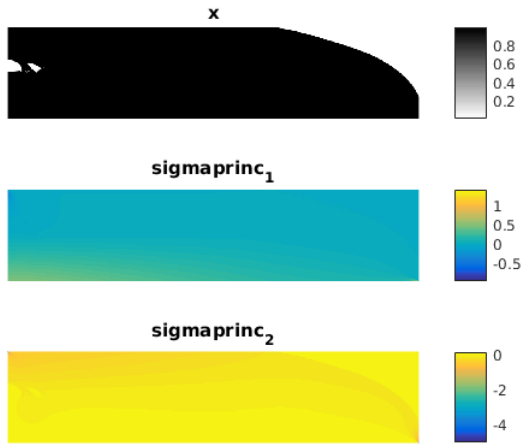

Figure 5.29. Typical optimized beam obtained from a combination of mesh and stress limits affected by stress singularities.

to have accurate results and overcome this issue, a customized strategy should be applied to the proposed algorithm. As stated by the St. Venant's principle [Mariano and Galano, 2015], the effect of local disturbances to a uniform stress field remains local. Thus, in the areas quite far from the singularity points the effect is not visible and significant. The proposed strategy is named *singularity check option* and is based on the aforementioned principle. The idea is, firstly, to check the stresses only in the zones where the stress singularity is supposed to occur. Then, once the problematic elements are individuated, the measured stresses are suitably re-calibrated. In particular, the steps performed through the *singularity check option* are:

- Identification of the affected area;
- Choice of an appropriate radius R which identifies the n-elements to be "fixed" (see Figure 5.30);
- Check of the σ_{princ} values on the identified n-elements;
- Correction of the singularity on the n-elements : if the elemental $\sigma_{princ}(el)$ is lower (greater) than the compression limit $\sigma_{lim(-)}$ (traction limit $\sigma_{lim(+)}$) then $\sigma_{princ}(el)$=$\sigma_{lim(-)}$ ($\sigma_{lim(+)}$).

Applying this option at each iteration of the analysis it is possible to avoid disturbances and the maximum values registered correspond to the limit values which is a normal condition for the PSTOpt algorithm.

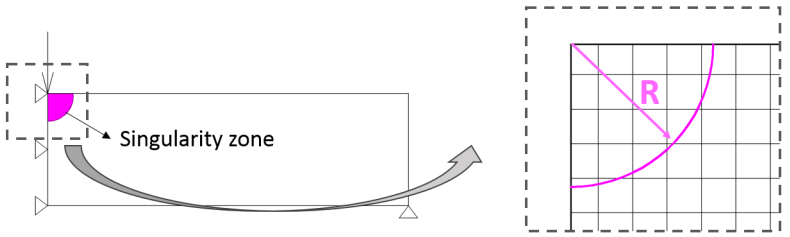

Figure 5.30. Singularity zone and radius R for the identification of the problematic elements.

Preliminary optimization results on the case study

In the following, preliminary results for the analyzed concrete beam are reported applying the *singularity check option* to the PSTOpt algorithm. Table 5.2 resumes the mesh types, load condition and starting density value of the test cases. In reporting results, the fraction of the final optimized volume (Avg_ρ) and the total computation time (T) are specified for each beam. The optimized configuration is represented by the plot of the density x over the domain. For each case, the trends of the average density and the maximum value of the risk factor over the number of iterations are provided together with a summary table with the values of some of the most significant quantities.

	Mesh	F	ρ
CASE 1	225x50	5500 N	0.85
CASE 2	450x100	5500 N	0.85
CASE 3	900x200	5500 N	0.85

Table 5.2. Optimization case tests for an F = 5550 N and a initial density of ρ=0.85 varying the mesh.

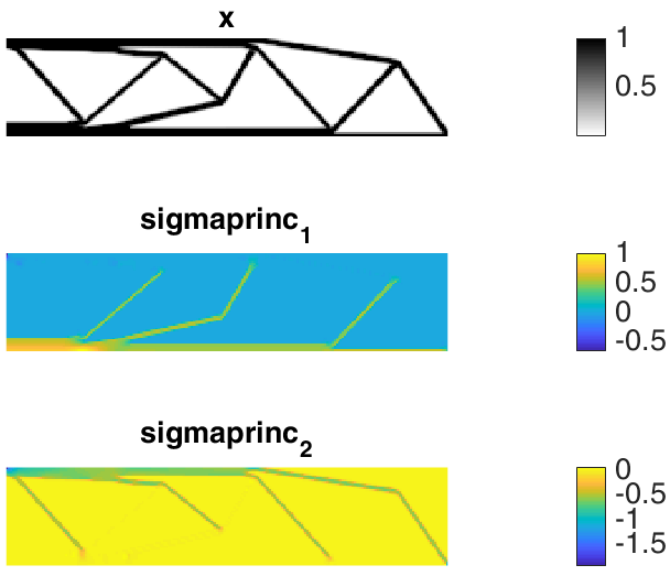

Figure 5.31. CASE 1, optimized beam. $N°$ iterations=616, T=323.8 s, Avg_ρ=0.26.

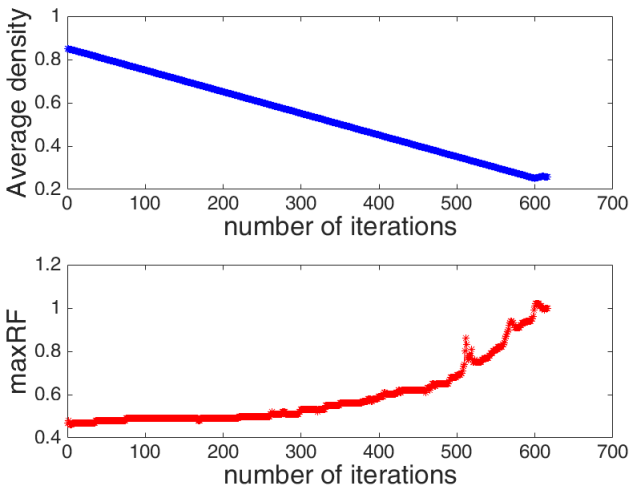

Figure 5.32. CASE 1, average density and maximum value of the risk factor over the number of iterations.

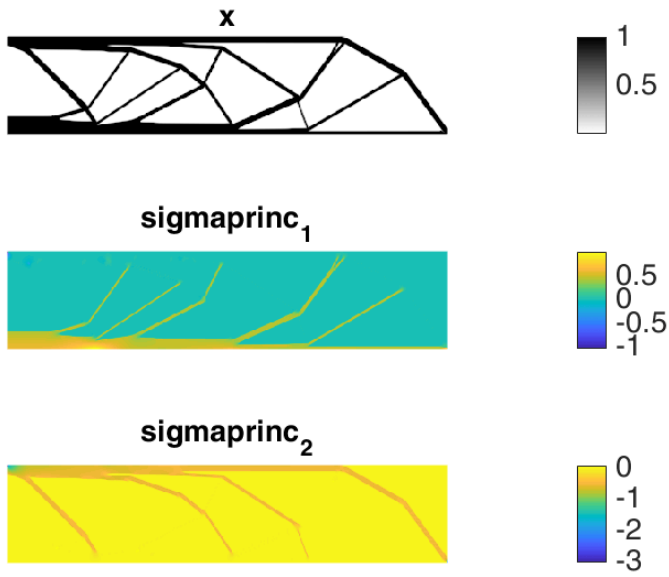

Figure 5.33. CASE 2, optimized beam. $N°$ iterations=601, T=601.8 s, Avg_ρ=0.26.

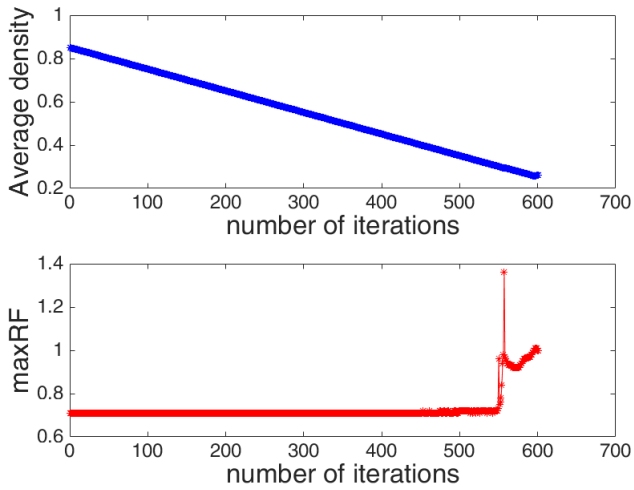

Figure 5.34. CASE 2, average density and maximum value of the risk factor over the number of iterations.

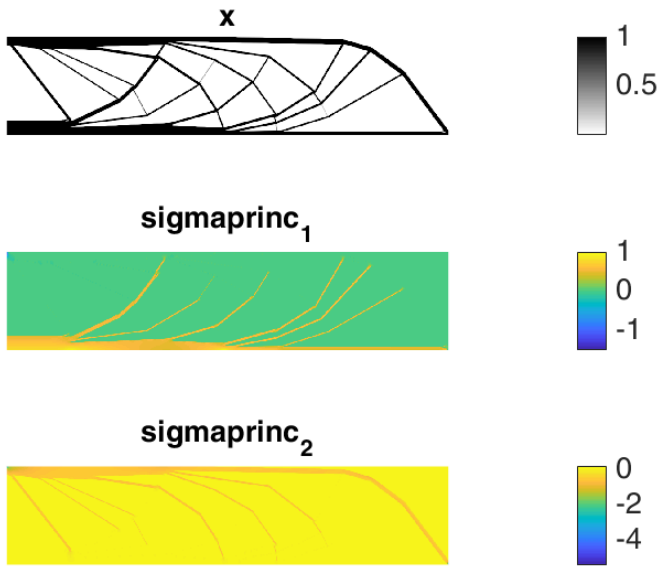

Figure 5.35. CASE 3, optimized beam. $N°$ iterations=639, T=2239.1 s, Avg_ρ=0.22.

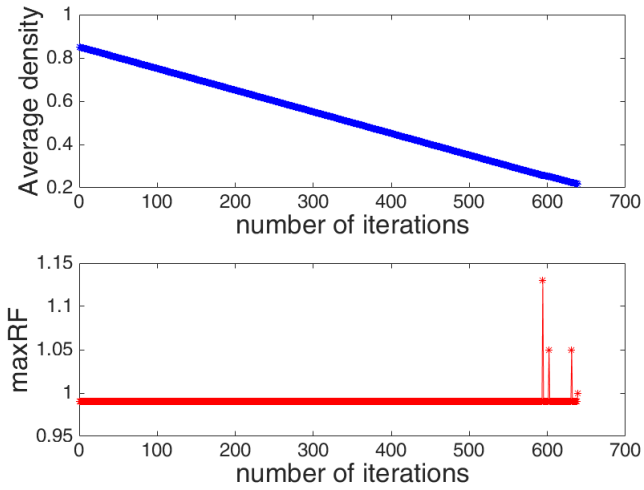

Figure 5.36. CASE 3, average density and maximum value of the risk factor over the number of iterations.

u_y	$max\sigma_{11}$	$max\sigma_{12}$	$max\sigma_{22}$	$max\sigma_{princ}$	$min\sigma_{princ}$
-0.30 mm	1.00 Mpa	0.42 Mpa	0.50 Mpa	1.00 Mpa	-1.93 Mpa

Table 5.3. CASE 1, results from the optimized beam.

u_y	$max\sigma_{11}$	$max\sigma_{12}$	$max\sigma_{22}$	$max\sigma_{princ}$	$min\sigma_{princ}$
-0.27 mm	1.00 Mpa	0.42 Mpa	0.98 Mpa	1.00 Mpa	-3.05 Mpa

Table 5.4. CASE 2, results from the optimized beam.

u_y	$max\sigma_{11}$	$max\sigma_{12}$	$max\sigma_{22}$	$max\sigma_{princ}$	$min\sigma_{princ}$
-0.32 mm	1.35 Mpa	0.56 Mpa	1.95 Mpa	1.00 Mpa	-5.42 Mpa

Table 5.5. CASE 3, results from the optimized beam.

Looking at the optimized beams in Figures 5.31, 5.33 and 5.35 we can immediately noticed that the the problem of mesh dependency appears to be not completely overcome as for the preliminary tests reported in the previous section. In spite of the filtering procedure, in fact, different meshes lead to differences in the optimized topology, showing the low reliability of the results when coarse mesh are used (CASE 1). It seems that the quality of the mesh in stress-constrained problem is more insidious than in compliance minimization ones where good topologies are obtained from low quality mesh. The density distribution corresponding to the more refined mesh of CASE 2 and CASE 3 are in better agreement. Focusing the attention on Figure 5.35, it is possible to note that final layout of the structure seems to follow principal stress lines direction and recall the Michell optimized structures, as underlined in the preliminary tests.

Concerning the *singularity check option*, it works properly since able to solve the problem illustrated in Figure 5.29. Indeed, for the same 450x100 mesh and stress bounding values, the optimization succeed producing the optimized configuration of Figure 5.33. From the plots of the maximum risk factor over the number of iterations it is possible to understand where (i.e. in which mesh) the *singularity check option* is fixing stress singularities. Indeed, the flat line characterizing the curves reported in Figures 5.34 and 5.36 proves that there are high stresses which have to be artificially modified in order to avoid numerical issues. Such flat line stands around the value 1, which is the maximum value allowed for the risk factor considering the constraint on the principal stresses (see Section 5.3.4). The effect of the *singularity check option* is absent in CASE 1 (see Figure 5.31) because the stress concentration is not registered. For the cases considered, this option is practically driven by the $sigmaprinc_1$ due to the fragile tensile behavior of the concrete which

leads the response of the beam.

Finally, looking at the plots of the average density over the number of iterations, the algorithm seems to converge and reach a stationary behavior. Nevertheless, it should be recalled the simplicity of the stopping criteria and the mass distribution adopted for the PSTOpt code. This two aspects are very important in the perspective of an efficient and reliable optimization code and will be object of future research.

5.4 Kratos topology optimization application

Structural and shape optimization is one of the main field of research of the Statik Chair (TUM) coordinated by Professor Kai-Uwe Bletzinger. A new topology optimization application (TopOpt application) has been developed inside the open-source multiphysics software Kratos by Daniel Baumgrtner (associate researcher at the Statik chair) and his master students. The implementation shall allow to optimize 3D structures with arbitrary geometry, while producing some benefits compared to the given open-source capabilities. The TopOpt application also covers a significant portion of the entire structural design process and it is competitive if compared with the available open-source topology optimization software [Andreassen et al., 2011, Talischi et al., 2012, Liu and Tovar, 2014a, Aage et al., 2015]. In the following, main theoretical aspects of the formulation at the basis of the TopOpt application are briefly recalled. Since the code is the result of the work contained in the unpublished dissertations by Baske [2015] and Farias [2016], literature references will be reported along with the summary of the theoretical formulation. Several optimization problems on realistic geometries, load conditions and materials have been performed through the TopOpt application. In particular, in the present thesis, numerical results obtained from the geometries 3D printed at the Naples laboratory are analyzed and discussed.

5.4.1 Topology optimization problem: compliance minimization

The TopOpt application allows to solve compliance problems consisting in the minimization of the compliance while satisfying a volume fraction constraint. It is simpler compared to the stress constrained problem and has been widely investigated in literature in the past two decades [Sigmund, 2001, Liu and Tovar, 2014b, Bendsøe and Sigmund, 2013]. Making use of the density based approach, the formulation of the minimum compliance problem can be expressed as follows:

$$\begin{cases} \min c(\boldsymbol{x}) = \boldsymbol{u}^T \boldsymbol{K} \boldsymbol{u} \\ \text{subject to} \\ \quad \frac{V(\boldsymbol{x})}{V_0} = v \\ \quad \boldsymbol{K}\boldsymbol{u} = \boldsymbol{f} \\ \quad \mathbf{0} < \boldsymbol{x_{min}} \leq \boldsymbol{x} \leq \mathbf{1}, \end{cases} \tag{5.15}$$

where c is the compliance function, $\boldsymbol{u}$ and $\boldsymbol{f}$ are respectively the global displacement and force vectors, $\boldsymbol{K}$ is the global stiffness matrix, $\boldsymbol{x}$ is the vector of design variables representing the density of the elements of the mesh, and $\boldsymbol{x_{min}}$ is a vector of minimum relative densities (strictly greater than zero to avoid singularities). For what concerns the volume constraints, $V(\boldsymbol{x})$ is the total material volume of the structure, V_0 is the design domain volume and v represents the prescribed volume

fraction.

5.4.2 Algorithm structure and optimization technique

The TopOpt application belongs to the gradient based topology optimization tools and is built using the density based SIMP approach (as for the Matlab code presented in Section 5.3). As known, the use of the SIMP lead to deal with mesh-dependency, checkerboard patterns and global optima convergence [Bendsøe and Sigmund, 2013]. In this case, such shortcomings are overcame by employing some of the filtering techniques proposed by Sigmund [2007b]. In particular, a density filter and a sensitivity filter have been introduced in the code to fix the mentioned issues. Choosing a gradient-based method, sensitivities in the form of gradients need to be calculated under the influence of the specific optimization algorithm. To determine the gradient, the algorithm makes use of the adjoint method, since it is one of the most efficient method when the problem is characterized by only one objective function with many design variables [Bletzinger et al., 2008, Stavropoulou, 2015]. Among the optimization algorithms, the Optimality Criteria (OC) method has been selected for the TopOpt application since simple and efficient in one constraint problem, due to the faster convergence. In this method, the design variables are updated towards a discrete black and white solution by following Bendse's updating scheme [Bendsøe, 1995]. The task of the TopOpt algorithm is to find an optimal material distribution by maximizing its stiffness with a constraint set on the permissible amount of material. The required steps are synthesized by the scheme illustrated in Figure 5.37.
After the definition of the initial design domain, the process begins by setting an equal user-specified volume fraction value to all elemental design variables (elemental densities) throughout the whole body. Once the FE analysis step is performed, gradients are computed for the strain energy (objective function) and the volume fraction (constraint function) within a sensitivity analysis. Afterwards, filters are applied to fix the complications arising from the SIMP method. Then, at the end of every optimization loop (where design variables are updated), a comparison between the previous objective value and the current one is made to observe if convergence has been reached, by having a lower value than the user-specified tolerance. This means, that increasing the tolerance value will cause the number of iterations to decrease as the result becomes less accurate. After some iterations within the optimization process, a solution is reached. The final structure has a new rearranged material which has a minimized compliance (maximized global stiffness) compared to the initial one. A post-processing stage referred in order to extract the new geometry and visualize the optimized final layout.

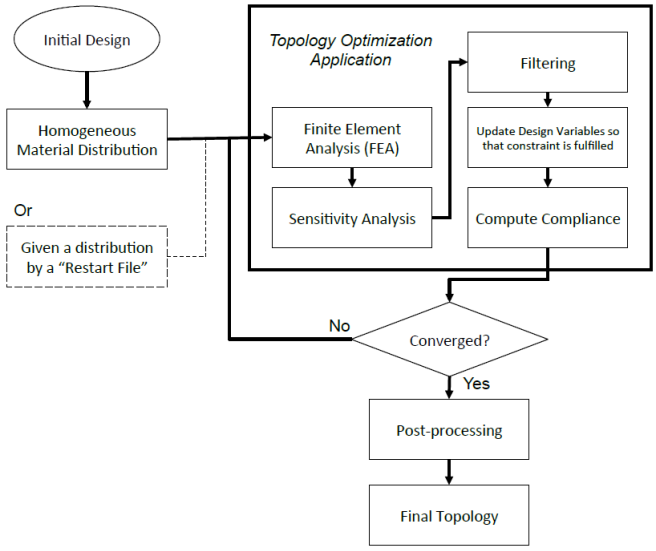

Figure 5.37. Flow Chart of the TopOpt algorithm [Farias, 2016].

5.4.3 TopOpt application

Here in the following the main features and the interface functioning of the used TopOpt application are described.

Tool capabilities and options

- Ability to analyze and optimize arbitrary geometries in 3D domains and availability of a link to pre-processing tools used for the creation of the initial model.
- Option which makes possible to assign active and passive elements within the studied domain.
- Integrated structural solver that is able to handle very large ("industry-size") problems, and that includes parallelization capabilities.
- FE library with tetrahedral and hexahedral elements.
- Organization of the application based on analyzers and controllers. It consists in an efficient master-slave solver proposition having the structural analysis as the slave and the optimization scheme as the master.

- Built-in post-processing capabilities to process the optimal design (i.e. surface extraction or smoothing functionality) and link to further post-processing tools.

- Availability of the optimal design and optimization functionality in an API (Application Programming Interface) that uses a high-level programming language (such as Python), that is needed to customize the software and to be able to work on the optimal design directly on script level.

- Possibility of saving a "Restart File" to gain computational time when interrupted analysis have to be re-run.

TopOpt user interface

The TopOpt Application is established on the framework developed in Kratos, based on two different programming languages: C++ and Python. The first one is used for fast performance operations, low-level memory manipulations and it is characterized by high flexibility in big design domains; the latter one is employed specifically for the user by bringing an easy environment to program and define process flows in a simple readable code. Furthermore, the TopOpt application uses GiD [Ribó and Riera, 2008] as its pre- and post-processor, since it can handle the definition of model's geometry, the creation of the mesh and the setting of the boundary and load conditions. A scheme of the design process stages covered with Kratos and the GiD software are depicted in Figure 5.38. The input file for the optimization analysis is built through the use of the GiD software. Then, a folder containing the GiD input files and other required files for the job has to be created. In particular, the folder contains two main Python scripts: the *OptimizationParameters.py* and the *run_TopOpt.py*. The first one stores all the values and user-parameters (design variable, filtering options etc.) that the program requires in order to find a solution to the problem. The second script constructs an optimizer, referenced to another python file called *topology_optimizer_ factory.py*, where the model part and optimization parameters are stated. Then, the optimization starts by calling the created optimizer and runs the adjusted FE analysis.

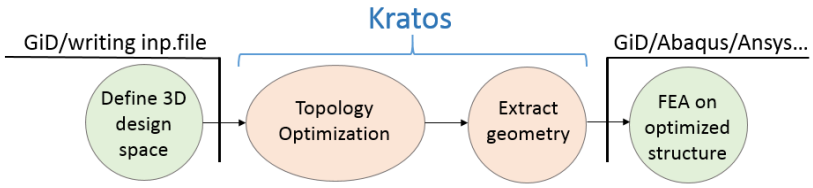

Figure 5.38. Stages of the design process covered by the Kratos and the GiD software.

The implementation of a post-processing approach resulted in a key feature to assess further analysis, review results in a detailed form, and corroborate that the settings employed in the simulation are the correct ones [Lakshmininarayana, 2004]. At the end of the optimization process, the post-processing step included in Kratos allows volume and surface extraction. This is performed by calling a Python script named *run_TopOpt_PostProcessing.py* which takes information from the "Restart File" produced at the end of the optimization. Then, the volume extraction relies on a procedure in which a threshold value dictates which elements are saved and which ignored based on the calculated "X_PHYS" vector (i.e. the vector of the elemental densities). The threshold value modifies the final extracted structure. Consequently, geometries that have a bigger threshold value result in a less number of elements, and vice versa. The surface extraction feature implemented in the code is based on the iso-surface extraction approach suggested by Wolf et al. [2015]. In a nutshell, the method allows to transform a 3D-tetahedral mesh into a 2D-triangular mesh and to generate an *stl* file [Roscoe et al., 1988] which can be imported in most of the post-processing available software. Since what obtained is simply a "raw" surface, as additional option a Laplacian smoothing algorithm [Vollmer et al., 1999] is introduced in the post-processing procedure to produce smooth surfaces from the optimal topologies. The level of smoothness required can be set by specific control parameters.

After having gained experience with the TopOpt application and GiD on simple problems, a second phase of the study moves towards more complex problems. For the sake of clarity, Tables 5.6 and 5.7 show an example of typical input and output parameters reported for the following optimization analysis.

E_{min}	Rel tol	Max $n°$ it	r_{filter}	$size_{elem}$	V fraction
0.01 Mpa	1e-06 Mpa	1000	0.03	0.008	0.3

Table 5.6. Typical input file parameters of an optimization analysis.

where:

- E_{min} = appropriate "small" number assigned to the void element;
- Rel tol = user-defined relative tolerance;
- Max $n°$ it = maximum number of iteration;
- r_{filter} = radius for the density filter (checkerboard effect);
- $size_{elem}$ = size of the mesh element;
- V fraction = volume fraction assigned to the initial domain.

Obj f	Abs Obj	n° it	t_{step}	t_{tot}
0.000717	-76.97%	57	20s	1284s

Table 5.7. Typical output file parameters of an optimization analysis.

where:

- Obj f = compliance objective function;
- Abs Obj = percentage improvement of the Obj f parameter (how much it is decreased);
- n° it = total number of iteration;
- t_{step} = time employed for each step; (checkerboard effect);
- t_{tot} = total analysis time.

5.4.4 Topology optimization tests on the 3D printed geometries

Here, results from the TopOpt application when applied to practical examples are presented. In particular, the analyzed geometries take inspiration from the tests cases introduced in Section 4.2.5. The purpose of this study is to understand in which measure the code under investigation is suitable for the proposed 3D printing approach and which further steps could be made in that direction. The application, in fact, has a great potential being open-source.

Straight concrete beam

The object of the optimization is a "MBB beam" (Figure 5.39 (a)), one of the most basic benchmark examples. In this case it consists in a simply supported beam made of concrete, loaded with a concentrate force applied at the mid-span in the negative y-direction. The model for this section is shown in Figure 5.39 (b). Since the purpose is to try to take in consideration the real limitations imposed by the 3D printing technology, we decide to model the beam in terms of "slice" to respect the constraint of the cross-section modularity in the z-direction (see Section 4.2). Recalling the description of the proposed 3D printing approach, we consider this geometry as the first layer of the printed object characterized by a thickness of 2.5 cm (i.e. the diameter of the nozzle used in the extrusion process). Thus, considering also displacements in the z-direction constrained in all the nodes of the mesh, the 3D model is practically reduced to a 2D model. Consequently, assuming a beam made of 16 layers and an applied force $F_{tot} \simeq 1000$ N, the re-scaled force applied at half of the beam (exploiting the symmetry condition) is $F_{layer} = 60$ N. The material parameters adopted are E = 30000 N/mm^2 and $\nu = 0.2$, while an

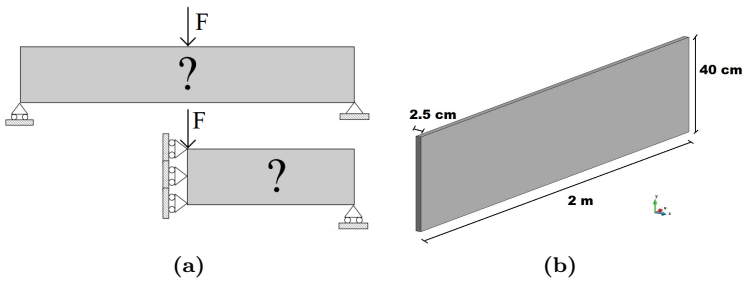

Figure 5.39. MBB scheme (a); "slice" model of the studied beam and geometrical dimensions (b).

hexaedral element type is chosen for the mesh discretization thanks to the regularity of the geometry. The input conditions are reported in Table 5.8.

E_{min}	Rel tol	Max $n°$ it	r_{filter}	$size_{elem}$	V fraction
?	1e-06	1000	0.03	0.008	0.3

Table 5.8. Input file parameters for the optimization analysis of the straight concrete beam.

As indicated by the question mark in Table 5.8, the choice of the E_{min} represents a critical point in the decision of the parameters for the analysis. In fact, preliminary results show that very low values of the E_{min} (as example the classical value E_{min}=1e-09 also adopted in Andreassen et al. [2011]) lead to the abort of the analysis or to numerical problems clearly visible by the output quality. Regarding this point, it is worth to notice that in literature normally dimensionless parameters are used as for the Yong modulus. In addiction, from the author knowledge, there are no papers or contributions explaining how to correctly tune such parameter when real material properties are assumed for the modeling. Thus, the first issue to be solved is to find the lowest value of E_{min} which allows to avoid numerical problems linked to a too small value of such parameter. For this reason, we test several values of the E_{min} in order to catch a good one proportioned to the chosen Young modulus E. In the following, most significant results corresponding to the E_{min} values of 0.01, 0.005, 0.0005 are compared. Figures 5.40 and 5.41 respectively illustrate the comparison of the plots of the Von Mises stress and the vertical displacement (y direction) for the analyzed E_{min} values.
Decreasing the E_{min} from 0.01 to 0.0005 there is a worsening in the quality of the images, thus numerical issues from the analysis point of view. When the ratio between the E and the E_{min} is too high, numerical singularities arose in the calculation leading to poor output as illustrated in Figure 5.40 (b) and 5.40 (c). The

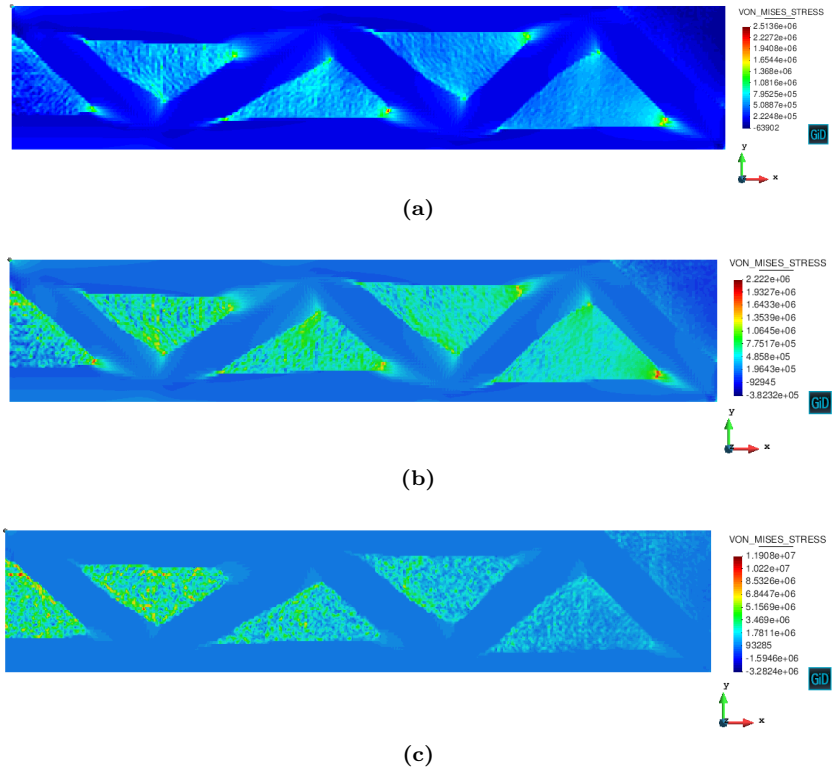

Figure 5.40. Contour plot of the Von Mises stress for E_{min} =0.01 (a), E_{min} =0.005 (b), E_{min} =0.0005 (c).

same behavior can be noticed looking at Figure 5.41 (c). According to these consideration, for the following analysis the adopted E_{min} is 0.005, considered enough accurate for the aim of the study. Nevertheless, a more deep research should be conducted on the matter.

By using the TopOpt application, we obtain an optimized geometry depicted in Figure 5.42 (a). Table 5.9 shows the output of the analysis that demonstrate that a fast solution can be reached even in the presence of a large hexaedral mesh, while greatly reducing the objective function value. Indeed, the final layout present a compliance which has decreased of about the 79 % respect to the starting one. After performing of the optimization step, the second one consists in extracting the generated geometry and to verify its results by testing the new design, and comparing it with the original configuration. Figure 5.42 (b) shows the results of the post-processing extraction of the optimized volume (for a threshold value = 0.3) and a subsequent extraction of the surface mesh through the TopOpt smoothness

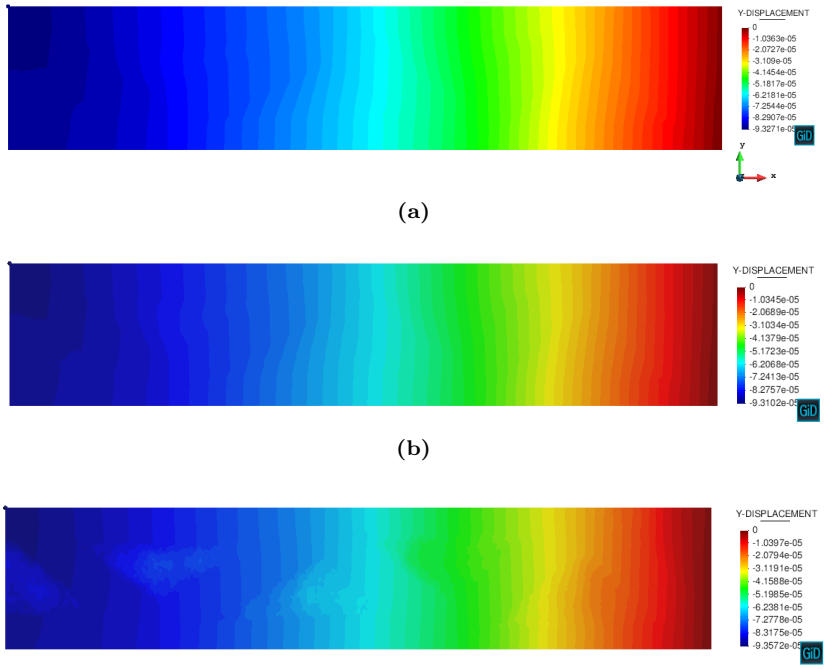

Figure 5.41. Contour plot of the vertical displacement (y direction) for E_{min} =0.01 (a), E_{min} =0.005 (b), E_{min} =0.0005 (c).

option.

Obj f	Abs Obj	$n°$ it	t_{step}	t_{tot}
0,005592	-79,24%	127	37.5s	2624s

Table 5.9. Output file parameters for the optimization analysis of the straight concrete beam.

From the final optimized extracted surface presented in Figure 5.42 (b), we can export an stl file with built-in functionalities. Since our goal is to study the post-processing potential and flexibility of the TopPot application, we chose a commercial software different from GiD to analyze and post-process the obtained stl file. In particular, to perform further solid mechanics simulation the Abaqus software is chosen. The first encountered issue is in the direct use of the produced stl file because of imperfections often contained in the file that make it not readable for the software. In such cases, we have to pass through additional tools to fix those

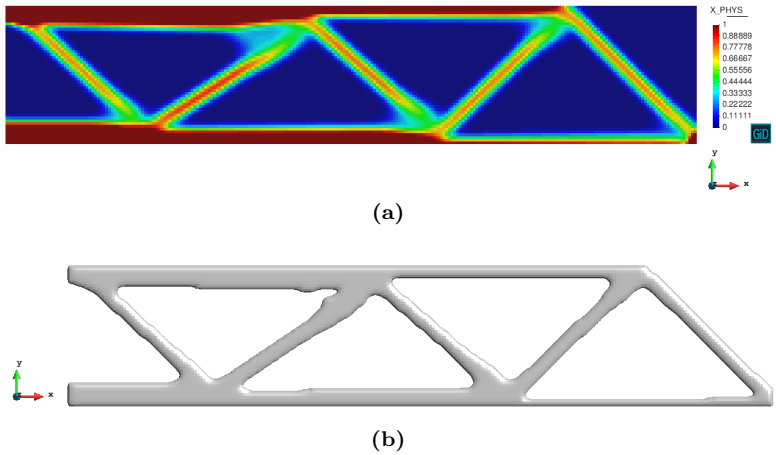

Figure 5.42. Contour plot of the density X_PHYS over the beam in the optimized configuration (a); extracted surface geometry considering a X_PHYS threshold value of 0.3 (b).

imperfections. Once the file is correctly imported and the 3D mesh created from the orphan 2D mesh, original load and boundary conditions are re-applied to the new geometry and a FE simulation is performed to calculate displacements and reactions. The result of the Abaqus modeling is reported in Figure 5.43. The picture also illustrates the practical difficulty in applying original boundary conditions and loads because of the new mesh smoothed curves. At this point, a numerical comparison can be performed between the optimized model after post-processing and the original non-optimized model. Figures 5.44 and 5.45 illustrate respectively the plots of the axial and shear stresses and the vertical displacement (y direction) for the optimized beam. In the plots, the stress are expressed in Pa and the displacement in mm, respectively.

Focusing on results reported in Figure 5.45, the vertical displacement measured for the optimized one is U_y= -0.08 mm, while for the initial geometry (Figure 5.39 (b)) is U_y= -0.04 mm. Even if the final displacement is twice the starting one, it should be noted that the structure is significantly lighter and the volume is reduced of the 70%. In fact, the starting volume constraint (0.3) is satisfied also after the volume extraction process. To this regard, it is possible to recover different final post-processed topologies starting from the same X_PHYS distribution but varying the threshold value for the volume extraction. This parametric study can be useful to evaluate the influence of such parameter in the final stiffness of the beam. An "equivalent stiffness" for the post-processed optimized beam can be estimated starting from the FE displacement and exploiting the analytic formula available for conventional static problems. The obtained approximated formula is:

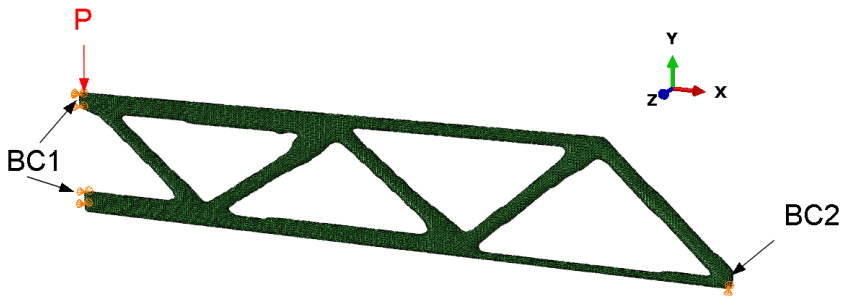

Figure 5.43. Abaqus model of the 3D optimized beam obtained from the *stl* file.

$$EJ_{eq} = \frac{F \cdot L^3}{48 \cdot U_y} \tag{5.16}$$

where F is the applied vertical load, L the length of the beam and U_y the vertical displacement calculated through the Abaqus FE analysis. Varying the threshold value for the volume extraction and applying equation (5.16) for each extracted geometries it is possible to extent the variation of the overall stiffness. Figure 5.46 depicts the extracted geometries considering different values (from 0.3 to 0.7) for the X_PHYS threshold; Figure 5.47 illustrates the trend of the "equivalent" stiffness varying the X_PHYS threshold value. In the plot, the EJ_{eq} stiffness is normalized respect to the same quantity calculated for the full solid beam of Figure 5.39 and a displacement U_y= -0.04 mm. Table 5.10 reports the maximum values of the axial and shear stress, and the vertical displacement measured for each extracted geometries of Figure 5.46.

	V_{frac} =30%	V_{frac}=40%	V_{frac}=50%	V_{frac}=60%	V_{frac}=70%
max σ_{11} [Mpa]	0.42	0.36	0.35	0.31	0.31
max σ_{12} [Mpa]	0.44	0.32	0.71	0.44	0.26
max U_y [mm]	0.0825	0.073	0.056	0.0498	0.0482

Table 5.10. Maximum values of the axial and shear stress, and the vertical displacement measured for each extracted geometries.

Looking at Figure 5.47 it can be noticed that, as expected, the stiffness of the optimized beam growths with the increase of the volume fraction but with a non-linear trend. The slope of the curve, in fact, is significantly different between the 30-40 % and 40-50 % steps. This aspect is particularly interesting and it

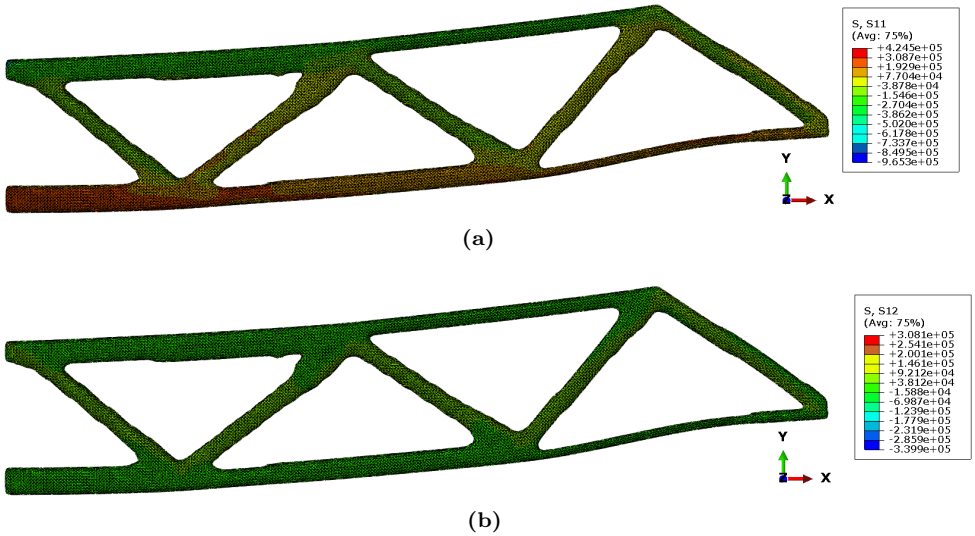

Figure 5.44. Contour plot of the axial stress (a) and the shear stress (b) for the 3D optimized beam.

demonstrates that in compliance minimization problem the choice of the volume constraint is not trivial and strongly influences the stiffness behavior.

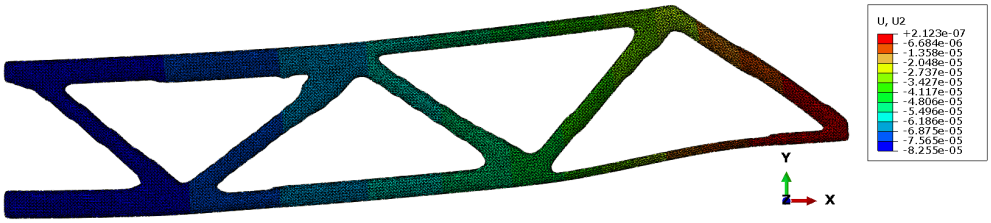

Figure 5.45. Contour plot of the vertical displacement (y direction) for the 3D optimized beam.

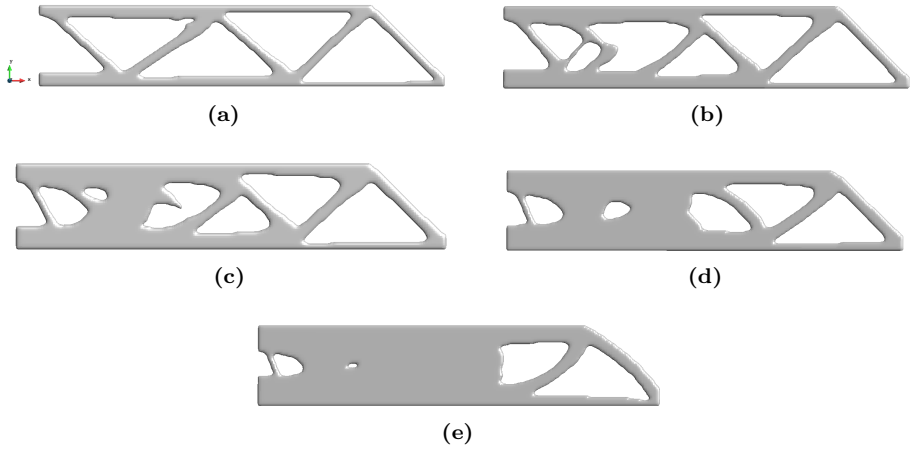

Figure 5.46. Extracted geometries considering a X_PHYS threshold value of 0.3 (a), 0.4 (b), 0.5 (c), 0.6 (d) and 0.7 (e).

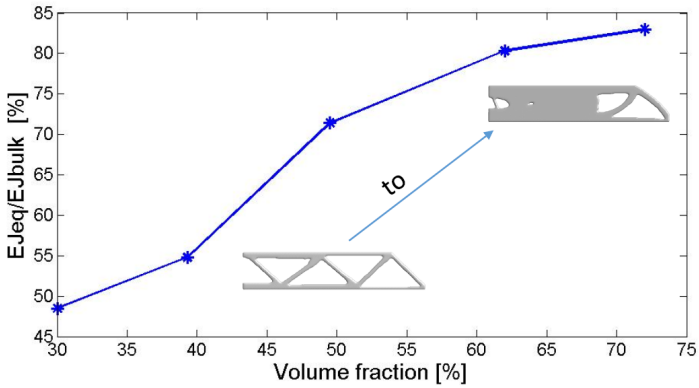

Figure 5.47. Evaluation of the normalized "equivalent" stiffness trend varying the final volume fraction.

Curved shape concrete beam

As second example, the object chosen for the optimization is the curved 3D printed beam introduced in Section 4.2.5. The model configuration is shown in Figure 5.48 (a). As for the straight beam case we decide to model the beam in terms of "slice" to respect the constraint of the cross-section in the z-direction. Parameters for the concrete material and the value for the concentrated load are the same adopted for the first example. As illustrated in Figure 5.48 (a) the concentrated load is applied at about the half of the beam. Due to the complexity of the geometry, in this case, a tetrahedral element type is chosen for the mesh discretization. The input conditions are reported in Table 5.11.

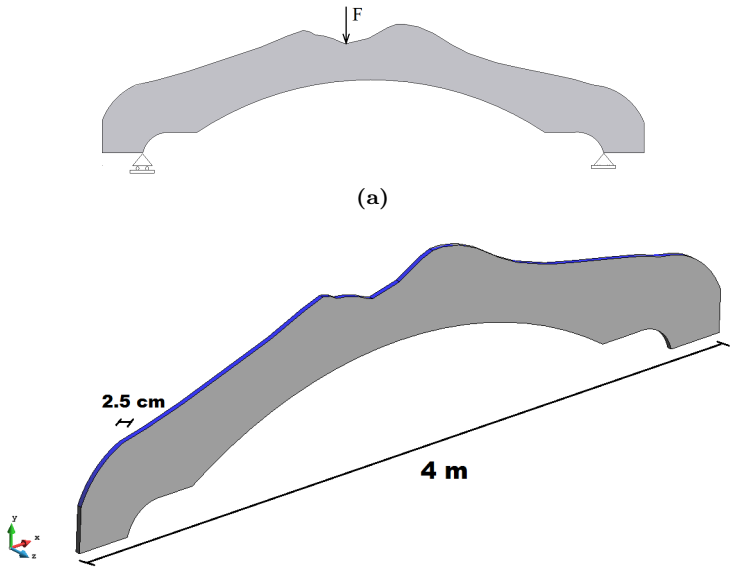

Figure 5.48. Curved shape beam (a); "slice" model of the studied beam and geometrical dimensions (b).

E_{min}	Rel tol	Max $n°$ it	r_{filter}	$size_{elem}$	V fraction
0.005 MPa	1e-06	1000	0.03	0.01	0.4

Table 5.11. Input file parameters for the optimization analysis of the curved shape concrete beam.

From the first steps of the design process performed by using GiD and the TopOpt

application, it is possible to recover the contour plot of the Von Mises stress field and the vertical displacement (see Figure 5.49), and the X_PHYS distribution over the domain (see Figure 5.50 (a)).

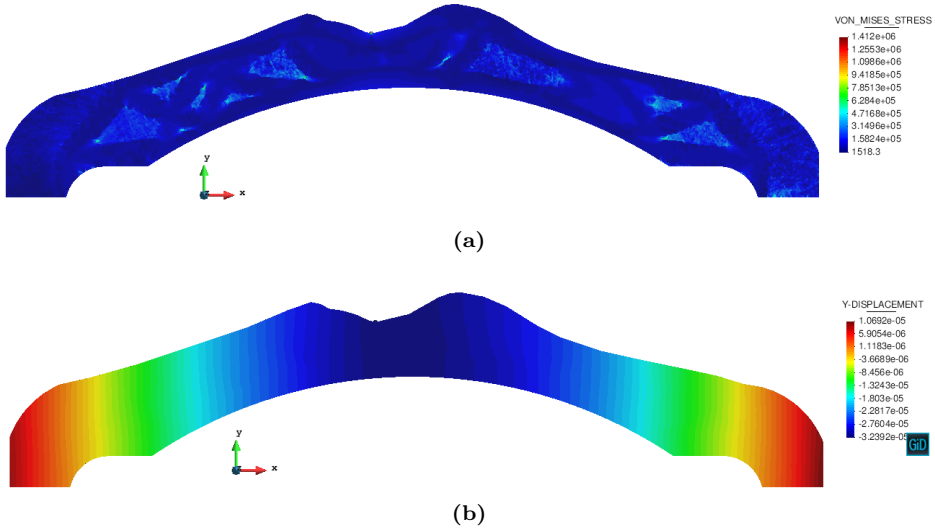

Figure 5.49. Contour plot of the Von Mises stress (a) and of the vertical displacement (b).

Table 5.12 shows the output of the analysis. Due to the complexity of the shape and the greater number of mesh elements, this optimization process takes around 5 hours to be completed using a standard portable computer. Nevertheless, it is an acceptable computational time if we think about the coupling of FE and optimization analysis at the same time. The final layout present a compliance which has decreased of about 39 % respect to the starting one. In this case, the final model gains less in terms of flexibility since the starting constraint on the volume is set to 0.4. As for the first example, we can extract the geometry from the density distribution. Figure 5.50 (b) shows the results of the post-processing extraction of the optimized volume using a threshold = 0.3 and a subsequent extraction of the mesh surface through the TopOpt smoothness option. Looking at the contour plot of the density variable it is interesting to see how it is distributed in the central part of the beam, where the concentrated load is localized. In this portion of the beam, the top chord and the bottom chord are thicker and well defined. Recalling the proposed 3D printing approach (Chapter 4) this kind of information is particularly useful in the defining, as example, the thickness to be used for the concrete segments. Considering the 3D printed curved beam (see Section 6.1) a better assembly configuration would have the central concrete segments with truss

and diagonals thicker respect the to external segments. Furthermore, the extracted geometry illustrated in Figure 5.50 (b) provides a clear definition of the areas of the beam which should be void.

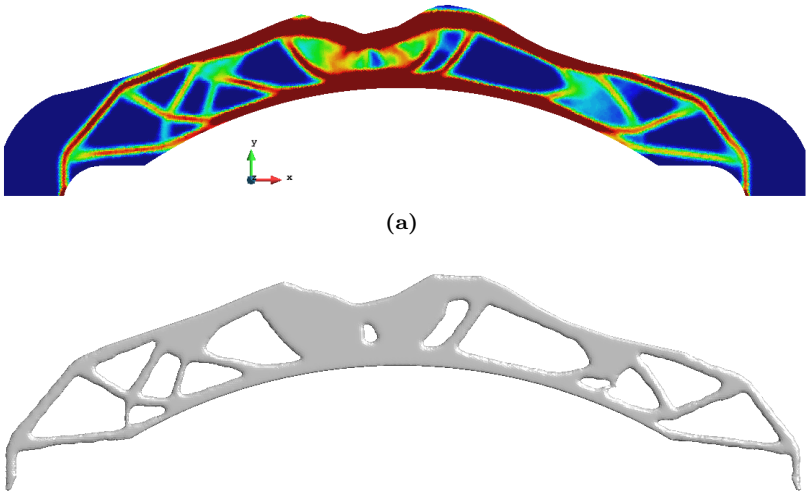

(a)

(b)

Figure 5.50. Contour plot of the density X_PHYS over the curved beam in the optimized configuration (a); extracted geometry considering a X_PHYS threshold value of 0.4 (b).

Obj f	Abs Obj	n° it	t_{step}	t_{tot}
0,0001941	-38,78%	155	85s	15478s

Table 5.12. Output file parameters for the optimization analysis of the curved concrete beam.

5.5 Conclusive considerations

Two topology optimization strategies are evaluated on realistic design problems for AM of concrete. The PSTOpt algorithm tries to solve stress-constrained optimization problems and to model in a proper way the material behavior of the concrete. The TopOpt Kratos application, instead, allows to cover most of the design process steps, from the starting domain to post-processing analysis. In the following, conclusive comments related both to the PSTOpt algorithm and to the TopOpt Kratos application are reported.

PSTOpt algorithm

The PSTOpt is a very intuitive procedure able to solve volume minimization problem, exploiting an innovative constraint on principal stresses. This key feature of the code allows to control the stresses in concrete optimization problems since catches the different behavior in tension and in compression of the material. Particularly, through the introduction of the risk factors it is possible to control asymmetrically the stresses both in case of compression (bound on the minimum value) and traction (bound on the maximum value). Preliminary results show that when accurate meshes are adopted, the obtained topologies closely recall the optimal grid-like continua studied by Michell [1904]. A *singularity check option* is also included in the code to avoid stress singularities. Analysis output show the positive effect of such strategy in the optimization, especially when large mesh are used, thus stress disturbances are more evident. Furthermore, for each analyzed case, it is possible to notice that the *singularity check option* is driven by the stress traction limit due to the fragile behavior of the concrete.

Even if the method proves to be useful for research purposes due to its flexibility and simplicity, there are several issues that should be solved. In spite of the filtering procedure, the problem of mesh dependency appears to be not completely overcome. The simplicity of the stopping and mass distribution criteria suggests the need of future research on such aspects, being fundamental within an optimization process. Further investigations should be made also on the solution of the stress singularity issue.

Kratos TopOpt application

The TopOpt Kratos application is a tool written in C++ and Python and is useful and efficient to optimize the material distribution inside an arbitrary 3D domain. The application allows compliance minimization while preserving a defined volume fraction. The main feature of this application is the possibility to pre- and post-process the domain analyzed in the optimization problem. In particular, it allows to extract smooth geometries from the optimized topologies and return and stl file which can be easily used in software for remeshing or further FE analysis.

Preliminary results on realistic concrete cases have demonstrated the capabilities of the software in handling complex 3D problems, obtaining stiffer structures in acceptable computational times. Furthermore, interesting observations can be recovered from the optimized topologies, useful in the design process of the concrete segments. The main drawback which can be identified in the TopOpt application is that it only tackles compliance minimization problems. As already said, the solution of stress-constrained problems is more interesting from a design point of views since it allows the control on the stress field. In compliance problems, this is possible only in a post-process phase and can require several additional analysis. Interesting work for the future should include this option to the application capa-

bilities. Moreover, a further improvement could be the combination of topology and shape optimization in the code. This will lead to the realization of a complete design process subjected to realistic constraints in volume or stresses, and post-processing steps necessary for the manufacturing application.

6 3D printing of RC elements: test cases

The present Chapter concludes the work about 3D printing of RC members by illustrating the two principal full-scale tests conducted at the laboratory of Naples and introduced in Section 4.2.5.

As a demonstration of the potentialities of this approach, Section 6.1 opens with the evaluation of the response of the variable cross-section curved RC beam. Then, Section 6.2 presents the straight RC beam together with the results of the full-scale three-point bending test performed on it. Finally, main issues and opportunities of this innovative production route are discussed in Section 6.3.

6.1 Curved shape 3D printed RC beam

To characterize the behavior of the curved 3D printed beam in terms of deformability and strength numerical simulations have been conducted. Here in the following, results obtained from linear and non-linear analysis are reported and commented. Currently, the experimental assessment of the mechanical properties of such a beam is out of the scope of this work and will be considered in future works by the authors.

6.1.1 Numerical modeling

In order to characterize the behavior of the printed object in terms of deformability and strength, a 3D finite element model is implemented using the Abaqus software. The concrete parts are modeled with 8-node linear brick, reduced integration, hourglass control elements while the steel bars with 2-node linear beam elements. Here different configurations considered in the numerical simulations are presented, varying some significant parameters, including: concrete material constitutive models, boundary conditions and interaction constraints. In particular, FE simulations are conducted considering both a linear and a non-linear constitutive behavior for the concrete. In the case of linear analysis, we adopted a Young modulus respectively equal to 30 GPa and 210 GPa, and a Poisson' s ratio equal to 0.2 and 0.3 for the concrete and the steel. While, in defining the non-linear constitutive behavior of the concrete we implement the Mander et al. [1988] constitutive model for confined concrete. In order to take into account different possible

configurations, both for linear and non-linear analysis, we considered two different boundary conditions and two different interaction constraints among the surfaces of each consecutive printed concrete segment. In particular, we considered either simply supported and clamped boundary conditions applied at the edges of the first ant last concrete segment, in order to simulate possible anchoring solutions to the ground and look at the effects on the printed beam. Concerning the surface interaction properties, we considered respectively: (i) the tie interaction condition, which allows making the translational and rotational motion as well as all other active degrees of freedom equal for a pair of surfaces; (ii) the general contact condition (including penalty for tangential and hard contact for normal behavior).

Regarding the loading condition, for the set of linear analyses we simply considered the dead load of the beam applied as a distributed gravity load. While for the non-linear cases, we carried out displacement-controlled analyses in order to investigate the behavior of the beam under strength limit conditions combined with gravity load case. In details, a vertical displacement was applied at the mid-span of the beam through a reference point con-strained to the mid cross-section surface. For the purpose of the investigation, three values of vertical displacement were considered: 1, 2 and 3 mm. Moreover, the displacement was not applied instantaneously but through a linear increasing function.

6.1.2 Numerical results

In the following, only the most significant results are reported along with a schematic interpretation of the results. In particular, we report only the results of the linear and non-linear analyses referred to only the simply supported boundary condition case since this represents the real configuration of the installed 3D printed beam. Furthermore, concerning the surface interaction constraint, the more interesting results are those obtained from the tie interaction condition since they better represent the real interaction among the printed concrete segments. In fact, the assembly phase foresees the insertion of mortar material between two consecutive printed concrete segments in order to guarantee continuity among the elements. Tables 6.3 and 6.2 show the simulation results obtained from linear and non-linear analyses, respectively. Each table reports the maximum vertical displacement achieved at the mid-span of the printed beam and maximum tensile stress in concrete and steel rebars.

Interaction constraint	$U_{max}vertical$ [mm]	σ_{max} [+] rebar [MPa]	σ_{max} [+] concrete [MPa]
Tie	-0.15	3.63	0.69
Contact	-0,41	11.80	1.35

Table 6.1. Linear analysis results for tie and contact surface interaction constraints.

Interaction constraint	$U_{max}vertical$ [mm]	σ_{max} [+] rebar [MPa]	σ_{max} [+] concrete [MPa]
Tie	-2.00	87.79	3.04
Contact	-2.00	64.47	2.95

Table 6.2. Non-linear analysis results for tie and contact surface interaction constraints.

As shown in the tables, under the hypotheses of linear elastic material and only gravity load case, the order of magnitude of tensile stresses do not exceed the strength limit values, particularly from the concrete side. Table 6.2 summarizes only the results coming from a single displacement controlled case (U = 2.00 mm) since sufficient to derive conclusions in the following. Indeed, in the controlled displacement analyses, the tensile stresses of concrete are very close to the threshold tensile strength values. Regarding the steel reinforcement rebars, it can be seen that the tensile stresses do not exceed 391 MPa, which is the elastic limit. Another aspect that should be noticed is the distribution of stresses over the concrete elements. In the models with tie interaction constraint (between adjacent concrete segment surfaces), the tensile stresses are spread in the lower side of the beam (Figure 6.1), while in the models with a contact interaction constraint they are more concentrated on the central concrete segment (Figure 6.2). On the basis of the previous observations, it appears that the tensile stresses in concrete can be a limiting factor in the design of such concrete segments. On this point, the introduction of reliable optimization algorithms to obtain a real optimized structure appears to be fundamental. A correct reshape of the concrete segments has to be performed to guarantee, at the same time, the maximum material removal and strength and stiffness characteristics of the beam.

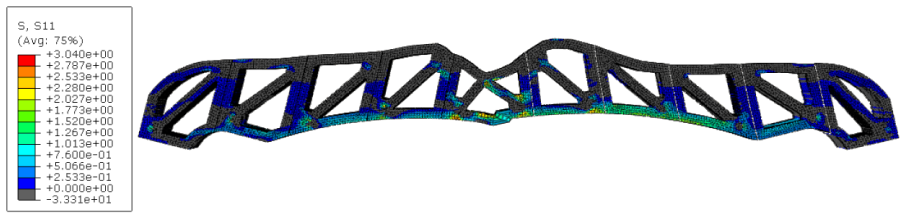

Figure 6.1. Contour plot of the concrete tensile stress distribution for the tie interaction constraint case.

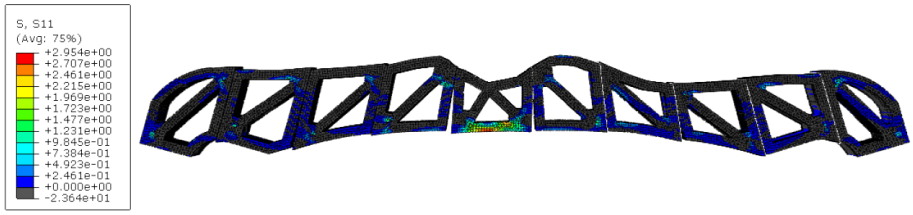

Figure 6.2. Contour plot of the concrete tensile stress distribution for the contact interaction constraint case.

6.2 Straight 3D printed RC beam

To evaluate the flexural behavior and failure mechanisms of the straight 3D printed RC beam manufactured with the proposed approach, both an experimental test and numerical analysis are performed. In the present Section, we illustrate the experimental set-up and results for the three-point bending test conducted on the RC straight beam and the corresponding 2D numerical model built with the software SAP2000.

6.2.1 Experimental set-up

The straight 3D printed RC beam is considered as specimen for a three points-bending test. The test is carried out by means of a universal servo-hydraulic testing machine with 500 kN force capacity while, the load scheme is set to ensure that the primary failure comes from tensile or compression stress. This is done by minimizing the shear stresses arising from the test thus by controlling the shear span to depth ratio [EN1992-1-1, 2004], i.e., the length of the outer span divided by the height (depth) of the specimen (see Figure 6.3).

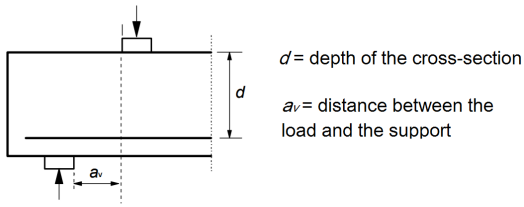

Figure 6.3. Beam with direct supports: shear to span depth ratio (a_vd [EN1992-1-1, 2004]).

The test is conducted under displacement control with a velocity of 0.5 mm/min. Strain measurements on the steel components of the beam are achieved through fourteen (seven for each side of the beam) strain gages placed at half-length of

each threaded rod, as illustrated in Figure 6.4. For the strain measurements of compressed concrete, nine strain gages are installed only in the backside of the beam (see Side B of Figure 6.4). The backside of the beam is made smooth on purpose in order to ensure the grip between the concrete surface and the strain gages. To measure the displacement at the mid-span of the beam, two linear variable differential transducers (LVDTs) are placed at the bottom edge in correspondence of the half of the beam. The load-displacement curve is obtained digitally as the test proceeded, while, at the same time, the strain-displacement curves for all the strain gages applied on the bars and on the concrete chords are recorded. Figure 6.5 shows the instrumented specimen arranged for the three-points bending test.

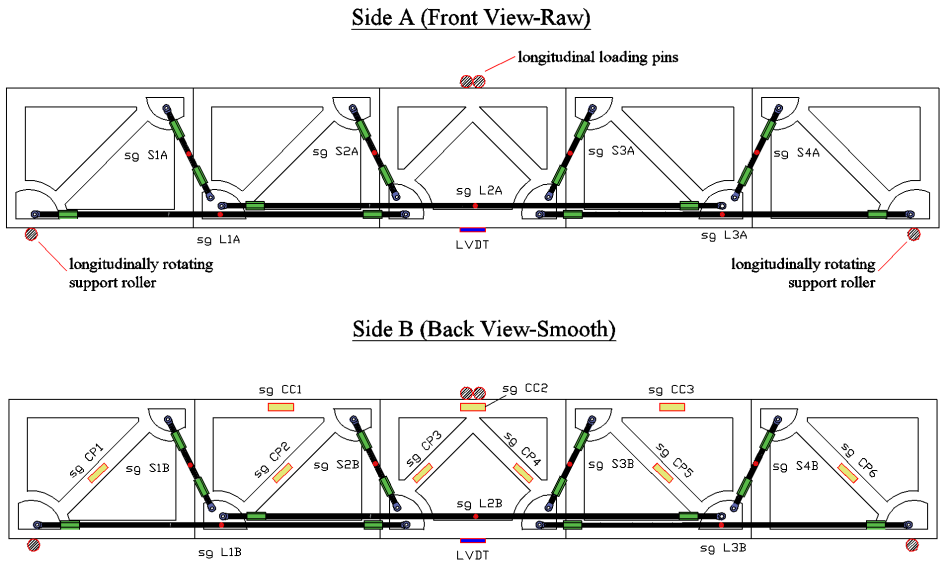

Figure 6.4. Front view and back view: positioning of the strain gages for the measurements of load on bars (red points) and on the concrete chords (yellow rectangles) and of the LVDT (blue rectangle) for the measurement of displacements at the beam mid-span.

6.2.2 Numerical modeling

A FE model of the straight 3D printed RC beam is also built up in order to interpret the experimental results presented in the next section. To reduce computational costs, a simplified 2D model is built with the software SAP2000 [Inc., 2009], choosing 1D-frame elements for the discretization of the beam system (see Figure 6.6). The black points represent the nodes defining the elements, thus, the model discretization. The beam is modeled considering only half of the geometry, applying

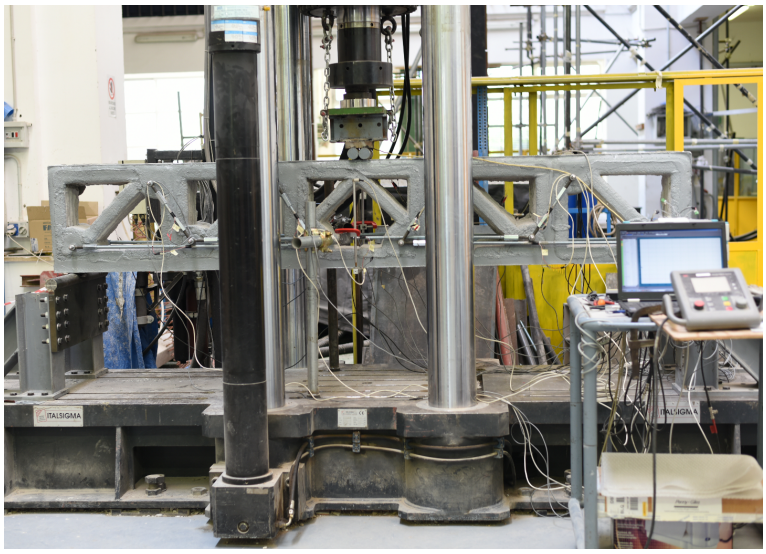

Figure 6.5. Equipped specimen for the three points bending test.

and ideal symmetric cutting plane (X-Y) at half width of the beam (Z direction). In this way, it is possible to build a 2D model and consider only one side of the beam thanks to the symmetry of the rods system. Such a simplified modeling can be considered enough accurate also because the actual beam is nearly a strut and tie system, consisting of diagonal compression concrete struts and opposite diagonal tension steel ties. Furthermore, to model the interface connection between the surfaces of two adjacent segments, we define another set of frame elements with suitable elastic properties, called *link* elements and numbered in Figure 6.6. We also introduce the notation B_el_i, j to identify the generic frame element of the concrete bottom side, where i indicates the concrete segment to which it belongs (as an example, i=1 identifies the first concrete segment starting from left of Figure 6.6) and j indicates the number of the element enumerated with increasing order from left to right. A CAD software is used to draw the actual beam geometry (once printed) and then imported in SAP2000. At this stage, we define cross-sections and correspondent properties to be assigned to the frame elements. Frame properties are chosen in accordance with the real dimensions measured on the beam (for the concrete segments) and the diameters adopted for the threaded rods.

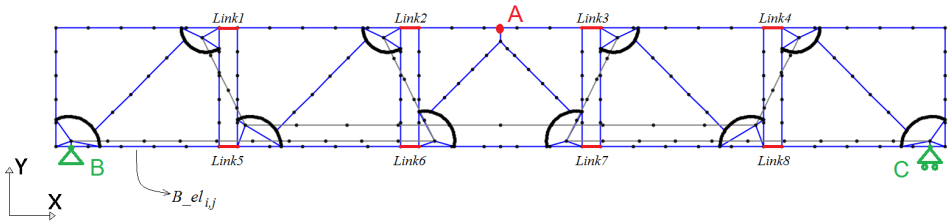

Figure 6.6. FE model details and boundary conditions for the straight RC beam. The link elements are introduced to model the interfaces between adjacent concrete segments. B_el_i, j notation refers to finite elements of the concrete bottom chord, where i indicates the concrete segment (from 1 to 5) and j indicates the number of the element enumerated with increasing order from left to right.

The following boundary conditions are applied to the 2D beam model (see Figure 6.6):

1. Out-of-plane displacements constrained at each node of the mesh (UZ = 0);
2. All displacements and rotations around X and Y constrained (UX=UY=UZ=RX=RY=0) at point B;
3. Out-of-plane and vertical displacements and rotations around X and Y constrained (UY=UZ=RX=RY=0) at point C;
4. Concentrated load applied at point A;
5. Gravity load in the vertical (Y) direction applied at each node of the mesh.

Material properties are defined as in Table 6.3 for concrete and steel. The numerical simulations are carried out according to the actual experimental evolution of the above-described three-points bending test, in order to achieve a satisfactory correspondence with the test results. Specifically, in such a simplified analysis, the finite element model configuration is modified in accordance with the development of the cracking process, by removing one or more link elements and frame elements which do not react anymore to traction, or degrading material properties of the link themselves. For all the resulting models, a linear static analysis has been performed. This choice comes from the fact that the beam system tested in this study does not exhibit a clear non-linear behavior from the material point of view, rather it depends on the assembly configuration under loading, as will be better demonstrated in the following. Comparisons between experimental, numerical and classical beam theory results are presented in order to validate numerical simulations as well as to obtain a better interpretation of the experimental test.

Concrete	Steel
E = 30000 MPa	E = 210000 MPa
$\nu = 0.2$	$\nu = 0.3$

Table 6.3. Material properties assigned to the frame sections.

6.2.3 Experimental results

In this section, the experimental outcomes obtained from the three-points bending test carried out on the straight 3D printed RC beam are analyzed. In terms of overall flexural behavior, it is possible to identify two main mechanical stages from the load-deflection curve reported in Figure 6.7: a *linear elastic stage*, in which the beam is intact (nor cracked or disassembled) and a *non-linear stage*, in which local/global cracks occur or interface failure takes place. The non-linear stage can be itself subdivided into: *start of cracking stage* (A-B curve) and *progression of cracking stage* (B-C curve) until the final *failure stage* (curve from point C on) corresponding to the complete loss of load carrying capacity of the beam.

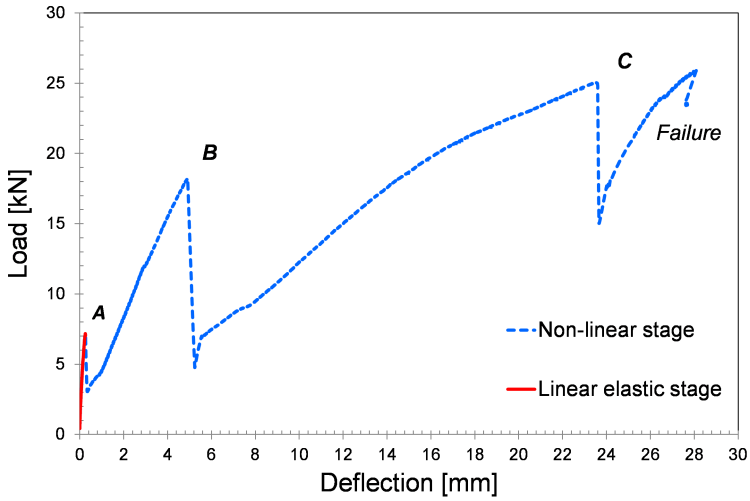

Figure 6.7. Linear elastic and non-linear stages of the load-deflection curve from experimental data.

To facilitate the understanding of the cracking/failure mechanisms developed by such system, Figure 6.8 shows the sequential order of crack creation and propagation along the beam.
The formation of the first tensile crack in the concrete corresponds to the point of

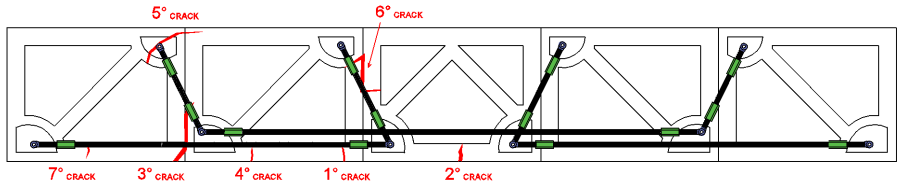

Figure 6.8. Linear elastic and non-linear stages of the load-deflection curve from experimental data.

transition from the linear elastic stage (in which the beam is intact) to the non-linear stage, as depicted in Figure 6.9 (a) and identified in the load-deflection curve of Figure 6.7 with Point A. This first brittle failure occurs at the bottom side of the concrete segment adjacent to the central one for a load level of approximately 7 kN. This transition corresponds to a moderate loss of carrying load capacity and is associated to the reduction of the tensile resistant cross-sectional area of the concrete segment undergoing cracking. After the transition from the linear to the non-linear stage, the load increases with an almost linear trend until the formation of the second major crack which is identified with the second peak in the force-displacement curve (point B) corresponding to an applied load of about 18 kN. Even if the flexural behavior is considered as non-linear between points A and B (*start of cracking stage*), the force vs deflection curve still maintains a linear slope as the first part of the curve. Indeed, the first two cracks at the concrete bottom side lead to an initial loss of stiffness but, at the same time, the beam system is still reacting as a monolithic element because the connection between the steel reinforcements and the concrete segments is preserved. Figure 6.9 (b) shows a detailed view of the second crack formation.

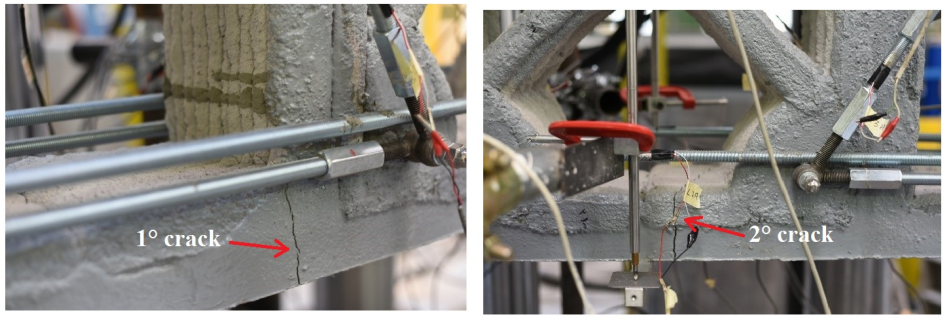

(a) **(b)**

Figure 6.9. 1° crack (a); 2° crack (b).

A different trend can be noticed in the shape of the force-displacement curve between points B and C, which identifies the occuring of the *progression of cracking stage*, exhibiting a non-linear behavior. Besides the growth of the existing cracks (1° and 2° cracks), in this stage it is possible to recognize the formation of three further major cracks (3°, 4° and 5° crack in Figure 6.10 (a)) localized between the first and the second concrete segment. During this loading stage, the three major cracks did not develop in a distinct or sequential manner, making not possible to clearly identify which one of them determines the third load peak (point C) and corresponding drop in the load-deflection curve. Furthermore, the mechanism of fracture developed in this stage increases in complexity, involving the bottom side of the first and second concrete segments (tensile cracks), the interface connection surface between the same concrete segments (interface opening and relative sliding), and the connection system between the steel reinforcement and the concrete (shear failure of the anchoring substrate made of concrete material). The final part of the curve (from point C until final failure) is representative of the *failure stage*. In detail, after reaching the ultimate load peak of approximately 25 kN, severe damages occur in correspondence of the connection system between the steel reinforcement and the concrete segment adjacent to the central one (see Figure 6.10 (b)). This circumstance led to the global failure of the beam.

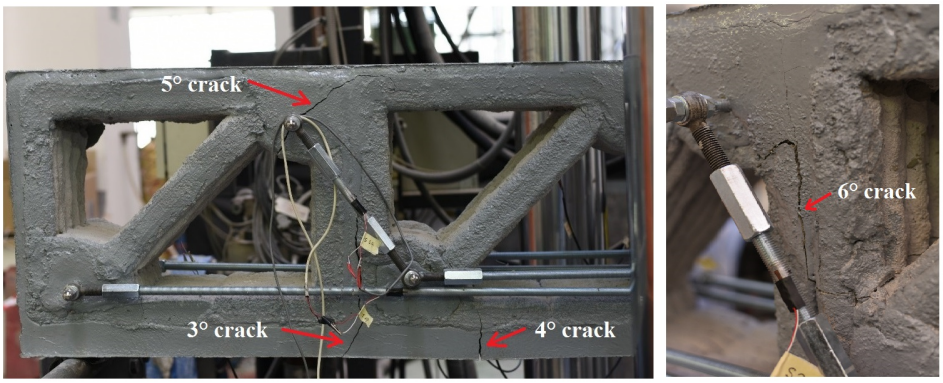

Figure 6.10. front view of the 3, 4 and 5 cracks (a); 6 crack (b).

Finally, it is worth making some considerations about the magnitude of the deflection at failure recorded in the flexural test. As shown in Figure 6.7, the maximum value of the vertical displacement is quite large if compared with that expected for an equivalent solid RC beam (with same cross-section dimensions), especially since the steel bars have not even reached the yielding limit. Nevertheless, looking at the linear elastic stage, the behavior of the 3D printed beam is

satisfactory, exhibiting an acceptable level of flexural deflection that is comparable with a non-cracked regime of a solid RC beam but associated with a significant weight reduction. On the contrary, for the non-linear stage, the loss of stiffness (and, consequently, the large deflections) derives mainly from the low effectiveness of the connection/interface system rather than from the reduction of the material properties or a wrong segment optimization strategy. For this stage, it would be worthy to draw a parallel with the displacements associated with the ductile region of an equivalent solid RC; however, due the different nature of the behaviors (connection system vs material ductility), this aspect deserves more attention and is currently under investigation by the authors.

From the strain measurements recorded during the flexural test, it has been noticed that the yielding limits in the steel rebars (i.e., approximately 0.18-0.20 %) are never attained upon ultimate beam failure. This is clearly observable in Figure 6.11 where we report the tensile strain-deflection curve recorded by the L2A and L2B strain gages (see Figure 6.4) which are applied to the threaded rods in correspondence of the mid-span of the beam, since they are the steel elements undergoing major tensile stresses. In addition, concrete material belonging to the upper compressed side of the printed segments does not experience any permanent failure given that the strain levels do not exceed non-linear limits (i.e., approximately 0.20%). Overall, the experimental outcomes revealed that the proposed

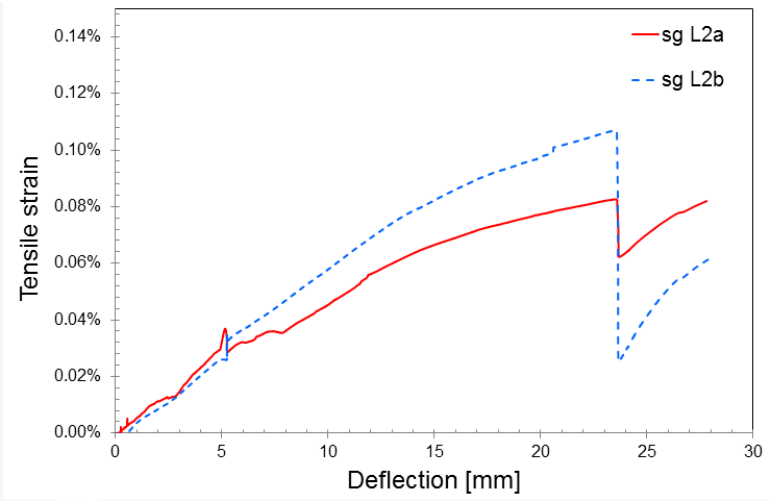

Figure 6.11. Tensile strain-deflection curve registered by the L2a and L2b strain gages applied on the steel bars.

RC beam system based on AM technology is prone to local damage phenomena occurring as flexural load increases. Besides moderate loss of stiffness related to

cracking of concrete under traction, the major limitation relies on the concrete segment assembly which can suffer from local failure mechanisms driven by shear forces arising at the interfaces between segments themselves. In addition, the low tensile strength of concrete material in correspondence of the upper anchorage of steel stirrups may play as a further brittle damage mechanism which triggers disconnections among components. Consequently, this characteristic behavior can be assumed as non-linear as a consequence of the above mentioned progressive failure mechanisms.

6.2.4 Numerical results

The results of the numerical analyses are presented in this section in order to better understand the failure mechanisms and the linear/non-linear stages observed in the experimental force- deflection curve. The analyses are also aimed at reproducing the characteristic stages of the flexural response of the beam observed during the progression of cracking formation. Three of four main stages identified during the experimental test (*linear elastic stage*, *start of cracking stage* and *progression of cracking stage*) correspond to three different FE models constructed by modifying the model configuration described in Section 6.2.2 (i.e. changing frame element and the connection properties among segments).

Starting from the *linear elastic stage*, Figure 6.12 shows the experimental load-deflection curve (blue line) measured at the mid-span of the beam compared with that obtained from the numerical simulation (named as Numerical 3D Printed_Stage1 curve, red line). In this case, the FE model of the beam comprises all the frame and link elements showed in Figure 6.6 having the standard material properties of Table 6.3. The curves corresponding to a full solid RC beam with the same overall cross-section dimensions of the printed RC beam are included in the graph of Figure 6.12, considering the non-cracked (black dotted line) and the cracked (green dotted line) configuration, i.e., for the latter case, corresponding to the actual RC beam cross section after first cracking. Furthermore, the curve related to a beam with same volume and ratio of the depth over the height is also added to the graph. In terms of overall flexural stiffness, the FE model (Numerical 3D Printed_Stage1 curve) reproduces satisfactorily the experimental force-deflection curve in the elastic range. In addition, even if the resulting flexural stiffness is quite lower than an equivalent full solid RC beam, it is still comparable to the behaviour of an equivalent beam with the same volume (Equivalent Beam_Volume curve). Thus, in this initial stage, the 3D printed beam investigated behaves as a simply supported beam (with a full cross-section and the same amount of material) under a concentrated load. Considering the curves related to the beam with equivalent overall cross-section dimensions, the 3D printed beam shows an intermediate behavior between that of the Equivalent Solid Beam and the Equivalent Cracked beam. This consideration is totally in line with the one made in section 3.1, about the beam deformability and the values of the vertical displacement registered during the test.

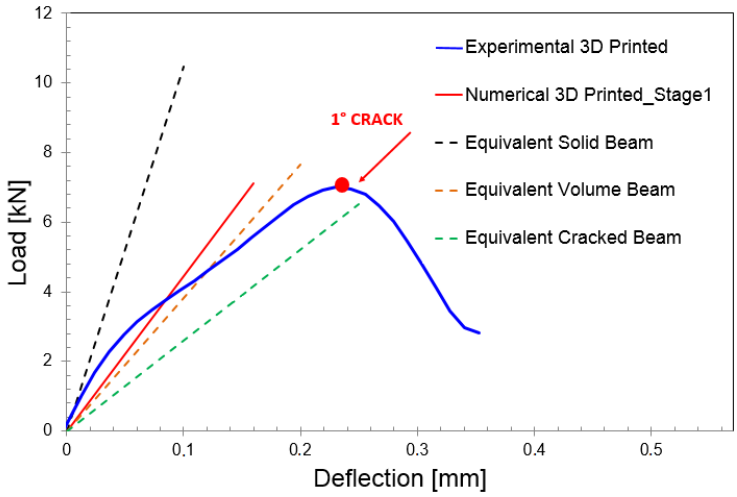

Figure 6.12. Linear elastic stage: load-deflection curves from experimental data and simulations.

The second main stage of the force-displacement curve, noticeable from the three points bending test, corresponds to the non-linear response of the beam system. Figure 6.13 reports the overall load-deflection curve recorded during the test and the overlapped curves obtained from the FE numerical simulations. Before going into the details of numerical-experimental comparison, it is worth to point out that some adjustments are made to the initial FE model on the basis of the experimental evidence of crack progression observed in the stages A-B and B-C of Figure 6.13. In detail, the Numerical 3D Printed_Stage2 curve of Figure 6.13 is obtained by removing Link6, and the elements involved by the cracks (see Figure 6.6) from the initial FE model (named as Numerical 3D Printed_Stage1). Those elements are considered mechanically not reacting in the A-B stage on account of the fact that 1° and 2° cracks occurred in the 3D printed beam (see Figure 6.8) at point A of the force vs deflection curve. Starting from this adjusted FE model, the Numerical 3D Printed_Stage3 curve is obtained by further removing Link5 and the elements involved by the new cracks (see Figure 6.6), in particular, the 3°-5° cracks (see Figure 6.8) at point B of stage B-C. As consequence of the crack pattern, also the material properties assigned to the link elements correspondent to the interface area subjected to the cracking phenomena are properly degraded.

Focusing on the *start of cracking stage*, as already underlined in Section 6.2.3, the behavior becomes globally non-linear due to the force drops in the experimental force-deflection curve; however, the curve between points A and B still maintains a linear slope which matches well with the numerical model (Numerical 3D Printed_Stage2).

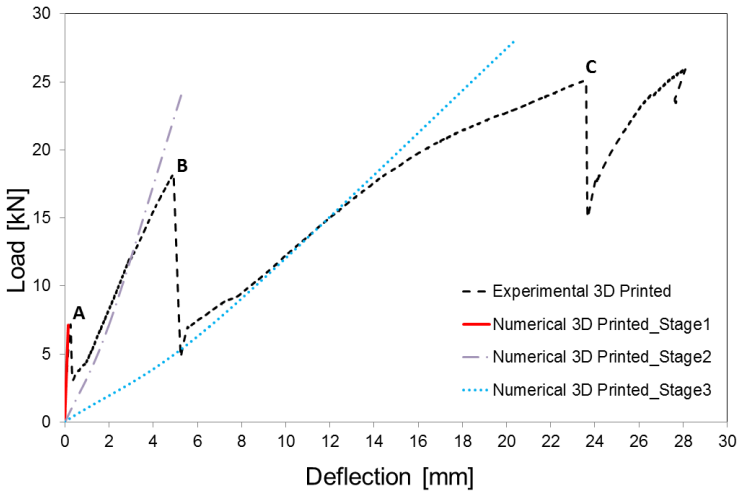

Figure 6.13. Load-deflection curves from experimental data and simulations.

Looking at the experimental curve between points B and C, corresponding to the *progression of cracking stage*, the numerical curve (Numerical 3D Printed_Stage3) matches quite well the experimental one until a load value of around 15 kN; afterwards, the numerical curve slightly diverges from the experimental one. The worsening in the response prediction through the numerical model can be explained analyzing the evolution of the cracking process. The local effects induced by the new crack mechanism lead to an emphasized non-linear trend in the experimental data not captured by the simplified numerical model. Indeed, the formation of the 3°-5° cracks is the result of the tensile failure of the concrete at the bottom side of the beam, the sliding at the interface surface between adjacent concrete segments, and the shear failure of the steel anchoring system.

Figure 6.14 reports the contour plot of the axial stress component obtained from the numerical analysis. Figure 6.14 (a) shows the level of stresses (both in traction and compression) correspondent to the Numerical 3D Printed_Stage1. Here, the top concrete chord is under compression while the bottom chord of the beam is in traction as expected, with the axial stress of the order of approximately 1 MPa, close to the cracking limit for concrete under traction. The reinforcement rebar system is also subjected to traction even if the values registered are very low. The FE simulation also highlights how the 3D printed beam systems behaves as a strut-tie ideal model, consisting of concrete compression members (i.e., struts) and steel tension members (i.e., ties).

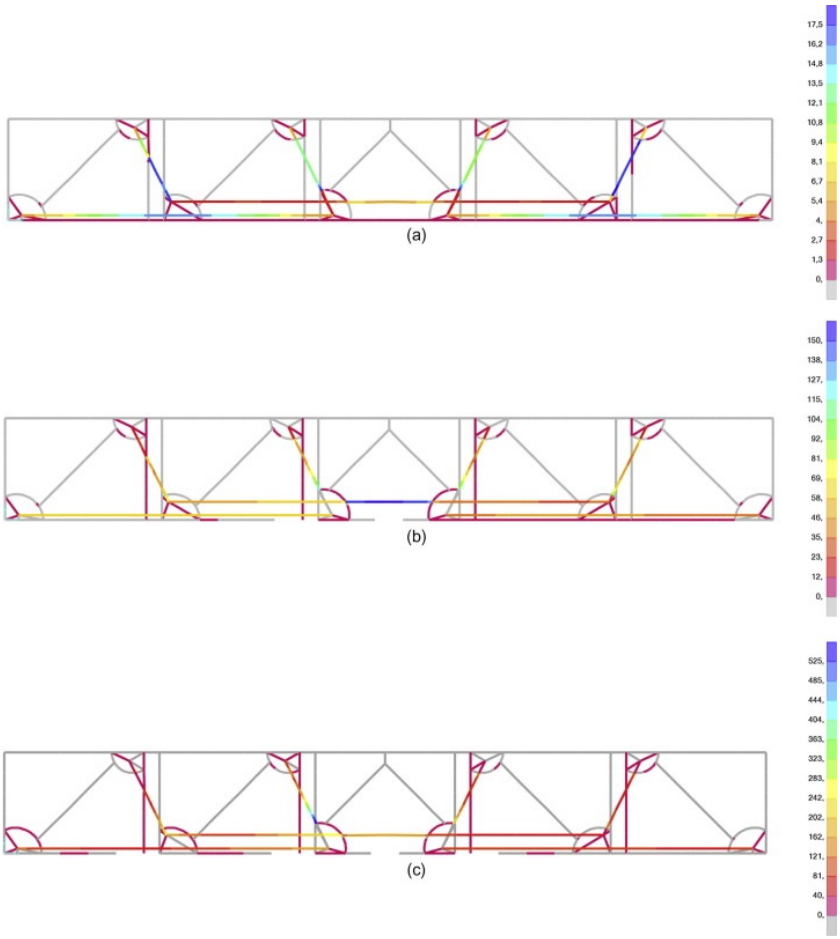

Figure 6.14. Contour plot of the axial stress σ_{11} component obtained from: Numerical 3D Printed_Stage1 (a), Numerical 3D Printed_Stage2 (b) and Numerical 3D Printed_Stage3 (c).

Figure 6.14 (b) shows the level of stress correspondent to the Numerical 3D Printed_Stage2, where the first cracks come into play. Here, all the steel rebars of the reinforcement system remain loaded, it is possible to notice some concrete elements undergoing traction stresses at the anchoring sites of the transverse steel reinforcement. The traction in the upper part of the beam is related to the development of the failure mechanism localized between concrete segment 2 and 3; in any cases, the stress level in those elements correspond to values around 0.5 MPa. Furthermore, as the concrete links are removed following first cracking, the traction stresses in the bottom chord are redistributed among the other segments. The plot in Fig-

ure 6.14 (c) refers to the to the Numerical 3D Printed_Stage3 and to a vertical concentrated force of 27 kN which almost corresponds to the beam failure load level. At this stage, mostly all the bottom concrete elements are not subjected to traction stresses due to the stress redistribution after progressive cracking. The stress concentration between concrete segment 2 and 3 is particularly reflected in the steel reinforcement response, in correspondence of which the rebars are the more stressed ones (even if never reaching the yielding limit, in accordance with the strain-deflection curve recorded by the strain-gages, see Figure 6.11). The local damage mechanism also determines a stress concentration in the steel stirrup connection system between the 2° and the 3° concrete segment (approximately 450 MPa). All the diagonal concrete struts are in compression as expected. Going back to Figure 6.13, the final part of the curve (from point C until the failure) describes the *failure stage*. The prediction given by the simplified numerical model is considered useless for this portion of the curve, due to the considerations linked to the complexity of the failure mechanisms at this stage of the test.

6.3 Conclusive considerations

In the following, conclusive comments are reported about the overall 3D printing strategy with a particular focus on the aspects arose from the examples treated in Chapter 6. It is worth to emphasize that the main purpose of this part of the thesis is to describe the basic idea of a novel rational use of AM in structural engineering, trying to underline difficulties but also opportunities coming from this technology. Indeed, numerous structural complications need to be dealt with and several critical issues have to be solved before this kind of elements can be usefully adopted in practice. However, numerous opportunities and advantages can be envisaged. Thus, more investigations are necessary for each step of the manufacturing process and obtained results confirm that this approach deserves to be further developed and extended to innovative practical cases.

The following list of issues and opportunities highlights the open questions but also the most promising features of the proposed AM approach.

Main issues

- The overall strength of the members can be limited by local failure mechanisms, e.g., inefficiency of the connection system, instability of the strut elements, and bar anchorage failure.
- The overall deflections can be large due to local deformations limiting the overall performances of the elements.
- The overall ductility has to be checked since capacity of the concrete elements to support the plastic deformations of the steel bars needs to be proved.

- The mechanical properties of the printed concrete can be weakened by the printing process.
- The research on materials and external finishing needs to be improved to reach enhanced performance in the printed object (e.g., the external steel rebar system is not protected by concrete and fire resistance is not yet assured).
- The printing process must be optimized in order to guarantee uniformity in thickness with varying setup parameters.
- The design step yet requires a great research effort, especially on the structural and topology optimization aspects since still limited by the printing material properties and technological limitations (more details on the argument are reported in the final conclusions of Chapter 5).

However, in our opinion, none of these issues justifies the ultimate rejection of this technology, at such an early phase of development, as a number of solutions can be imagined for each of them. In fact, to overcome possible local failure mechanisms that can limit the strength of the members, proper measures can be employed, such as high strength connection devices between bars and concrete elements, and buckling restraining systems. This is also the case of possible local deformations, which cause large deflections that can be overcome with adequate systems. In this case, post-tensioned cables can be an effective solution to limit the deflections. The ductility can be enhanced by inserting local energy absorption devices, e.g. dampers, into the concrete elements during the printing process. The external finishing can also be improved by refining the concrete mix and the printing parameters in order to enhance the properties of the extruded concrete, or by smoothing the surface of the elements just after the printing process, when the concrete has not yet hardened. Fire resistance can be improved with proper coatings of the bars or flexible boards can be used to encase the elements. Furthermore, the mechanical properties of the hardened concrete can be improved and controlled to satisfy the design requirements.

Opportunities

- This technique enables the fabrication of complex shapes, such as curved beams of variable heights. The use of post-tensioned cables can boost this capability, enabling the fabrication of very long elements with really complex shapes.
- The optimization of the shapes of the concrete segments enables a reduction in the volume of concrete used to fabricate RC members, while still guaranteeing good mechanical performances of the final elements. The reduction in the amount of concrete promises to make this manufacturing technology

sustainable from both the environmental and the economic point of view, if compared to the conventional casting process (see contents of Chapter 5).

- From a mechanical perspective, the reduction in the concrete volume implies a reduction in the mass of the elements, with possible indirect benefits to the structural systems, including the seismic behavior.
- The fabrication process does not need complex formwork systems and can be optimized to be faster, easier and cheaper than the conventional casting process.
- The concrete segments can be easily moved and transported to be assembled in situ into the final RC members; this approach enables a major reduction in the transport and installation costs, especially in the case of very long beams.

All of these opportunities still need to be confirmed and proved by further investigations and tests, but the initial results and outcomes are encouraging and form the basis for new research activities.

7 Conclusions

Multidisciplinary integration and innovation are the key words of today's integrated engineering and architectural design. Indeed, combining the conception of the project with the disciplines that regard its feasibility is the fundamental element for achieving optimal and challenging solutions for buildings and infrastructures. Furthermore, non-conventional and complex design has become more and more achievable thanks to research on new construction technologies and the development of sophisticated computational tools. Within this context, the present thesis wanted both to deepen the performance of numerical methods for the design of complex shapes and to present an innovative 3D printing method for the production of RC elements and possible compatible topology optimization tools.

Accordingly, in Chapters 2 and 3 an accurate non-prismatic beam model (NP-Model) has been presented and applied in real modeling problems. The advantages in adopting non-prismatic elements within structures are well known since they allow to optimize the structural behavior without renouncing to architectural freedom. However, common codified methods are often unable to account for the varying section shapes of non-prismatic elements, suffering of an ineffective modeling capability. To test the potential of the proposed NP-Model, results obtained with such model and the well-known structural software SAP2000 have been compared in a haunched beam-2D frame problem. The discussion of the results has highlighted a good response of the NP-Model but also significant differences with SAP2000, suggesting a cautious modeling of such structural elements when commercial codes are adopted. In fact, if the model provides a coarse description of the quantities of interest for the practitioners, the resulting design will be no longer effective and the performing features of non-prismatic elements would be compromised.

Moving towards new technologies which promote architectural freedom and construction methods improvements, a novel approach for the manufacturing of 3D printed RC members has been presented in Chapter 4. As described along the text, the basic idea is to separately print concrete segments then assembled to create complex shapes; each segment can be topologically optimized and a steel reinforcement system can be installed when the assembly is completed. Topology optimization of the concrete segments is a key ingredient within the design and production chain, thus, first steps towards a topology optimization strategy customized for such approach have been illustrated in Chapter 5. The two studied codes (the PSTOpt algorithm and the Kratos software) and obtained results have

outlined several problematic issues in the implementation of topology optimization for AM purposes. These aspects are related to the particular optimization problem, the stages of the design process, constraints and limitations connected to the printing material and the peculiarity of the 3D printing technology. All the difficulties listed above are the main challenges that have to be investigated in order to obtain performing optimization algorithms able to fill the gap between the design concept and the manufactured object. The ideal optimization tool for the proposed 3D printing approach should bring together the potential of the studied topology optimization methods (the PSTOpt algorithm and the Kratos software) in a unique and integrated platform.

Concerning the proposed 3d printing method, first applications of this technology have been proved in practice by two full-scale 3D printed beams and preliminary outcomes from an experimental activity and numerical analysis have been reported in Chapter 6. As emphasized in the final comments of the same Chapter, more investigations are needed to address some critical issues and extend this method to innovative practical cases. Among the issues, overall ductility, comparison with standard performances, size effects related to the printed technology, environmental degradation, steel rebar coating and fire resistance may represent further topic of interest for such a technology. Nevertheless, the application of AM in structural engineering clearly increase the building possibility, as the fabrication of complex elements (e.g. curved beams of variable heights), the topological optimization of shapes, the reduction of concrete volume and mass, the elimination of complex formwork systems, the easy transportability and installation.

This thesis wished at contributing to the research related to innovative engineering and architectural projects, moving over from modeling strategies of complex elements to the study of a new construction technology. As demonstrated by the increasing high sophistication of the commercial software available in the market, nowadays it is possible to solve (almost) any complex structural problem. In specific modeling problems, however, as for the case of non-prismatic elements treated in this thesis, professionals still need the help provided by the literature contributions to use in a conscious and effective manner commercial codes. On the other hand, the successful implementation of AM in the building industry appears challenging and several questions remain open. In fact, even if the innovative potential of AM can not be disputed, there is yet a lack of fundamental research on the matter which impedes its immediate insertion in this engineering field. Particularly, two major challenges have been identified:

- To clarify what large-scale additive manufacturing means. To fully understand how AM can be implemented in a construction work flow it is necessary to distinguish between "printing process" and "building system". Depending on the adopted additive manufacturing technique, indeed, it is possible to conceive different structural system or components. As example, the AM

approach proposed in this work is finalized to the design of RC elements as beams, pillars or single components. The final product is strictly connected to potential and limitations of the printing technology. A systematic classification of the available AM concrete-based technologies and related obtainable products is essential to develop real solutions in constructions.

- To facilitate study and understanding of concrete 3D printing to engineers and designers. To make possible an effective design a great effort in research have to be carried out, aimed at gaining more insights in all the aspects linked to 3D printing. The targeted research topics should concern 3D printing material, analytic/numerical method for the calculation of 3D printed concrete elements, and new proven experimental/statistical data to support theoretical advances.

In the author's opinion, the research model discussed in this thesis constitutes a valid guide in the development of new complex building elements. The present work aimed at joining the comprehension of the behavior of non-conventional objects with their effective realization trough the AM technology. Future research should unify the achievements obtained, combining the design step (using the non-prismatic beam model and a renewed topology optimization tool) with the presented 3D printing approach in a real application. Furthermore, the printed objects used as experimental samples should be designed to be integrated in a real building, then monitored over the time. The availability of such data would allow to identify practical issues of the printed components in each step of the building life (from the assembly to the behavior in exercise), supporting 3D printing as feasible construction technology.

Bibliography

E. Torroja and E. T. Miret. *Philosophy of structures*. Univ of California Press, 1958.

E. Montalar. 647 fotografas de estructuras, el iabse photo contest of structures 2011, 2012. http://enriquemontalar.com/647-fotografias-de-estructuras-el-iabse/.

M. Schoenholz. Salginatobel bridge, schiers switzerland, 2006. https://www.flickr.com/photos/mattschoenholz/173969167/.

S. Giedion. *Space, time and architecture: the growth of a new tradition*. Harvard University Press, 1967.

D. H. Hodges, A. Rajagopal, J. C. Ho, and W. Yu. Stress and strain recovery for the in-plane deformation of an isotropic tapered strip-beam. *Journal of Mechanics of Materials and Structures*, 5, 2010.

T. Zegard and G. H. Paulino. Bridging topology optimization and additive manufacturing. *Structural and Multidisciplinary Optimization*, 53(1):175–192, 2016.

ARUP. Design method for critical structural steel elements, 2014. https://www.arup.com/projects/additive-manufacturing.

S. Timoshenko. Strength of materials. In *Elementary theory and problems*. Krieger publishing company, 1955.

S. Bennati, P. Bertolini, L. Taglialegne, and P. S. Valvo. On shear stresses in tapered beams. In *GIMC-GMA 2016 - 21st Italian Conference on Computational Mechanics and 8th Meeting of the AIMETA Materials Group*, 2016.

G. Balduzzi, M. Aminbaghai, E. Sacco, J. Füssl, J. Eberhardsteiner, and F. Auricchio. Non-prismatic beams: a simple and effective Timoshenko-like model. *International Journal of Solids and Structures*, 90:236–250, 2016a.

M. Zhou, J. Zhang, J. Zhong, and Y. Zhao. Shear stress calculation and distribution in variable cross sections of box girders with corrugated steel webs. *Journal of Structural Engineering*, 142(6):04016022, 2016.

A. Paglietti and G. Carta. La favola del taglio efficace nella teoria delle travi di altezza variabile. In *AIMETA*, 2007.

A. Beltempo, C. Cappello, D. Zonta, A. Bonelli, O. S. Bursi, C. Costa, and W. Pardatscher. Structural health monitoring of the Colle Isarco viaduct. In *Environmental and Energy and Structural Monitoring Systems (EESMS) and 2015 IEEE Workshop on*, pages 7–11. IEEE, 2015a.

F. Auricchio, G. Balduzzi, and C. Lovadina. A new modeling approach for planar beams: finite-element solutions based on mixed variational derivations. *Journal of Mechanics of Materials and Structures*, 5(5):771–794, 2010.

G. Balduzzi. *Beam Models: Varyational derivation and Analytical and Numerical Solutions*. PhD thesis, Universitá degli Studi di Pavia, 2013.

A. Beltempo, G. Balduzzi, G. Alfano, and F. Auricchio. Analytical derivation of a general 2d non-prismatic beam model based on the hellinger–reissner principle. *Engineering Structures*, 101:88–98, 2015b.

S. Timoshenko and J. N. Goodier. *Theory of Elasticity*. McGraw-Hill, 3rd edition, 1970.

S. Timoshenko and D. H. Young. *Theory of Structures*. McGraw-Hill, 1965.

Portland and Cement Associations. *Handbook of frame constants. Beam factor and moment coefficient for members of variable section*. Portland and Cement Associations, 1958.

F. Romano and G. Zingone. Deflections of beams with varying rectangular cross section. *Journal of engineering mechanics*, 118(10):2128–2134, 1992.

F. Romano. Deflections of timoshenko beam with varying cross-section. *International journal of mechanical sciences*, 38(8):1017–1035, 1996.

S.J. Medwadowski. Nonprismatic shear beams. *Journal of Structural Engineering*, 110:1067–1082, 1984.

K. J. Schneider and A. Albert. *Bautabellen für Ingenieure: mit Berechnungshinweisen und Beispielen*. Bundesanzeiger Verlag GmbH, 2014. ISBN 9783846203040. https://books.google.at/books?id=X0eSoAEACAAJ.

N. El-Mezaini, C. Balkaya, and E. Citipitioglu. Analysis of frames with nonprismatic members. *Journal of Structural Engineering*, 117:1573–1592, 1991.

C. Balkaya, E. Citipitioglu, and A. Tena-Colunga. Stiffness formulation for nonprismatic beam elements. *Journal of Structural Engineering*, 1996.

H. J. Al-Ghatani and M. S. Khan. Exact analysis of nonprismatic beams. *Journal of Engineering Mechanics*, 124:1290–1293, 1998.

G. Balduzzi, G. Hochreiner, J. Füssl, and F. Auricchio. Performance evaluation of new straightforward formulas for the serviceability analysis of cambered timber beams. In *Proceedings of the Word Conference on Timber Engineering*, 2016b.

O. T. Bruhns. *Advanced Mechanics of Solids*. Springer, 2003.

O. W. Blodgett. *Design of welded structures*, chapter 4.4, pages 1–8. the James F. Lincon arc welding foundation, 1966.

L. Vu-Quoc and P. Léger. Efficient evaluation of the flexibility of tapered i-beams accounting for shear deformations. *International journal for numerical methods in engineering*, 33(3):553–566, 1992.

B. A. Boley. On the accuracy of the bernoulli-euler theory for beams of variable section. *Journal of applied mechanics*, 30(3):373–378, 1963.

D. H. Hodges, C. H. Jimmy, and W. Yu. The effect of taper on section constants for in-plane deformation of an isotropic strip. *Journal of Mechanics of Materials and Structures*, 3, 2008.

H. Rubin. Analytische Berechnung von Stäben mit linear veränderlicher Höhe unter Berücksichtigung von M- and Q- und N- Verformungen. *Stahlbau*, 68:112–119, 1999.

F. Auricchio, G. Balduzzi, and C. Lovadina. The dimensional reduction approach for 2D non-prismatic beam modelling: a solution based on Hellinger-Reissner principle. *International Journal of Solids and Structures*, 15:264–276, 2015.

E. Kosko. Uniform element modeling of tapered frame members. *Journal of the Structural Division*, 108(1):245–264, 1982.

R. Raymond and F. K. Wang. Stiffnesses of nonprismatic member. *Journal of Structural Engineering*, 114(2):489–494, 1988.

C. M. Patel and G. D. Acharya. Analytical determination of deflection of stepped cantilever rectangular beam under uniform load, 2016.

D. J. Just. Plane frameworks of tapering box and i-section. *Journal of the Structural Division*, 103(1):71–86, 1977.

C. J. Browns. Approximate stiffness matrix for tapered beams. *Journal of Structural Engineering*, 110:3050–3055, 1984.

M. Eisenberger. Explicit stiffness matrix for nonprismatic members. *Computer & Structures*, 20:715–720, 1985.

A. Tena-Colunga. Stiffness formulation for nonprismatic beam elements. *Journal of Structural Engineering*, 122:1484–1489, 1996.

Y. Zhi-Luo, X. Xu, and F. Wu. Accurate stiffness matrix for nonprismatic members. *Journal of Structural Engineering*, 133:1168–1175, 2007.

F. Gimena, P. Gonzaga, and L. Gimena. 3d-curved beam element with varying cross-sectional area under generalized loads. *Engineering structures*, 30(2):404–411, 2008a.

F. Gimena, P. Gonzaga, and L. Gimena. Structural analysis of a curved beam element defined in global coordinates. *Engineering Structures*, 30(11):3355–3364, 2008b.

A. Shooshtari and R. Khajavi. An efficient procedure to find shape functions and stiffness matrices of nonprismatic euler-bernoulli and timoshenko beam elements. *European Journal of Mechanics A/Solids*, 29:826–836, 2010.

C. Balkaya. Behavior and modeling of nonprismatic members having t-sections. *Journal of Structural Engineering*, 127:940–946, 2001.

G. Failla and N. Impollonia. General finite element description for non-uniform and discontinuos beam element. *Archive of Applied Mechanics*, 82:43–67, 2012.

T. H. Trinh and B. S. Gan. Development of consistent shape functions for linearly solid tapered Timoshenko beam. *Journal of Structural and Construction Engineering*, 80:1103–1111, 2015.

SIMULIA Dassault Sistèmes. *Abaqus Analysis User's Manual*, 2012.

Wolfram Mathematica. 7 documentation center. *Available from:http://reference.wolfram.com/language/*, 2017.

Computer & Structures Inc. *CSI Analysis Reference Manual*, 2011.

Y. H. Zeinali, S. M. Jamali, and S. Musician. General form of the stiffness matrix of a tapered-beam column. *International Journal of Mining and Metallurgy & Mechanical Engineering*, 1:2320–4060, 2013.

A. Tena-Colunga and L. A. M. Becerril. Lateral stiffness of reinforced concrete moment frames with haunched beams. In *15TH WORLD CONFERENCE ON EARTHQUAKE ENGINEERING*, 2012.

NTC. *Norme tecniche per le costruzioni*, D.M. January 14 and 2008.

Eurocode 2. *Design of concrete structures. Part 1-1: General rules and rules for buildings*, 2004.

Eurocode 8. *Design of structures for earthquake resistance. Part 1: General rules and seismic actions and rules for buildings*, 2004.

Standard ASTM. F2792 standard terminology for additive manufacturing technologies. *ASTM F2792-10e1*, 2012.

B. Berman. 3-d printing: The new industrial revolution. *Business horizons*, 55(2): 155–162, 2012.

H. Lipson and M. Kurman. *Fabricated: The new world of 3D printing.* John Wiley & Sons, 2013.

F. Rengier, A. Mehndiratta, H. von Tengg-Kobligk, C. M. Zechmann, R. Unterhinninghofen, H-U. Kauczor, and F. L. Giesel. 3d printing based on imaging data: review of medical applications. *International journal of computer assisted radiology and surgery*, 5(4):335–341, 2010.

T. Campbell, C. Williams, O. Ivanova, and B. Garrett. Could 3d printing change the world. *Technologies, Potential, and Implications of Additive Manufacturing, Atlantic Council, Washington, DC*, 2011.

I. J. Petrick and T. W. Simpson. 3d printing disrupts manufacturing: how economies of one create new rules of competition. *Research-Technology Management*, 56(6):12–16, 2013.

J. P. Kruth, G. Levy, F. Klocke, and T. C. H. Childs. Consolidation phenomena in laser and powder-bed based layered manufacturing. *CIRP Annals-Manufacturing Technology*, 56(2):730–759, 2007.

I. Agustí-Juan, F. Müller, N. Hack, T. Wangler, and G. Habert. Potential benefits of digital fabrication for complex structures: Environmental assessment of a robotically fabricated concrete wall. *Journal of Cleaner Production*, 154:330–340, 2017.

U. Scheithauer, E. Schwarzer, H. Richter, and T. Moritz. Thermoplastic 3d printing-an additive manufacturing method for producing dense ceramics. *International journal of applied ceramic technology*, 12(1):26–31, 2015.

C. Ladd, J. So, J. Muth, and M. D. Dickey. 3d printing of free standing liquid metal microstructures. *Advanced Materials*, 25(36):5081–5085, 2013.

J. A. Inzana, D. Olvera, S. M. Fuller, J. P. Kelly, O. A. Graeve, E. M. Schwarz, S. L. Kates, and H. A. Awad. 3d printing of composite calcium phosphate and collagen scaffolds for bone regeneration. *Biomaterials*, 35(13):4026–4034, 2014.

J. Pegna. Exploratory investigation of solid freeform construction. *Automation in construction*, 5(5):427–437, 1997.

J. Pegna, S. Pattofatto, R. Berge, C. Bangalan, H. Herring, M. LeSaux, and J. Engler. The sand painter: two dimensional powder deposition. In *Proceedings on the Solid Freeform Fabrication Symposium, Austin, TX*, pages 695–709, 1999.

R. A. Buswell, R. C. Soar, A. G. F. Gibb, and A. Thorpe. Freeform construction: mega-scale rapid manufacturing for construction. *Automation in construction*, 16(2):224–231, 2007.

T. Wangler, E. Lloret, L. Reiter, N. Hack, F. Gramazio, M. Kohler, M. Bernhard, B. Dillenburger, J. Buchli, N. Roussel, et al. Digital concrete: opportunities and challenges. *RILEM Technical Letters*, 1:67–75, 2016.

B. Khoshnevis. Automated construction by contour crafting?related robotics and information technologies. *Automation in construction*, 13(1):5–19, 2004.

S. Lim, R. A. Buswell, T. T. Le, S. A. Austin, A. G. F. Gibb, and T. Thorpe. Developments in construction-scale additive manufacturing processes. *Automation in construction*, 21:262–268, 2012.

A. Tibaut, D. Rebolj, and M. N. Perc. Interoperability requirements for automated manufacturing systems in construction. *Journal of intelligent manufacturing*, 27 (1):251–262, 2016.

E. Lloret, A. R. Shahab, M. Linus, R. J. Flatt, F. Gramazio, M. Kohler, and S. Langenberg. Complex concrete structures: Merging existing casting techniques with digital fabrication. *Computer-Aided Design*, 60:40–49, 2015.

I. Perkins and M. Skitmore. Three-dimensional printing in the construction industry: A review. *International Journal of Construction Management*, 15(1):1–9, 2015.

T. T. Le, S. A. Austin, S. Lim, R. A. Buswell, A. G. F. Gibb, and T. Thorpe. Mix design and fresh properties for high-performance printing concrete. *Materials and structures*, 45(8):1221–1232, 2012.

H. Valkenaers, D. Jansen, A. Voet, A. Van Gysel, and E. Ferraris. Additive manufacturing for concrete: a 3d printing principle. In *Proceedings of the 14th euspen International Conference*, volume 1, pages 139–142. euspen, 2014.

A. Perrot, D. Rangeard, and A. Pierre. Structural built-up of cement-based materials used for 3d-printing extrusion techniques. *Materials and Structures*, 49(4): 1213–1220, 2016.

STRESS. Consortium for the development of research and technologies for sustainable and seismically safe building, 2015. http://www.stress-scarl.com/it/.

A. Rudenko. 3d concrete house printer, 2017. http://www.totalkustom.com/.

P. P. Xanthakos. *Theory and design of bridges*. John Wiley & Sons, 1994.

WASP. Wasp world's advanced saving project, 2015. http://www.wasproject.it/w/.

EN-12350. *Testing fresh concrete - Part 2: Slump test.*, 2009.

EN-12390. *Testing hardened concrete - Part 3: Compressive strength of test specimens.*, 2009.

J. Schlaich, K. Schäfer, and M. Jennewein. Toward a consistent design of structural concrete. *PCI journal*, 32(3):74–150, 1987.

M. Schlaich and G. Anagnostou. Stress fields for nodes of strut-and-tie models. *Journal of Structural Engineering*, 116(1):13–23, 1990.

CIMNE. *KRATOS Multiphysics software*, 2017.

G. Rozvany. *Topology optimization in structural mechanics*, volume 374. Springer, 2014.

G. Chahine, P. Smith, and R. Kovacevic. Application of topology optimization in modern additive manufacturing. In *Solid Freeform Fabrication Symposium*, pages 606–618, 2010.

A. T. Gaynor. *Topology optimization algorithms for additive manufacturing.* PhD thesis, 2015.

A. Aremu, I. Ashcroft, R. Hague, R. Wildman, and C. Tuck. Suitability of simp and beso topology optimization algorithms for additive manufacture. In *21st Annual International Solid Freeform Fabrication Symposium (SFF)–An Additive Manufacturing Conference*, pages 679–692, 2010.

V. G. Sundararajan. *Topology optimization for additive manufacturing of customized meso-structures using homogenization and parametric smoothing functions.* PhD thesis, 2010.

C. Chu, G. Graf, and D. W. Rosen. Design for additive manufacturing of cellular structures. *Computer-Aided Design and Applications*, 5(5):686–696, 2008.

N. Meisel A. Gaynor, C. Williams, and J. Guest. Multiple-material topology optimization of compliant mechanisms created via polyjet 3d printing. In *24th Annual international solid freeform fabrication symposium an additive manufacturing conference*, page 28, 2013a.

Z. Doubrovski, J. C. Verlinden, and J. M. Geraedts. Optimal design for additive manufacturing: opportunities and challenges. In *ASME 2011 International Design Engineering Technical Conferences and Computers and Information in Engineering Conference*, pages 635–646. American Society of Mechanical Engineers, 2011.

D. Brackett, I. Ashcrof, and R. Hague. Topology optimization for additive manufacturing. In *Proceedings of the solid freeform fabrication symposium, Austin, TX*, volume 1, pages 348–362. S, 2011.

C. Gosselin, R. Duballet, P. Roux, N. Gaudillière, J. Dirrenberger, and P. Morel. Large-scale 3d printing of ultra-high performance concrete–a new processing route for architects and builders. *Materials & Design*, 100:102–109, 2016.

Q. Q. Liang, Y. M. Xie, and G. P. Steven. *Topology optimization of strut-and-tie models in reinforced concrete structures using an evolutionary procedure*. PhD thesis, American Concrete Institute, 2000.

M. Bruggi. Generating strut-and-tie patterns for reinforced concrete structures using topology optimization. *Computers & Structures*, 87(23):1483–1495, 2009.

Q. Q. Liang, Y. M. Xie, and G. P. Steven. Generating optimal strut-and-tie models in prestressed concrete beams by performance-based optimization. *ACI Structural Journal*, 98(2):226–232, 2001.

M. Bogomolny and O. Amir. Conceptual design of reinforced concrete structures using topology optimization with elastoplastic material modeling. *International journal for numerical methods in engineering*, 90(13):1578–1597, 2012.

O. Amir. A topology optimization procedure for reinforced concrete structures. *Computers & Structures*, 114:46–58, 2013.

O. Amir and O. Sigmund. Reinforcement layout design for concrete structures based on continuum damage and truss topology optimization. *Structural and Multidisciplinary Optimization*, 47(2):157–174, 2013.

G. Sved and Z. Ginos. Structural optimization under multiple loading. *International Journal of Mechanical Sciences*, 10(10):803–805, 1968.

A. T. Gaynor, J. K. Guest, and C. D. Moen. Reinforced Concrete Force Visualization and Design Using Bilinear Truss-Continuum Topology Optimization. *Journal of Structural Engineering*, 139(April):607–618, 2013b. ISSN 0733-9445. doi: 10.1061/(ASCE)ST.1943-541X.0000692.

J. París, F. Navarrina, I. Colominas, and M. Casteleiro. Topology optimization of continuum structures with local and global stress constraints. *Structural and Multidisciplinary Optimization*, 39(4):419–437, 2009.

C. Le, J. Norato, T. Bruns, C. Ha, and D. Tortorelli. Stress-based topology optimization for continua. *Structural and Multidisciplinary Optimization*, 41(4): 605–620, 2010.

N. M. Patel, D. Tillotson, J. E. Renaud, A. Tovar, and K. Izui. Comparative study of topology optimization techniques. *AIAA journal*, 46(8):1963, 2008.

E. Biyikli and A. C. To. Proportional topology optimization: A new non-sensitivity method for solving stress constrained and minimum compliance problems and its implementation in matlab. *PloS one*, 10(12):e0145041, 2015.

M. P. Bendsøe. Optimal shape design as a material distribution problem. *Structural and multidisciplinary optimization*, 1(4):193–202, 1989.

M. Zhou and G. Rozvany. The coc algorithm, part ii: topological, geometrical and generalized shape optimization. *Computer Methods in Applied Mechanics and Engineering*, 89(1-3):309–336, 1991.

E. Andreassen, A. Clausen, M. Schevenels, B. S. Lazarov, and O. Sigmund. Efficient topology optimization in matlab using 88 lines of code. *Structural and Multidisciplinary Optimization*, 43(1):1–16, 2011.

M. P. Bendsøe and O. Sigmund. *Topology optimization by distribution of isotropic material*. Springer, 2004.

O. Sigmund and J. Petersson. Numerical instabilities in topology optimization: a survey on procedures dealing with checkerboards, mesh-dependencies and local minima. *Structural and Multidisciplinary Optimization*, 16(1):68–75, 1998a.

M. Zhou, Y. K. Shyy, and H. L. Thomas. Checkerboard and minimum member size control in topology optimization. *Structural and Multidisciplinary Optimization*, 21(2):152–158, 2001.

O. Sigmund. Morphology-based black and white filters for topology optimization. *Structural and Multidisciplinary Optimization*, 33(4):401–424, 2007a.

T. E. Bruns and D. A. Tortorelli. Topology optimization of non-linear elastic structures and compliant mechanisms. *Computer Methods in Applied Mechanics and Engineering*, 190(26):3443–3459, 2001.

O. Sigmund and J. Petersson. Numerical instabilities in topology optimization: a survey on procedures dealing with checkerboards, mesh-dependencies and local minima. *Structural optimization*, 16(1):68–75, 1998b.

G. H. Golub and J. H. Welsch. Calculation of gauss quadrature rules. *Mathematics of computation*, 23(106):221–230, 1969.

G. Rozvany. Exact analytical solutions for some popular benchmark problems in topology optimization. *Structural and Multidisciplinary Optimization*, 15(1): 42–48, 1998.

A. G. M. Michell. Lviii. the limits of economy of material in frame-structures. *The London, Edinburgh, and Dublin Philosophical Magazine and Journal of Science*, 8(47):589–597, 1904.

S. R. Picelli, S. Townsend, C. Brampton, J. Norato, and H. Kim. Stress-based shape and topology optimization with the level set method. *Computer Methods in Applied Mechanics and Engineering*, 2017.

P. M. Mariano and L. Galano. *Fundamentals of the Mechanics of Solids*. Springer, 2015.

C. Talischi, G. H. Paulino, A. Pereira, and I. F. M. Menezes. Polytop: a matlab implementation of a general topology optimization framework using unstructured polygonal finite element meshes. *Structural and Multidisciplinary Optimization*, 45(3):329–357, 2012.

K. Liu and A. Tovar. An efficient 3d topology optimization code written in matlab. *Structural and Multidisciplinary Optimization*, 50(6):1175–1196, 2014a.

N. Aage, E. Andreassen, and B. S. Lazarov. Topology optimization using petsc: An easy-to-use, fully parallel, open source topology optimization framework. *Structural and Multidisciplinary Optimization*, 51(3):565–572, 2015.

E. R. G. Baske. *Development of an open-source tool for 3D Topology Optimization and its extension towards integrated design and analysis*. PhD thesis, Technische Universitt Mnchen (TUM), 2015.

O. Malfavon Farias. *Development of an open-source tool for 3D Topology Optimization and its extension towards integrated design and analysis*. PhD thesis, Technische Universitt Mnchen (TUM), 2016.

O. Sigmund. A 99 line topology optimization code written in matlab. *Structural and multidisciplinary optimization*, 21(2):120–127, 2001.

K. Liu and A. Tovar. An efficient 3D topology optimization code written in Matlab. *Structural and Multidisciplinary Optimization*, 50(6):1175–1196, 2014b. ISSN 16151488. doi: 10.1007/s00158-014-1107-x.

M. P. Bendsøe and O. Sigmund. *Topology optimization: theory, methods, and applications*. Springer Science & Business Media, 2013.

O. Sigmund. Morphology-based black and white filters for topology optimization. *Structural and Multidisciplinary Optimization*, 33(4-5):401–424, 2007b. ISSN 1615147X. doi: 10.1007/s00158-006-0087-x.

K. Bletzinger, M. Firl, and F. Daoud. Approximation of derivatives in semi-analytical structural optimization. *Computers & structures*, 86(13):1404–1416, 2008.

E. Stavropoulou. *Sensitivity analysis and regularization for shape optimization of coupled problems*. PhD thesis, München, Technische Universität München., 2015.

M. P. Bendsøe. *Optimization of structural topology, shape, and material*, volume 414. Springer, 1995.

R. Ribó and M. Riera. Gid, the personal pre and post processor. *Reference Manual, version*, 9, 2008.

H. Lakshmininarayana. *Finite Elements Analysis: Procedures in Engineering*. Universities Press, 2004.

D. Baumgartnerand J. Wolf, R. Rossi, R. Wüchner, and P. Dadvand. *Contribution to the fluid-structure interaction analysis of ultra-lightweight structures using an embedded approach*. CIMNE, 2015.

L. E. Roscoe et al. *Stereolithography interface specification*, 1988.

J. Vollmer, R. Mencl, and H. Mueller. Improved laplacian smoothing of noisy surface meshes. In *Computer graphics forum*, volume 18, pages 131–138. Wiley Online Library, 1999.

J. B. Mander, M. J. N. Priestley, and R. Park. Theoretical stress-strain model for confined concrete. *Journal of structural engineering*, 114(8):1804–1826, 1988.

EN1992-1-1. *Eurocode 2: Design of concrete structures - Part 1-1: General rules and rules for buildings.*, 2004.

Computer & Structures Inc. *CSI Analysis Reference Manual.*, 2009.